MEASUREMENT OF THE $Z\gamma\gamma$ PRODUCTION CROSS SECTION AT PROTON-PROTON COLLISIONS WITH THE CMS EXPERIMENT

by

SACHIKO TODA MCBRIDE

B.S., Syracuse University, 2009

AN ABSTRACT OF A DISSERTATION

submitted in partial fulfillment of the
requirements for the degree

DOCTOR OF PHILOSOPHY

Department of Physics
College of Arts and Sciences

KANSAS STATE UNIVERSITY
Manhattan, Kansas

2016

Abstract

This thesis presents the first study of a rare production of Z boson in association with two photons ($Z\gamma\gamma$), where the Z boson decays into a pair of muons or electrons, by proton-proton collisions at the Large Hadron Collider (LHC). This study uses full data samples that have been collected with the Compact Muon Solenoid (CMS) detector in 2012 with a center of mass energy of 8 TeV, corresponding to an integrated luminosity of $19.7\,\mathrm{fb}^{-1}$. The $Z\gamma\gamma$ production cross section is measured within a fiducial region defined by two leptons with two photons where transverse momentum over 15 GeV and distance between γ and ℓ above 0.4. Using the obtained samples, the $Z\gamma\gamma$ cross section is measured to be:

$$12.6 \pm 1.6\ (\mathrm{stat.}) \pm 1.7\ (\mathrm{syst.}) \pm 0.3\ (\mathrm{lumi.})\,\mathrm{fb}.$$

where stat., syst., and lumi. denote the statistical uncertainty, systematic uncertainty, and the uncertainty in integrated luminosity, respectively. This result is in an excellent agreement with the theoretical prediction of $13.0 \pm 1.5\,\mathrm{fb}$.

MEASUREMENT OF THE $Z\gamma\gamma$ PRODUCTION CROSS SECTION AT PROTON-PROTON COLLISIONS WITH THE CMS EXPERIMENT

by

SACHIKO TODA MCBRIDE

B.S., Syracuse University, 2009

A DISSERTATION

submitted in partial fulfillment of the
requirements for the degree

DOCTOR OF PHILOSOPHY

Department of Physics
College of Arts and Sciences

KANSAS STATE UNIVERSITY
Manhattan, Kansas

2016

Approved by:

Major Professor
Dr. Yurii Y. Maravin

Copyright

Abstract

This thesis presents the first study of a rare production of Z boson in association with two photons ($Z\gamma\gamma$), where the Z boson decays into a pair of muons or electrons, by proton-proton collisions at the Large Hadron Collider (LHC). This study uses full data samples that have been collected with the Compact Muon Solenoid (CMS) detector in 2012 with a center of mass energy of 8 TeV, corresponding to an integrated luminosity of $19.7\,\mathrm{fb}^{-1}$. The $Z\gamma\gamma$ production cross section is measured within a fiducial region defined by two leptons with two photons where transverse momentum over 15 GeV and distance between γ and ℓ above 0.4. Using the obtained samples, the $Z\gamma\gamma$ cross section is measured to be:

$$12.6 \pm 1.6\ (\mathrm{stat.}) \pm 1.7\ (\mathrm{syst.}) \pm 0.3\ (\mathrm{lumi.})\,\mathrm{fb}.$$

where stat., syst., and lumi. denote the statistical uncertainty, systematic uncertainty, and the uncertainty in integrated luminosity, respectively. This result is in an excellent agreement with the theoretical prediction of $13.0 \pm 1.5\,\mathrm{fb}$.

Table of Contents

List of Figures

List of Tables

Acknowledgments

There are many people that I have interacted with over the course of completing my doctoral studies, which have spanned 2 states and 3 countries.

First and foremost, I would like to express my sincere thanks to my PhD adviser, Dr. Yurii Maravin, for his continuous guidance expertise; mentoring me from my first semester programming exercise at Kansas State University to giving me skills sets that I am sure will help me in my future career. Without his encouragement and support, this dissertation would not have been possible.

I am grateful to the all faculty members of High Energy Physics: Dr. Glenn Horton-Smith, Dr. Tim Bolton, Dr. Larry Weaver, Dr. Andrew Ivanov, and Dr. Ketino Kaadze for their helpful advice, support, and for reading sections of this dissertation. I am also thankful to my current and previous colleagues in the HEP group along with Dr. Lovedeep Saini, Dr. Mihail Makouski, Dr. Sadia Khalil, Dr. Irakli Chakaberia, Dr. Nikoloz Sklirladze, Dr. Shruti Shrestha, Dr. Pi-Jung Chang, Dr. Deepak Shrestha, Dr. Irakli Svintradze, and Saima Farooq.

I owe special thanks to Dr. Josh Kunkle and Christopher Anelli at University of Maryland and Dr. Chia-Ming Kuo at National Central University in Taiwan, who worked on the $Z\gamma\gamma$ analysis with me, for all helpful advice, suggestions, support, and comments. I have learned so much from the three of these individuals. I also wish to thank Dr. Daniele Benedetti and Dr. Lindsey Gray at CERN and Fermilab respectively, for their appropriate advice and support of my previous work on implemented CMS software of electron pre-identification.

I am thankful to Dr. Julia Gray from University of Kansas, Dr. Morris Swartzs at Johns Hopkins University, and Dr. Alessia Tricomi at University and INFN for their useful ideas and information to correctly integrate the radiation re-weighting code and templates into

simulation samples which was another subset of my previous work. A special thanks also goes to all my colleagues in the CMS WebBased Monitoring team at Fermilab and CERN along with Dr. Kaori Maeshima, Dr. Juan Antonio Lopez-Perez, Dr. William Badgett, Dr. Sho Maruyama, Dr. James Patrick, and Dr. Aron Soha for great working experience. I am greateful for amount of WebBased Monitoring skills I obtained through the expert guidance from these individuals.

I am also in debt to the staff of the Physics Department, specially Peggy Matthews, Jane Peterson, Pamela Anderson, Kim Coy, and Kimberly Elliott for everything you have done for me over the past 5 years. Your efforts in maintaining my academic assistantship, your efforts in supporting all my travels between CERN, Fermilab, and Kansas, and for your efforts in keeping all financial affairs associated during my doctoral studies have all been greatly appreciated. I am also thankful to Dr. Bruce Law for assisting me in my moving transitions between CERN, Fermilab, and Kansas.

I would also like to thank all of my wonderful friends in Physics Department along with Dr. Sean P. McBride, Dr. Amy Rouinfar, Dr. Mohammad Zohrabi, Bethany Jochim, Dr. Shuo Zeng, Dr. Varun "Mac" Makhija, Dr. Bachana Lomsadze, Wes Erbsen, Dr. Omer Farooq, Neda Dadashzadeh, Jeff Powell, Utuq Ablikim, Sara Crandall, and Dr. Maia Magrakvelidze for sharing many great times and memories in Manhattan, KS! Without Sean, Amy, Mohammad, Bethany, Shuo, Mac, and Neda my life in Kansas would not have been as memorable and enjoyable. We always had a great time together every time when I came back to Kansas, and I always missed them every time I stayed outside of Kansas.

A special thanks goes to Jane and Rodney Fox and David Stuckenschmidt, who are great friends in Kansas that assisted me in so many when I first arrived in Manhattan Kansas.

I am thankful to my great Japanese friends at CERN and Fermilab: Dr. Yasuyuki Okumura, Dr. Yuta Takahashi, Dr. Yutaro Iiyama, Dr. Hidetoshi Otono, and Dr. Hideyuki Oide for still making time to have fun together outside of research. Yasuyuki and Yuta always had great advice and useful comments whenever I asked various questions. I have

learned so much from the both of them. I really appreciate it!

I am thankful to Dr. Joseph Schechter and Dr. Sheldon Stone at Syracuse University. They introduced me to the High Energy Physics field and encourage me come to Kansas State University. I am thankful for all the help I received from the support staff at Fermilab, especially Carrie S Farver, administrative support, and Jacqueline "Jackie" J. Cyko, an accommodation organizer at Fermilab for assisting in organizing my living accommodations at Fermilab during each move.

Finally, I owe my deepest gratitude to my father, Nobuhiro, my sister, Yumiko, and my brother, Hiroshi for their support, encouragement, and love throughout all my academic study in the United States. I am deeply in debt and thankful to my father who encouraged me to study abroad for my undergraduate and graduate studies. Without his support, none of this would have been possible.

Also, I am very thankful to my US parents in Pennsylvania, Duy and Sheila McBride. From day one, they always warmly welcome me as a member of the family. Most importantly, I would like to express a special thankful to my husband, Sean P. McBride, for his love, support, understanding, and encouragement. I am very glad to have met you here at Kansas. It has not been easy with all the moving back and forth between CERN, Fermilab, and Kansas but your patience and understanding is beyond measureable. I could not have done my dissertation without you. I am excited for our future and our life together!

Dedication

I would like to dedicate this thesis to my father, Nobuhiro Toda, my brother, Hiroshi Toda, and my sister, Yumiko Sawada.

Chapter 1

Introduction

> "What?" or "Why?" growing in your mind is exactly the "Bud of Science." Observe, examine, and then look into your wonder. This is exactly the stem of science. Then you find the answer of your wonder. This is the flower of science.
> - Dr. Sin-itiro Tomonaga [17]

This thesis presents the first observation of a rare production of Z boson in association with two photons. The study of this process provides a strong test of the electroweak sector of the Standard Model (SM) at the TeV energy scale within the Compact Muon Solenoid (CMS) experiment. The measurement was performed using CMS data taken during the full 2012 run at a center of mass energy [1] of $\sqrt{s} = 8\,\text{TeV}$, corresponding to an integrated luminosity [2] of $19.7\,\text{fb}^{-1}$. This thesis is organized as the following: the introduction of theoretical background related to $Z\gamma\gamma$ production at proton-proton collisions is presented in Chapter 2. A brief description of the experimental apparatus of the Large Hadron Collider (LHC) [3] accelerator and an overview of the CMS detector including all sub-detector systems

[1] The center of mass energy is defined as the center of mass system at proton-proton collisions. The four momentum of circulating protons at $\sqrt{s} = 8\,\text{TeV}$ are p1 = (4.0 TeV, 0, 0, 4.0 TeV) and p2 = (4.0 TeV, 0, 0, -4.0 TeV), thus the four momentum of the center of mass system is p1 + p2 = (8 TeV, 0, 0, 0) at LHC [18].

[2] The luminosity is the quantity of rate of production in a collider.

[3] The LHC is the largest and the highest energy collider in the world.

are given in Chapter 3. The reconstruction of final state particles: electrons, muons, and photons, that for the Z$\gamma\gamma$ production in Chapter 4. The data analysis to measure the Z$\gamma\gamma$ production cross section is given in Chapter 5, and the conclusion is given in Chapter 6. A brief summary of data analysis, described in Chapter 5, is given below:

- Section 5.1: The data and Monte Carlo (MC) simulation samples of signal and background events used in the Z$\gamma\gamma$ study are summarized in this section.

- Section 5.2: The selection criteria used to identify electrons, muons, and photons in this analysis is described in this section. These definitions are optimized by CMS Egamma Physics Object Group (POGs) and Muon-POGs, and additional offline requirements are applied to select the Z$\gamma\gamma$ event candidates.

- Section 5.3: The applications of pile-up reweighting and additional scale factors of objects identification and dilepton trigger are described. They are applied to all MC simulation samples to improve the agreement between the data and MC samples. All works using MC simulations are done with the applications of pile-up reweighting method and additional scale factors.

- Section 5.4: This section discusses how we estimate background events to the Z$\gamma\gamma$ process. The Zγ + jets and Z + jets productions, where one or two of jets are misidentified as photon candidates, are the dominant background. The background contributions are established using control data sample.

- Section 5.5: The Z$\gamma\gamma$ production cross section is measured in a fiducial region that is defined to be close to the offline event selection in order to minimize extrapolations from the selected events. The components used for the measurement of the cross section include the expected signal events, the acceptance of Z$\gamma\gamma$ process, and the integrated luminosity. This section summarizes the definition of fiducial region and calculate the acceptance for Z$\gamma\gamma$ process.

- Section 5.6: The various sources of the systematic uncertainty considered in the cross section measurements are described in this section. These sources are taken into account in the analysis:
  - uncertainty in the luminosity evaluation
  - uncertainty in the detector performance
  - uncertainty related to the simulation sample
  - uncertainty from the background estimation
- Section 5.7: The fiducial cross sections in two channels for $Z\gamma\gamma \to \mu\mu\gamma\gamma$ and $Z\gamma\gamma \to ee\gamma\gamma$ process are measured individually and combined to the final cross section of $Z\gamma\gamma$ process.

We measure the $Z\gamma\gamma$ production cross section to be:

$$12.6 \pm 1.6\ (\text{stat.}) \pm 1.7\ (\text{syst.}) \pm 0.3\ (\text{lumi.})\,\text{fb}.$$

where stat., syst., and lumi. denote the statistical uncertainty, systematic uncertainty, and the uncertainty in integrated luminosity, respectively. This result is in great agreement with the theoretical prediction of $13.0 \pm 1.5\,\text{fb}$.

Chapter 2

Theoretical Background

2.1 The Standard Model

The standard model (SM) of elementary particle physics is expressed by a quantum field theory that describes the fundamental particles and their interactions [19]. All particles in the SM framework are divided into two types: bosons and fermions. The fermions have spin quantum number equal to $\frac{1}{2}$ and hence obey the Fermi statistics and constitute matter. The bosons have spin quantum number equal to 1 or 0 and follow the Bose statistics. The gauge bosons are gluons, photons, Z, and $W^{\pm}$ and are the fundamental force mediators. The SM describes the fundamental forces by their gauge group: strong - $SU(3)_C$ and electroweak - $SU(2)_L \otimes U(1)_Y$. Therefore, the SM theory is based on the gauge symmetry of $SU(3)_C \otimes SU(2)_L \otimes U(1)_Y$ [1] [19]. Figure 2.1 shows these fundamental forces and their mediators. The gravitational force is not included in the SM, and the hypothetical particle called the graviton has not been observed.

The fundamental fermions are classified into six leptons and six quarks that are divided into three generations. The six leptons are classified into charged leptons (electron (e), muon (μ), and tau (τ)) and neutral leptons called neutrinos (electron neutrino (ν_e), muon

[1] C: color, L: weak isospin, Y: weak hypercharge

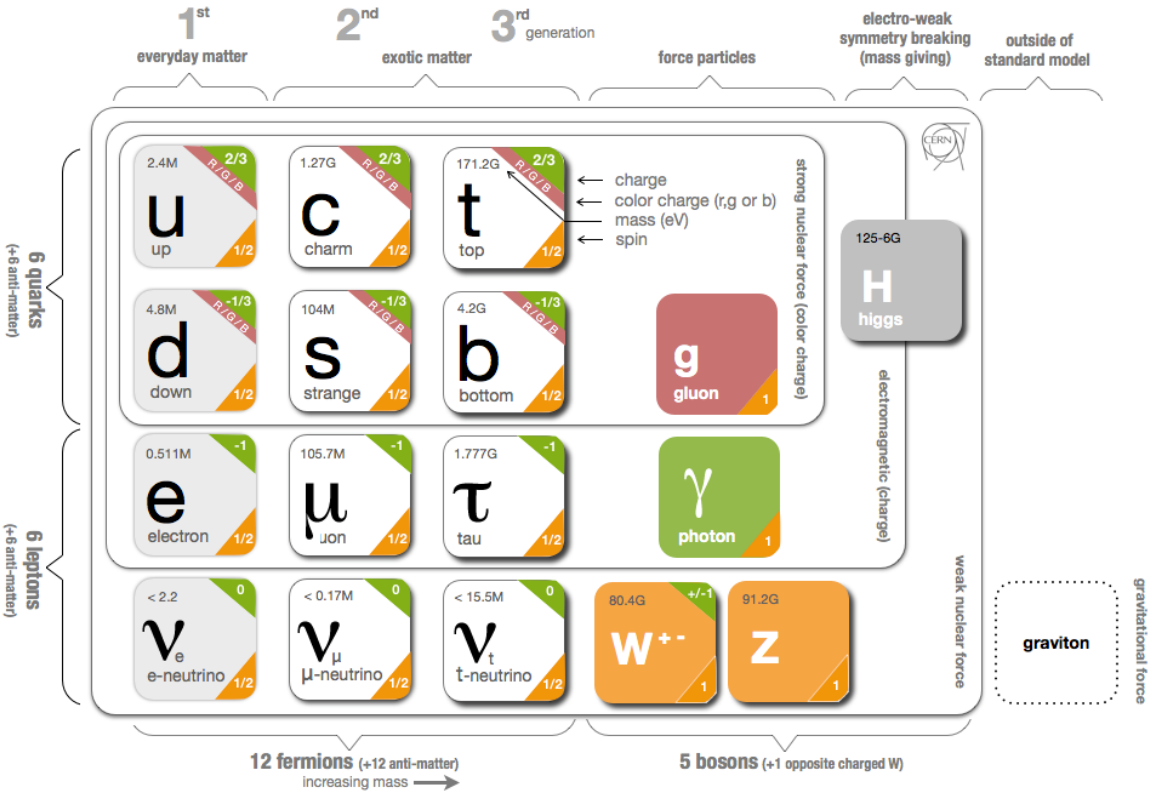

Figure 2.1: Table of the elementary particles of the standard model [1].

neutrino (ν_μ), and tau neutrino (ν_τ)) [20]. They underlie only the weak interaction. Quarks and gluons have a property called color [21]. These color charged particles interact with each other by exchanging gluons in strong interactions. The theory that explains interactions between color charged particles is called quantum chromodynamics (QCD). Quarks can change their color charges by exchanging gluons with other quarks. A single quark can not be found individually; however, quarks are able to form other colorless particles by means of the strong color couplings [22]. The new particles made of quarks by that process are called hadrons [23]. Hadrons are categorized into two types: mesons (combination of quark-antiquark) and baryons (combination of three quarks) [23]. In addition to these

quark-antiquark or quark-quark-quark combination of "valence quarks" hadrons contain gluons and a "sea" of quark-antiquark pairs. The electromagnetic interaction is represented by the exchange of photons [24]. The weak interaction is represented by the exchange of the vector bosons, $W^{\pm}$ and Z [24]. One of the most important hypothetical particle called Higgs boson was discovered by the CMS and ATLAS experiments at CERN [25]. The Higgs boson provides a mechanism that makes elementary particles have different masses.

2.2 Electroweak Theory

The electroweak interaction unifies the electromagnetism and weak interactions that is based on the combination of $SU(2)_L \otimes U(1)_Y$ gauge symmetry group. There are three W bosons (W^+, W^0, and W^-) corresponding to gauge bosons from $SU(2)_L$, and the B^0 boson from $U(1)_Y$, respectively. We will see later that the Z and γ are hidden here. They will acquire energy from the spontaneous symmetry breaking discussed below. The Lagrangian for the electroweak interaction is described as the following [26]:

$$\mathcal{L}_{SU(2)_L \otimes U(1)_Y} = \mathcal{L}_{gauge} + \mathcal{L}_{\phi} + \mathcal{L}_{fermion} + \mathcal{L}_{Yukawa} \tag{2.1}$$

The gauge term describe the interaction between three W bosons and the B^0 boson as:

$$\mathcal{L}_{gauge} = -\frac{1}{4} W^i_{\mu\nu} W^{\mu\nu i} - \frac{1}{4} B_{\mu\nu} B^{\mu\nu} \tag{2.2}$$

where $W^i_{\mu\nu}$ and $B_{\mu\nu}$ can be expressed as:

$$\begin{aligned} B_{\mu\nu} &= \partial_\mu B_\nu - \partial_\nu B_\mu \\ W^i_{\mu\nu} &= \partial_\mu W^i_\nu - \partial_\nu W^i_\mu - g\epsilon_{ijk} W^j_\mu W^k_\nu \end{aligned} \tag{2.3}$$

where $W^{\mu\nu i}$ (i = 1, 2, 3) and $B^{\mu\nu}$ are field strength tensor for the weak isospin and weak hypercharge fields, respectively. g is the coupling constant to the $SU(2)_L$, and ϵ_{ijk} is the antisymmetric tensor. The gauge Lagrangian gives rise to triple and quartic gauge boson couplings. It is important that the $SU(2)_L$ gauge field does not generate any neutral vertex with only Z bosons and photons [19]. The presence of such vertices with Z bosons and photons is predicted by theories beyond the SM [12].

The second term of the Lagrangian is the scalar part:

$$\mathcal{L}_\phi = (D^\mu \phi)^\dagger D_\mu \phi - V(\phi) \tag{2.4}$$

The ϕ is a complex Higgs scalar that is expressed as:

$$\phi = \begin{pmatrix} \phi^+ \\ \phi^- \end{pmatrix} \tag{2.5}$$

The gauge covariant derivative is expressed as:

$$D_\mu \phi = \left(\partial_\mu + ig\frac{\tau^i}{2} W_\mu^i + \frac{ig'}{2} B_\mu \right) \phi \tag{2.6}$$

where the τ^i are the Pauli matrices. The square of the covariant derivative meant that there are three and four point interactions between the gauge and scalar fields.

The $V(\phi)$ is the potential energy of the Higgs field.

$$V(\phi) = \mu^2 \phi^\dagger \phi + \lambda (\phi^\dagger \phi)^2 \tag{2.7}$$

where the λ (> 0) term describes a quartic self-interaction between the scalar fields, and spontaneous symmetry breaking occurs for $\mu^2 < 0$.

The other terms ($\mathcal{L}_{fermion}$ and $\mathcal{L}_{Yukawa}$) in Equation 2.1 are not discussed in this thesis, and details about them can be found elsewhere [26].

Electroweak Symmetry Breaking and the Higgs Mechanism

The gauge term does not involve any mass terms because they are not allowed by the gauge invariance of the Lagrangian for the gauge bosons. However, the experimental observations of the weak interactions show that $W^{\pm}$ and Z gauge bosons have masses while the photon is massless [2] and hence the gauge invariance has to be spontaneously broken. In the electroweak theory, the spontaneous symmetry breaking of the Higgs field creates the difference between the physical $W^{\pm}$, Z, and γ boson masses. The complex Higgs ϕ is doublet with four components [29]:

$$\phi = \begin{pmatrix} \phi^{+} \\ \phi^{-} \end{pmatrix} = \frac{1}{\sqrt{2}} \begin{pmatrix} (\phi_1 - i\phi_2) \\ (\phi_3 - i\phi_4) \end{pmatrix} \tag{2.8}$$

The potential energy of the Higgs field, Equation 2.7, becomes:

$$V(\phi) = \mu^2 \phi^{\dagger}\phi + \lambda(\phi^{\dagger}\phi)^2 = \frac{1}{2}\mu^2 \left(\sum_{i=1}^{4} \phi_i^2 \right) + \frac{1}{4}\lambda \left(\sum_{i=1}^{4} \phi_i^2 \right)^2 \tag{2.9}$$

The Higgs potential energy has a minimum for any ϕ_i that satisfies $\langle 0|\phi_i|0\rangle = (-\mu^2/\lambda)^{1/2}$ [29]. We are able to choose the axis in the four dimensional space without loss of generality so that $\langle 0|\phi_i|0\rangle = 0$ for i = 1, 2, 4 and $\langle 0|\phi_3|0\rangle = \nu$ where ν is the vacuum expectation value [29]. Therefore,

$$V(\phi) \rightarrow V(\nu) = \frac{1}{2}\mu^2\nu^2 + \frac{1}{4}\lambda\nu^4 \tag{2.10}$$

The sign of μ^2 is considered at the minimum of the potential as shown in Figure 2.2. For $\mu^2 > 0$, the potential has the minimum at $\nu = 0$, so the vacuum is empty space and the electroweak symmetry is unbroken. For $\mu^2 < 0$, the potential has the minimum at $\nu = (-\mu^2/\lambda)^{1/2}$, and the electroweak symmetry is spontaneously broken.

[2] W and Z bosons were discovered in 1983 with UA1 and UA2 experiments at the CERN Super Proton Synchroton (SPS) [27, 28]. The mass of W boson is 80.4 GeV and the mass of Z boson is 91.2 GeV.

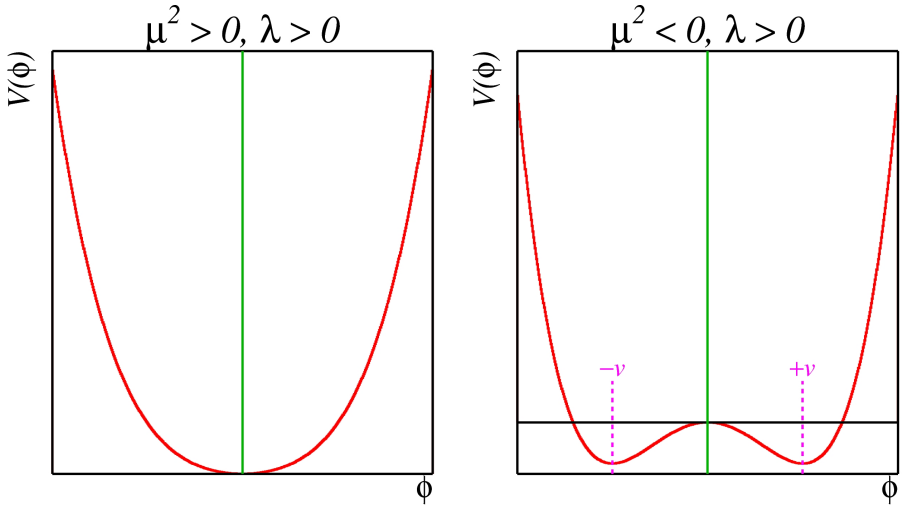

Figure 2.2: The Higgs potential $V(\phi)$ for $\mu^2 > 0$ (right) and $\mu^2 < 0$ (left) [2].

The Higgs field is written as [30]:

$$\phi = \frac{1}{\sqrt{2}} \begin{pmatrix} 0 \\ \nu + H \end{pmatrix} \tag{2.11}$$

where H is the scalar field that describes a physical Higgs boson. The Higgs term ($\mathcal{L}_\phi$) in the Lagrangian takes the form:

$$\mathcal{L}_\phi = (D^\mu \phi)^\dagger D_\mu \phi - V(\phi) = M_W^2 W^{\mu +} W_\mu^- \left(1 + \frac{H}{\nu}\right)^2 + \frac{1}{2} M_Z^2 Z^\nu Z_\nu \left(1 + \frac{H}{\nu}\right)^2 + \tfrac{1}{2}(\partial_\mu H)^2 - V(\phi) \tag{2.12}$$

where

$$W_\mu^\pm = \frac{W_\mu^1 \mp i W_\mu^2}{\sqrt{2}} \tag{2.13}$$

$$Z_\mu = W_\mu^3 cos\theta_W - B_\mu sin\theta_W \tag{2.14}$$

Equation 2.13 to 2.14 correspond to the physical fields of the charged W bosons ($W^\pm$) and

the neutral Z boson, respectively. The θ_W is the Weinberg angle that connects the $SU(2)_L$ and the $U(1)_Y$ coupling constants [6]. Their masses are expressed as:

$$M_W = \frac{g\nu}{2} \tag{2.15}$$

$$M_Z = \frac{M_W}{cos\theta_W} \tag{2.16}$$

The physical fields of photon is expressed as:

$$A_\mu = W^3_\mu sin\theta_W + B_\mu cos\theta_W \tag{2.17}$$

and its mass is zero.

2.3 $Z\gamma\gamma$ Production at the LHC

The study of the production of Z boson in association with two photons ($Z\gamma\gamma$) in proton-proton collisions at the LHC provides an important test of the SM at the TeV energy. In the SM, a Z boson and a pair of photons can be produced via a non-resonant process. The $Z\gamma\gamma$ production at proton-proton collisions is from quark-antiquark annihilation. The allowed Feynman diagrams of the SM for $Z\gamma\gamma \to \ell\ell\gamma\gamma$, where ℓ is a muon or electron, processes are shown in Figure 2.3. The process where photons are emitted by the interacting partons is called the initial state radiation (ISR) is shown in Figure 2.3 (a), and the process where photons are emitted by charged leptons in the final state is called final state radiation (FSR) is shown in Figure 2.3 (b). In addition to the process when one photon is from ISR and an another photon is from FSR process (ISR + FSR) is shown in Figure 2.3 (c). In this dissertation, we collectively refer to the process as $Z\gamma\gamma \to \ell\ell\gamma\gamma$ in the charged leptonic channel. The events from τ decay ($Z\gamma\gamma \to \tau\tau\gamma\gamma \to \ell\nu\nu\ell\nu\nu\gamma\gamma$) are subtracted from signal events.

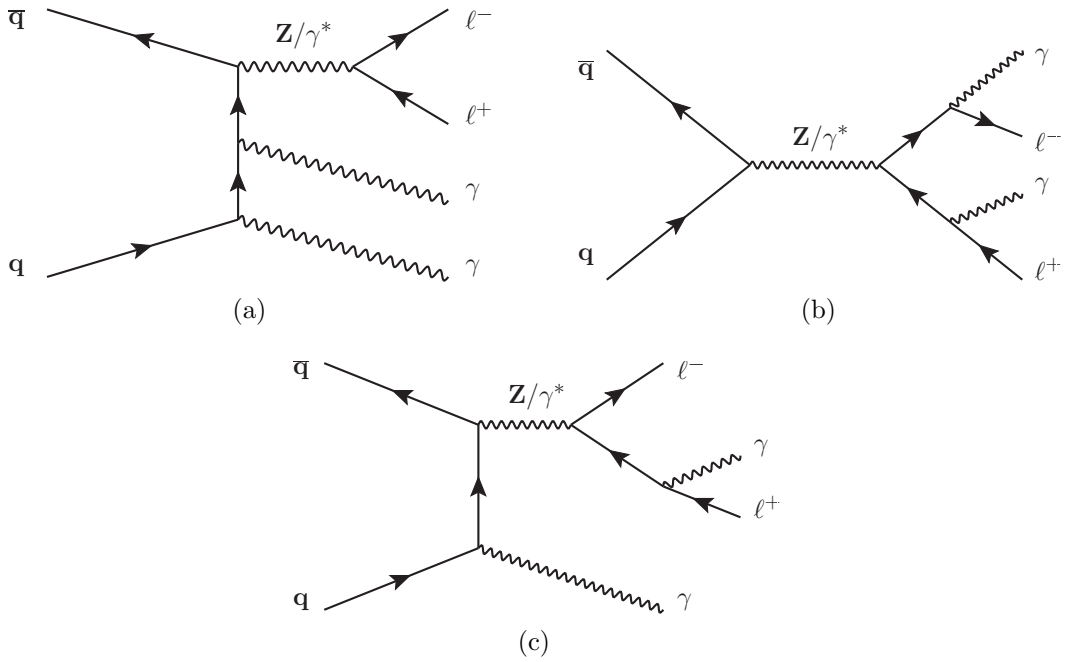

Figure 2.3: Some of the Feynman diagrams that describe leading order $pp \to \ell\ell\gamma\gamma$ production: ISR (a), FSR (b), and an ISR and FSR (c) production.

2.4 Previous Study at LEP

The study of Z$\gamma\gamma$ production have been performed at low-energy e^+e^- collisions at the LEP collider by the L3 collaboration [13]. The cross section of the process $e^+e^- \to Z\gamma\gamma$ is measured using L3 data taken at a center of mass energies of 182.7 GeV and 188.7 GeV, corresponding to an integrated luminosity of 231 pb^{-1}. Their studies given to the measurement of the Z$\gamma\gamma$ production cross section at e^+e^- collisions is summarized in Table 2.1.

Center of mass energy	$\sigma\,(e^+e^- \to Z\gamma\gamma)$ fb (stat., syst.)
182.7 GeV	$0.49\ ^{+0.20}_{-0.17} \pm 0.04$ pb
188.7 GeV	$0.47 \pm 0.10 \pm 0.04$ pb

Table 2.1: The measured cross section for the Z$\gamma\gamma$ production at $\sqrt{s}$ = 182.7 GeV and $\sqrt{s}$ = 188.7 GeV at LEP experiment [13]. Two uncertainties are determined that originate from data statistics uncertainty and systematic uncertainty, respectively.

Chapter 3

Experimental Setup

The following introduction on the experimental apparatus of the LHC and the CMS detector parallels similar discussion presented elsewhere [6, 12].

3.1 The Large Hadron Collider

The LHC is designed to collide protons at center of mass energy of $\sqrt{s} = 14\,\text{TeV}$ with high instantaneous luminosity of $\mathcal{L} = 10^{34}\,cm^{-2}\,s^{-1}$ [31] that is operated by the European Organization for Nuclear Research (CERN). [1] The performance is able to be accomplished with an injector complex [32] (see Figure 3.1) followed by the 27 km LHC main ring located 100 meters beneath the ground. In the LHC main ring, the superconducting coils are cooled by super-fluid helium to a temperature of 1.9 K to provide a magnetic field at 8.3 Tesla to bend the proton beams [33]. This injector complex is designed for the protons to be accelerated to an energy up to a maximum of 7 TeV that result in 14 TeV center of mass energy. The injector system consists of the Linac2, the Proton Synchrotron Booster (PSB), the Proton Synchrotron (PS) and the Super Proton Synchrotron (SPS), which accelerates the protons with energy from 50 GeV to 450 GeV [33].

[1] CERN is the world largest international laboratory of particle physics. It was founded in 1954 in a northwest suburb of Geneva, Switzerland.

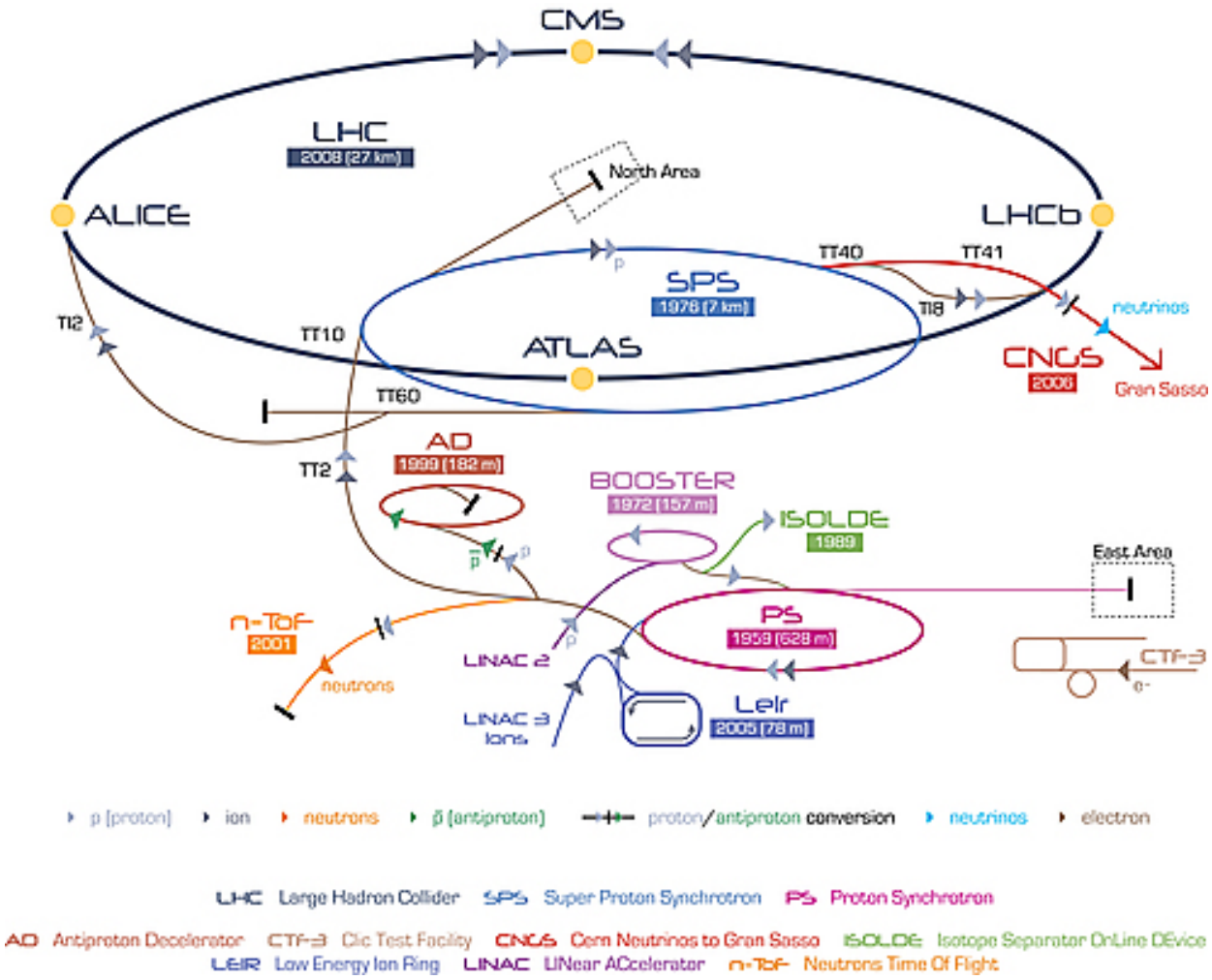

Figure 3.1: The CERN accelerator complex. Four interaction points, where the CMS, the ATLAS, the ALICE, and the LHCb detectors are located in the ring [3].

There are several detectors are located around the LHC ring. The CMS detector will be discussed in great detail in the following sections in Chapter 3. The ATLAS (A Toroidal LHC ApparatusS) [34] detector is designed to search for the Higgs boson [2] and supersymmetric particle (SUSY) [36] in addition SM search. The LHCb (Large Hadron Collider beauty experiment) [37] detector is dedicated to B-physics [38]. The ALICE (A Large Ion Collider Experiment) [39] detector is designed for the study of heavy ion collisions.

[2]Higgs boson was observed by the CMS and ATLAS experiments at LHC in 2012. Its mass is approximately 125 GeV [35].

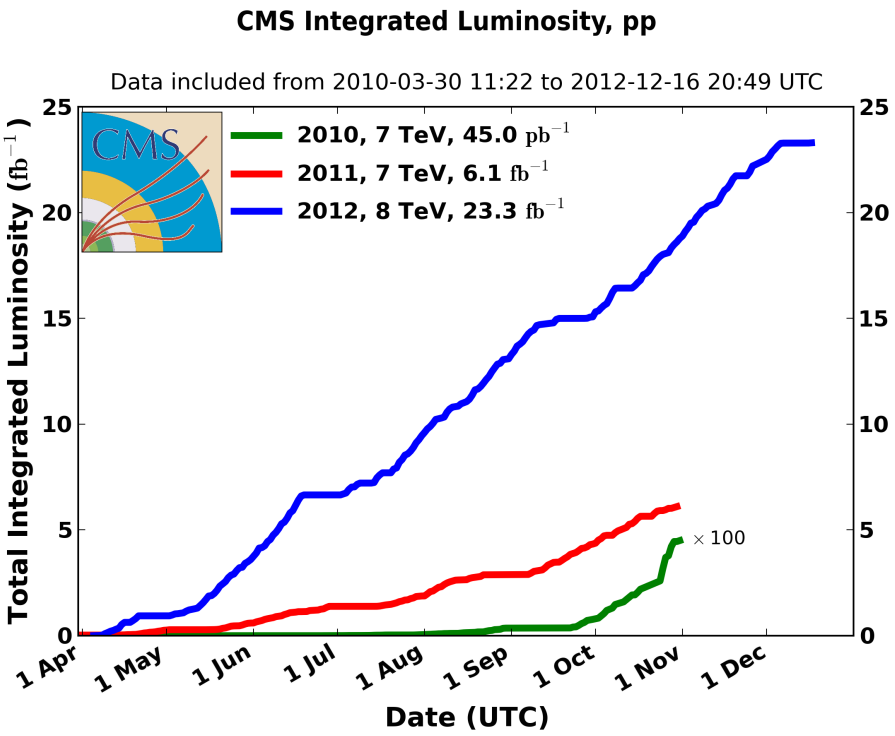

Figure 3.2: Total integrated luminosity with CMS experiment for 2010, 2011, and 2012 [4].

The LHC started working on March in 2010, and it ran at 7 TeV (3.5 TeV per proton beam) in 2010 - 2011 and at 8 TeV (4.0 TeV per proton beam) in 2012 [40]. This successful operation resulted in 6.1 fb^{-1} and 23.3 fb^{-1} integrated luminosity with the CMS experiment in the year of 2011 and 2012 [4], see Figure 3.2. The LHC's first run was officially ended in 2013. Its second run restarted at the center of mass energy up to 13 TeV (6.5 TeV per beam) in June 2015 after two years of maintenance and upgrading [41].

3.2 The CMS detector

3.2.1 Overview and Coordinate System

The CMS detector is located 100 m under the ground [7] at the LHC interaction point 5 in the French side of the CERN. It covers almost the whole solid angle around the proton-proton

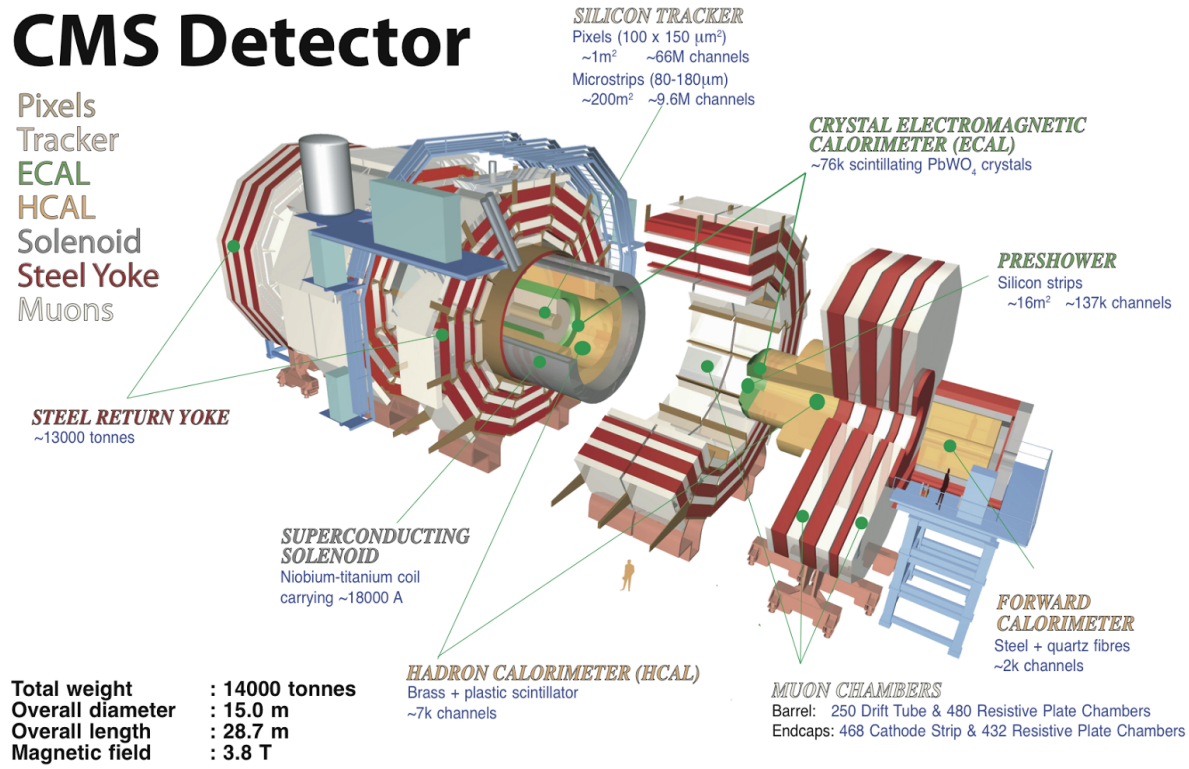

Figure 3.3: The CMS detector consists of silicon pixel and strip tracker, electromagnetic calorimeter, hadron calorimeter, superconducting solenoid, and muon chamber. It is 28.7 m in length with 15 m diameter. The overall weight of the detector is 14,000 tons [5].

collision point [7] with layers of silicon pixel and strip tracker, electromagnetic calorimeter (ECAL), hadron calorimeter (HCAL), superconducting solenoid, and muon chamber. Figure 3.3 illustrates the structure of the CMS detector. The CMS detector is designed to search for the Higgs boson and supersymmetric particles (SUSY) in additional to Standard Model searches similar to the ATLAS detector. The various components of the CMS detector work together to identify the final state of objects such as electrons, muons, photons, hadron-jets, hadronically decaying τ leptons, and b-jets in proton interactions. The measurement of the $Z\gamma\gamma$ production cross section makes use of electrons, muons, and photons reconstructed with the CMS detector.

In the right-hand CMS coordinate system, the z coordinate points along counter-clockwise direction around the beam line, the x coordinate towards the center of the LHC ring, and the y coordinate is the vertical axis pointing up [7], see Figure 3.4. In this system, pseudorapidity, $\eta = -\ln(\tan\theta/2)$, is calculated by the polar angle θ which is defined with respect to the z axis [7]. Transverse momentum, $p_{\mathrm{T}} = p\sin\theta$, and energy, $E_T = E\sin\theta$ are calculated from the polar angle theta and the total p and E [7]. The azimuthal angle ϕ is defined with respect to the x axis. In this analysis, the distance, ΔR, between two particles are evaluated in the $\eta - \phi$ plane with $\Delta\mathrm{R} = \sqrt{\eta^2 + \phi^2}$ [42]. Isolation of a particle is defined from the sum of p_{T} of other particles around it within a cone with ΔR [43]. Three different types of isolation are calculated separately: charged hadron isolation, neutral hadron isolation, and photon isolation.

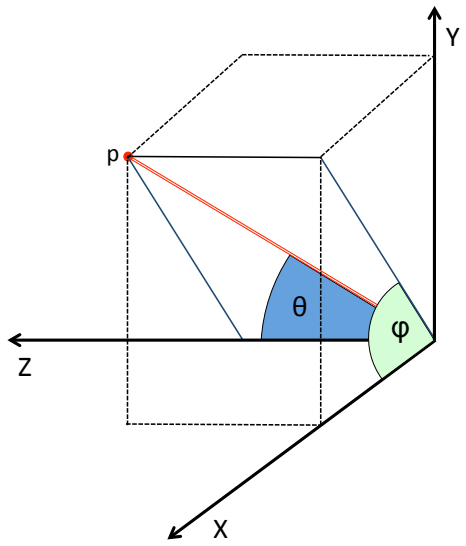

Figure 3.4: Cartesian and spherical system of coordinates for CMS detector [6].

3.2.2 Superconducting Magnet

The CMS detector uses a large superconducting solenoid magnet, 12.5 m in length with 6.3 m diameter and 220 metric tons in mass [44], to produce a uniform magnetic field in

the inner detector region. Figure 3.5 shows the perspective view of the solenoid magnet. This magnetic field bends charged particles passing the inner detector to determine their momenta. This superconducting solenoid magnet is made of niobium-titanium alloy to handle a strong magnetic field, 3.8 T with large amount of current, 20 kA [44]. The magnetic flux is returned through a supported iron yoke with 2 T magnetic field [44]. This yoke consists of 5 wheels in the barrel and 3 disks in each endcap [44].

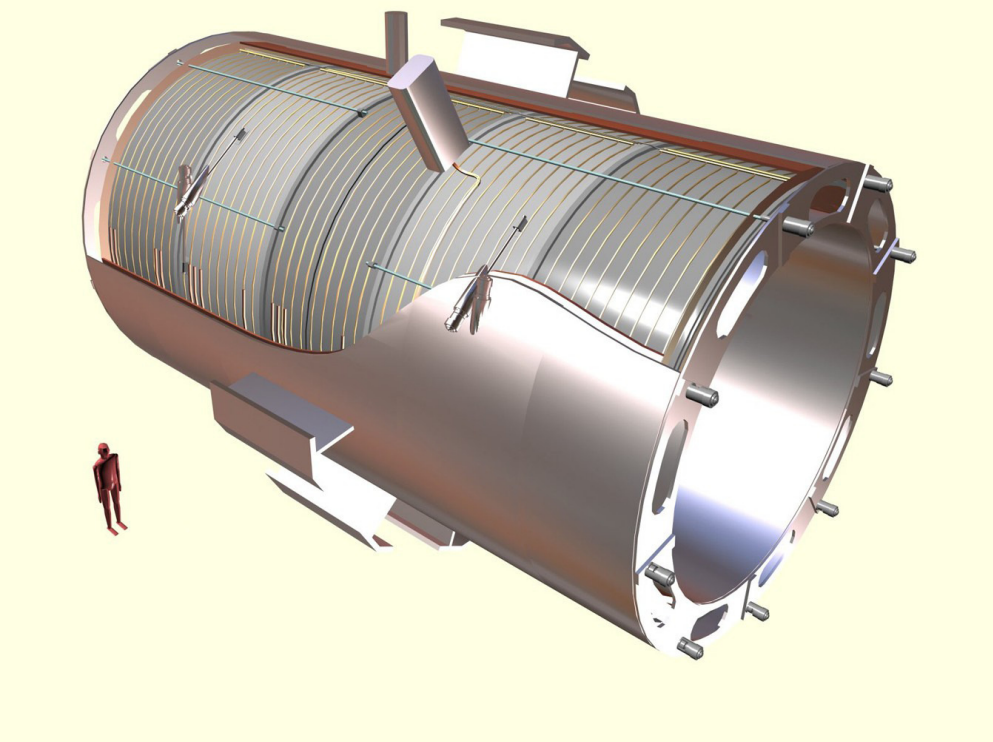

Figure 3.5: A perspective view of the solenoid magnet [7].

3.2.3 Inner Tracker

The CMS tracker is located at the center of the CMS detector near the interaction point. It is 5.8 m in length, 2.6 m in diameter and consists of 25,000 silicon strip sensors [45]. The tracker measures the direction of particle tracks and provides the primary and secondary vertex information of particles. The transverse momentum of a particle is calculated by

measuring the radius of curvature in a magnetic field. The tracker can reconstruct the charged particles such as electrons, muons, and hadrons passing through the detector. The CMS tracker is comprised of two different systems: the Silicon Pixel Detector and Silicon Strip Detector that are composed of silicon and register charged particle. A charged particle knocks electrons out of the material in the pixel detector, and then it creates a net positive charge on the pixel. The silicon is returned to its neutral state by an electric current. That electric current is amplified and measured by the readout electronics [46].

Silicon Pixel Detector

The silicon pixel detector consists of 65 million pixels distributed in three cylindrical barrel layers at radii of 4, 7, and 11 cm and two disks in each endcap at 6 and 15 cm from the interaction point [47]. Figure 3.6 illustrates the overall silicon pixel detector. A single pixel measures 100 μm x 150 μm [47], with each pixel being read out by a dedicated chip attached to the module. The energy of a charged particle hitting the surface of a pixel is collected as a small electric signal. Each silicon chip has an amplifier, which boosts the electrical signal.

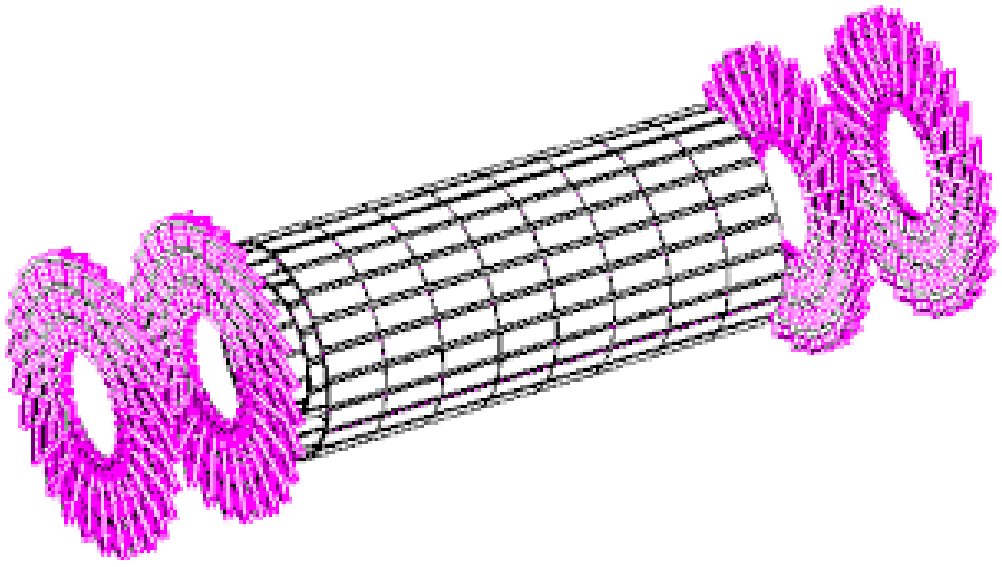

Figure 3.6: A perspective view of the CMS pixel system [8].

Silicon Strip Detector

The silicon strip detector consists of 15,200 silicon strip modules with 10 million strips in 10 layers of strips in both the barrel and endcap. It covers $|\eta| < 2.5$ in the pseudorapidity range and its radius is 130 cm [48] from the interaction point. The silicon strip detector is comprised of four different subsystems, the four inner barrel (TIB) layers reaching to 50 cm in a radius, the inner endcap disks (TID) consisting of three layers to $\pm$90 cm in Z coordinate, the outer barrel (TOB) with six concentric layers to 1.16 m radially, and the outer endcap (TEC) consisting of nine layers extending to $\pm$2.8 m in Z coordinate [46]. Each subsystem has different design silicon modules for its place within the detector. Figure 3.7 shows the schematic layout of the entire CMS tracker system.

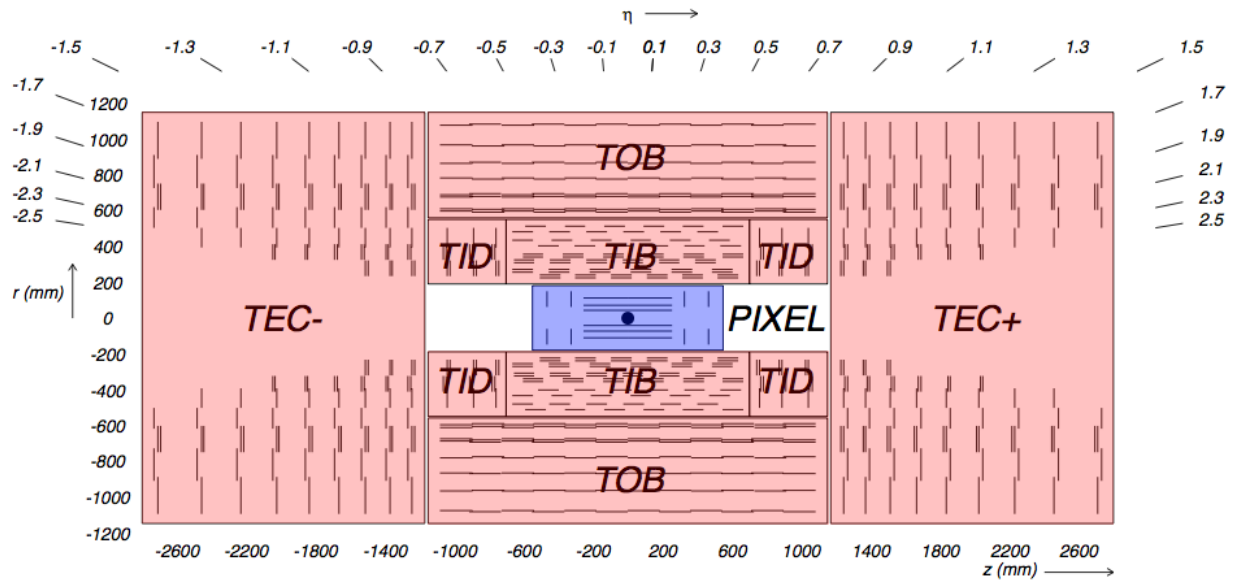

Figure 3.7: A schematic view of the CMS inner tracker tracker [9].

3.2.4 Calorimeters

The CMS calorimeter is comprised of Electromagnetic Calorimeter (ECAL) and Hadronic Calorimeter (HCAL) to measure energies of particles passing through the detector. The

ECAL is located outside the tracker and the HCAL surrounds the ECAL. Both of calorimetrs are located within the solenoid.

Electromagnetic Calorimeter

The ECAL is a homogeneous calorimeter made of 61,200 lead tungstate (PbWO4) scintillating crystals in the central barrel ($|\eta|$ <1.479) and 7,324 crystals in endcaps ($1.479 < |\eta| < 3.0$) [49] in order to measure energies of electromagnetic showers from electrons and photons with a high precision. The electromagnetic component of jets mostly due to $\pi^0 \to \gamma\gamma$ is also included. Each crystal is 2.2 cm x 2.2 cm in width and 23 cm in length for barrel, and 3 cm x 3 cm in width and 22 cm in length for endcap [49]. This material is chosen due to the small radiation length X_0 (0.89 cm) [3] [49] and small Moliere radius R_M (2.2 cm) [4] [49] that simultaneously ensure good response times and granularity. To measure the scintillation light, avalanche photon diodes (APD) are used in barrel region. The scintillation light translates to the energy deposit. The APDs is less efficient in endcap region due to the large amount of radiation, thus vacuum phototriodes (VPT) are used instead [49]. To enhance photon identification capabilities, a preshower detector is placed between the inner tracker and the crystal calorimeter in the range approximately $1.65 < |\eta| < 2.6$ [49]. Its total thickness is 20 cm [50] and consist of two layers of lead that are used to reject the some of background events from π^0 decay and improve the photon identification. The ECAL energy resolution for particles are measured to be [49]:

$$\left(\frac{\sigma_E}{E}\right)^2 = \left(\frac{2.8\%}{\sqrt{E/GeV}}\right)^2 + \left(\frac{12\%}{E/GeV}\right)^2 + (0.3\%)^2\,, \tag{3.1}$$

[3] The radiation length is the average distance which the electron to reduce its initial energy by a factor of 1/e due to radiation losses. It is defined by $X_0 = \frac{716.4 g/cm^{-2} A}{Z(Z+1)\ln 287/\sqrt{Z}}$ where Z is the atomic number and A is the mass number.

[4] The Moliere radius is a characteristic constant of a material to be indicative of the transverse dimension of electromagnetic showers.

where the three contributions are corresponding to the stochastic, noise, and constant terms, respectively. Figure 3.8 shows the schematic layout of the CMS ECAL detector.

Hadronic Calorimeter

The HCAL main purpose is to measure the energy of hadronic jets and other hadronic objects that have passed through the ECAL from proton-proton collision. The overall HCAL is comprised of four sub-components: the barrel (HB), the endcap (HE), the outer (HO), and the forward (HF) calorimeters. Figure 3.9 shows the longitudinal view of the CMS HCAL detector. HB and HE cover $|\eta| < 3.0$ and up to $|\eta| < 5.0$ in HF, both within the solenoid magnet [51]. HO is filled outside of the solenoid magnet to measure the energy leakage from HB [51]. The CMS HCAL uses sampling calorimeter where absorber material is brass and active material is plastic scintillator in barrel and endcap region. Steel plates and quartz fibers are used for HF. The scintillation light is read out by wavelength-shifting fibers and the signals by a hybrid photodiode (HPD) in a sampling calorimeter [51]. Since some energies are not detected in the material, the energy measurement is scaled with experimentally determined factors. The depth of the HCAL with respect to the interaction length (λ_I) of hadrons varies 5.82 to 10.6 λ_I [52] at depend on the angle η. The HCAL depth is extended to 11.8 λ_I [52] at $|\eta| < 1.3$ for the HO. Finally, the additional component HF covers $|\eta| < 5.2$ [51]. Two different lengths of quartz fibers are ready to discriminate electromagnetic objects from hadronic jets [51]. The long fibers, reach to approximately 10 λ_I, measure the hadronic showers coming from the full HF, whereas the short fibers measure the electromagnetic showers after 22 cm of steel [51].

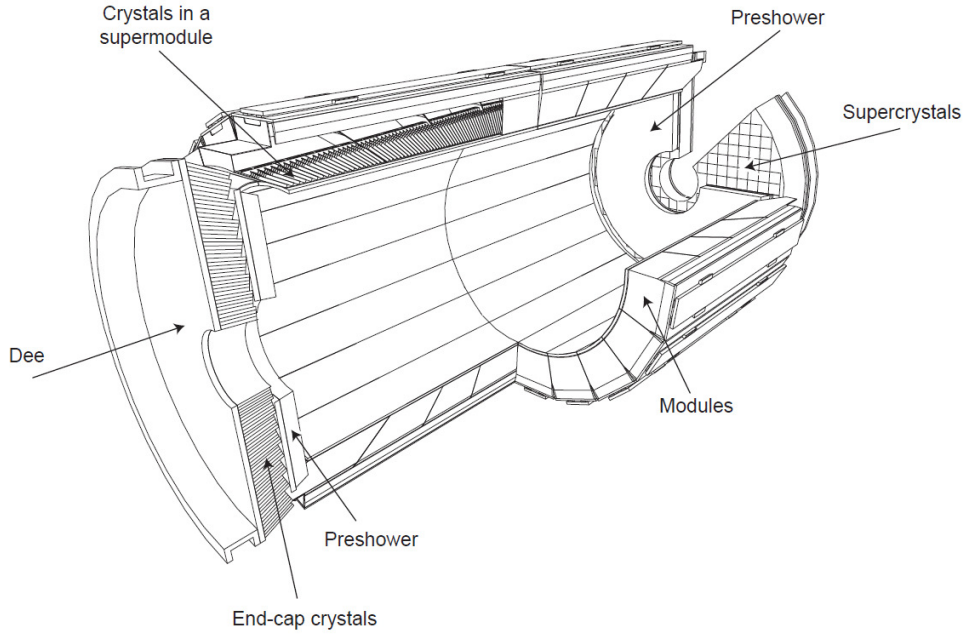

(a)

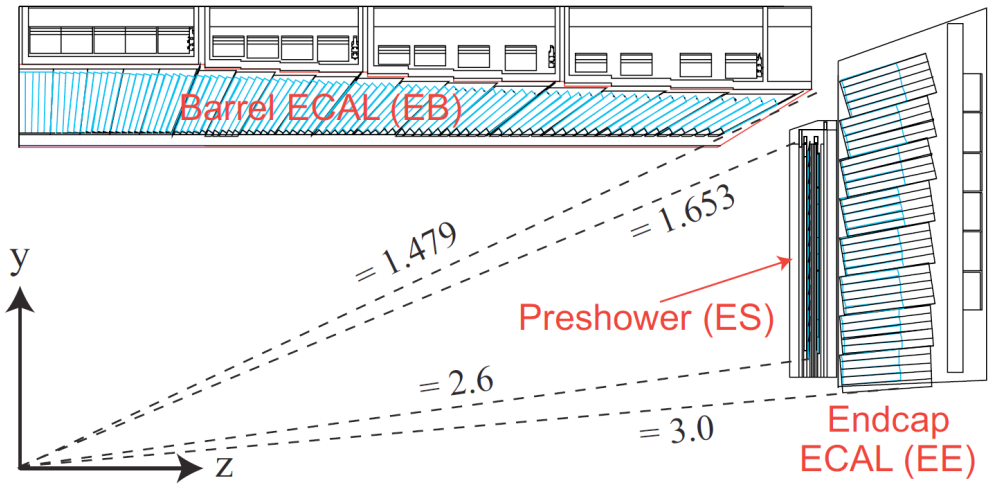

(b)

Figure 3.8: A schematic layout of the CMS electromagnetic calorimeter showing the arrangement of crystal modules, supermodules, endcap crystals, and preshower (a), and a longitudinal view of the CMS electromagnetic calorimeter (b) [10].

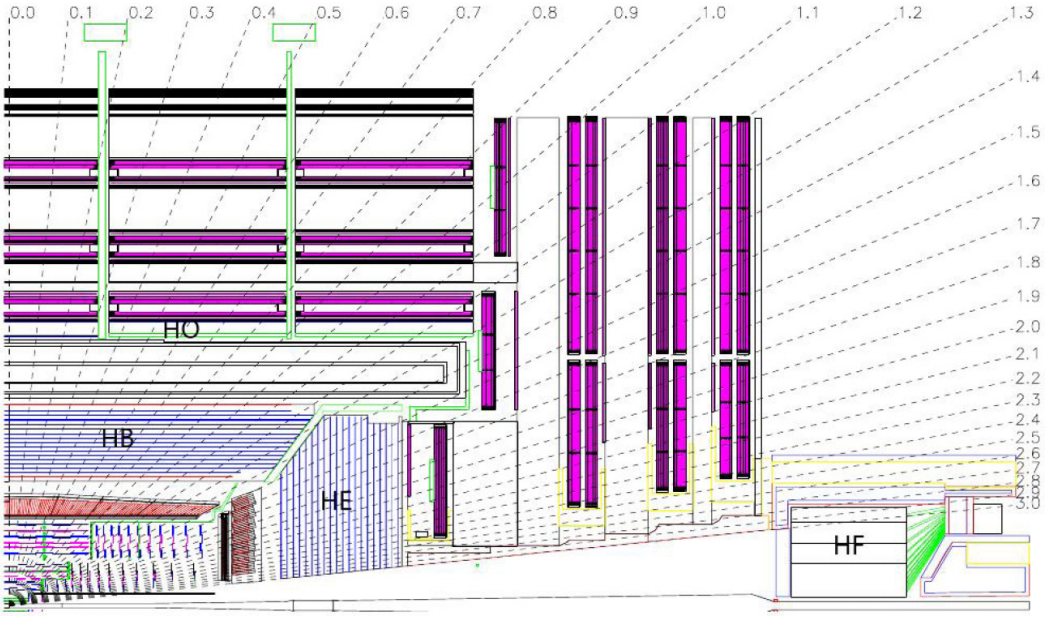

Figure 3.9: Longitudinal view of the CMS hadron calorimeter, showing the position of hadron barrel (HB), hadron endcap (HE), and hadron forward (HF) [10].

3.2.5 Muon Detector System

The CMS Muon detector system is located outside of the solenoid magnet and provides muon [5] track reconstruction and muon identification. Observing muon, as the middle name of CMS detector suggests, is one of the important task at the CMS experiment. Most of muons pass through CMS calorimeter, so that we can not measure muon energy through deposition. Therefore, the muon momentum is measured by the precise track reconstruction. The CMS muon system is comprised of three different systems: 250 drift tube (DTs) chambers, 610 resistive plate chambers (RPCs), and 540 cathode strip chambers (CSCs) [54]. Figure 3.10 shows the longitudinal layout of CMS muon detector system. These are attached to the return yokes in four layers and four layers of disks in the barrel and endcap regions, respectively.

[5] Muons are charged particles that are 200 times heavier than electrons [53].

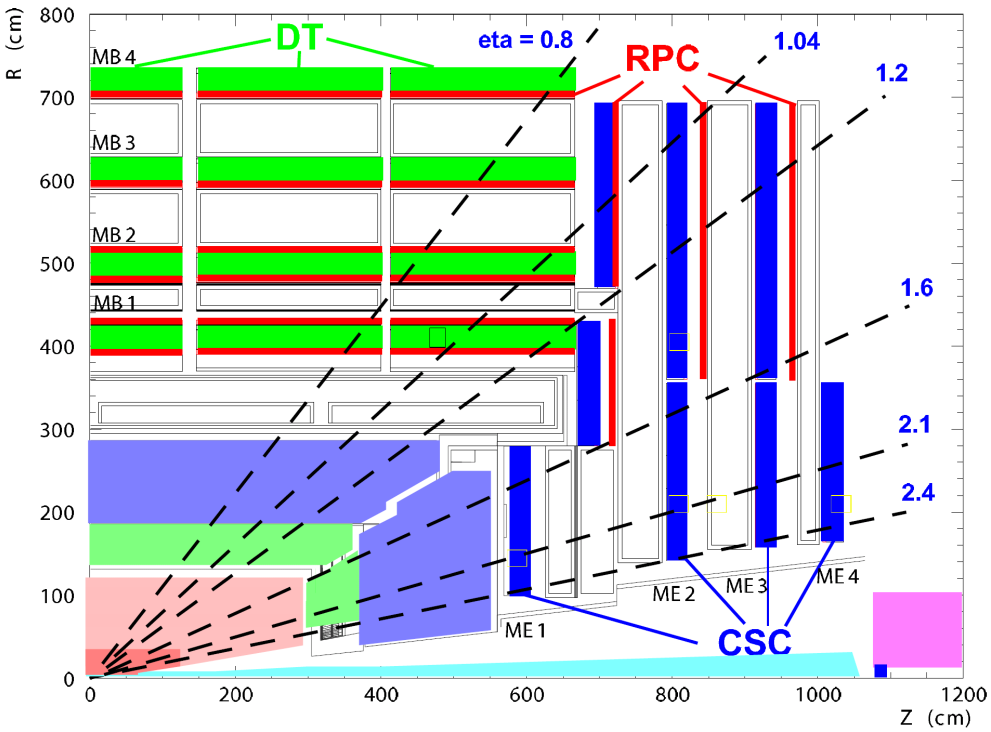

Figure 3.10: A longitudinal view of the muon detector system [10].

Drift tubes

The DTs are filled with 85% of Ar and 15% of CO_2 gas mixture at $|\eta| < 1.2$ between the iron return yoke plates [6]. They measure the muon positions in the barrel region. The DTs consist of 12 aluminum layers in three groups of four [55]. The middle group can measure the muon position in Z direction, and the two outside groups can measure the muon position in $r - \phi$ direction. The muon position in the $r - \phi$ direction is determined by the 8 layers of DT cells in the outermost muon station.

Cathode strip chambers

The 4 CSC stations are located in the muon detector endcap at $0.9 < |\eta| < 2.4$ overlapping slightly with the DTs [55]. The CSCs are trapezoidal shaped and composed of 7 layers of copper strips cathode panel [55]. Anode wire planes are placed perpendicularly to those

copper strips in 40% of Ar, 50% of CO_2, and 10% of CF_4 gas mixture filled gaps between each layer [55]. The muon position is measured in ϕ direction with the copper strips and in r direction with the anode wire.

Resistive plate chambers

The RPCs provide much faster response with time resolution of about 1 ns for the muon trigger system [6]. In the barrel region, 6 layers of RPCs are installed [56]. There are two layers in each of the first two drift tube stations, and only one layer is installed in each of the last two outer stations. Additionally, one layer of RPCs is installed in each of the first three stations of endcap. This, the RPCs are placed in the barrel and endcap region at $|\eta| < 1.6$ [6]. The RPCs consist of two parallel plastic plates. The 95% of $C_2H_2F_4$ and 5% of i-C_2H_{10} gas mixture filled and read-out strips are installed in the middle [56].

3.3 Trigger System

Data is produced by proton-proton collisions every 25 ns [57]; however, it is impossible to record all data. The CMS trigger system is designed to choose collision events corresponding to physics of interest before recording data, thus only interesting data are stored. The CMS trigger system is composed of two parts: the level 1 (L1) trigger and high level trigger (HLT) [57]. The L1 trigger analyzes the events very quickly, and the event rate is reduced by the order of 10^3 [58]. Then events of interest are reconstructed and recorded if passed the L1 trigger. L1 trigger derives the track pattern information from the calorimeter and muon detector systems. Figure 3.11 shows overview of the CMS L1 trigger system. The L1 trigger is running on programmable electronics with the Field Programmable Gate Arrays (FPGA) and custom Application Specific Integrated Circuits (ASIC) [58]. All of the detector data have to be kept in pipelines while the trigger decision is made. The events that are selected by the L1 trigger transfer to the HLT machines for the final decision of recording the data.

The HLT runs software-based on a multi-processor filter farm. This system is more flexible to make changes for the objects reconstruction software.

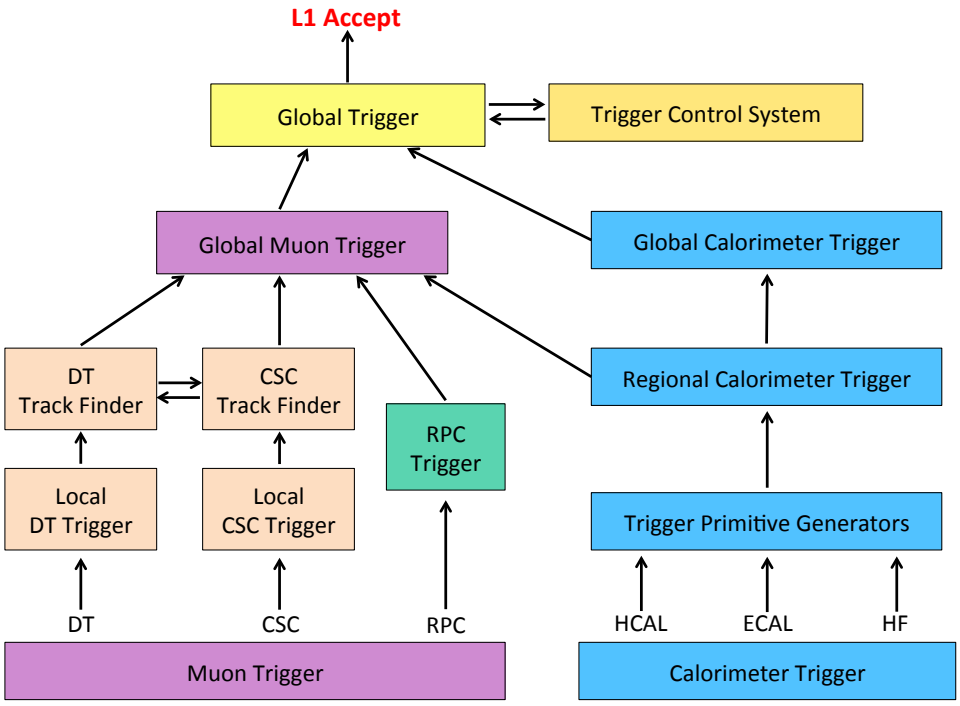

Figure 3.11: Overview of the CMS L1 trigger system [6].

Chapter 4

Event Reconstruction

4.1 Particle Flow Algorithm

The particle flow (PF) events reconstruction is an algorithm which collects information about energy deposits in detectors and the tracks following particle collisions. The algorithm is able to classify and identify all stable particles [59] such as electrons, photons, and muons in these events based on their energy deposited in the detectors and their respective tracks. Then these individual particles are used to build higher level physics objects such as jets [1], hadronic taus, a jet originating from b-quark, missing transverse energy, and charged lepton isolation.

4.2 Photon Reconstruction

Photons and electrons are reconstructed from the measured energy deposited by them in the ECAL. Approximately 94% (97%) of the incident energy of a single electron or photon would be collected within the 3x3 (5x5) crystals (see Figure 4.1) [11]. Due to a significant bremsstraghlung, photons convert to e^+e^- pairs in tracker material. The photon energy

[1] collimated bunches of low energy particles in a quark or gluon fragmentation environment.

cluster in the ECAL surface can be widely spread in the azimuthal direction due to the strong magnetic field. Photons and electrons are reconstructed by building a cluster of clusters in the ECAL to account for these energy spread, called superclusters (SCs).

There are different clustering algorithms used to find SCs in the barrel and endcap region because the difference in their position and their position. The "hybrid" algorithm is used to the $\eta - \phi$ geometry of barrel crystals to exploit the knowledge of lateral shower shape in η direction [60]. The hybrid algorithm makes a group of 5x1 crystals during the separated energy in the ϕ direction is dynamically searched [6]. The "multi5x5" algorithm is used in endcap region to consider the information from the preshower in the ECAL [46]. A 5x5 cluster is obtained to collect the energy and then added other energy deposit within the 5x5 cluster window to form the supercluster within a rectangular $\eta - \phi$ window. The preshower cluster position is extrapolated by the cluster position in endcap region, and total cluster energy in endcap is the sum of cluster energies in preshower and endcap.

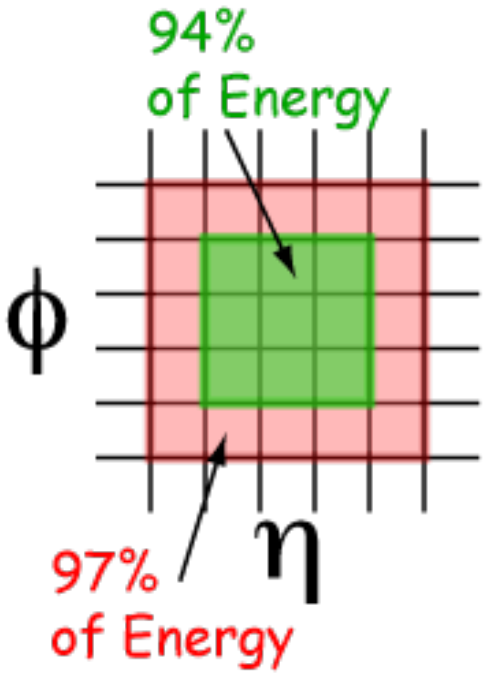

Figure 4.1: Typical energy distribution in a basic cluster [11].

4.3 Electron Reconstruction

Electrons passing through the CMS detector leave a signature pattern in the sub-detectors. Electrons are able to produce tracks in the tracker detector and energy cluster in the ECAL. Therefore the electron reconstruction is starting from energy cluster in ECAL and search for hits in tracker which match to the ECAL cluster position. There are two complementary algorithms used to electron reconstruction: the "ECAL-driven seeding" method and "Tracker-driven seeding" method [2].

The ECAL-driven seeding method starts from an energy cluster in the ECAL to track hits in the pixel detector optimized for isolated and high energy electrons. However, this method does not work well to reconstruct low energy non-isolated electrons in jets.

The tracker-driven seeding is an alternative seeding [3]. by a track that is followed to the ECAL surface to find a match with the ECAL cluster. This method provides better performance for low energy electrons in jets, for which electron energy cluster can be widely spread in the azimuthal direction due to a significant bremsstrahlung photon emission. The tracker-driven seeding is performed in two stages.

The method in the first stage is designed to find the electrons which do not have photon emission within the tracker detector volume. In this method, the good tracking quality is required, as well as good matching quality between reconstructed energy cluster and tracks. Thus, the electron tracks are selected that seed based on requirement in the ratio between the ECAL energy cluster and momentum in the tracker (E_{ECAL}/p_{trk}). The other method detects electrons which emit photons in the tracker volume; this photon emission results in a kink of trajectory of the electron, which typically does not have good quality in the Kalman Filter (KF) [4] track fitting. Matching criteria between tracks and energy clusters are

[2]The Tracker-driven seeding method algorithm was implemented by S. Toda McBride and Y. Maravin for the operation of the LHC complex in 2015 to 2018.

[3]Seeding is a technique to find the tracker hits to start the electron tracking [61].

[4]The KF method is the standard track reconstruction in CMS experiment that is used to expect the location of hits in the next layer of detector by the current known track parameter. The KF algorithm is perfect to perform tracks that do not loose much energy due to radiation loss.

re-optimized to maximize the efficiency for such electrons. The electron tracks are selected when number of hits is small or normalized KF χ^2 is large. Besides the simple cut-based selection, a multivariate analysis using Boosted Decision Tree (BDT) technique is applied to perform electrons with the best efficiency. The KF and the Gaussian Sum Filter (GSF) [5] method comparison is input to a BDT algorithm to collect those electrons. Finally, the electrons are combined with those previously identified from the track-cluster matching to perform the final collection of tracker-driven seeding. Figure 4.2 shows the work-flow of the tracker-driven seeding strategy.

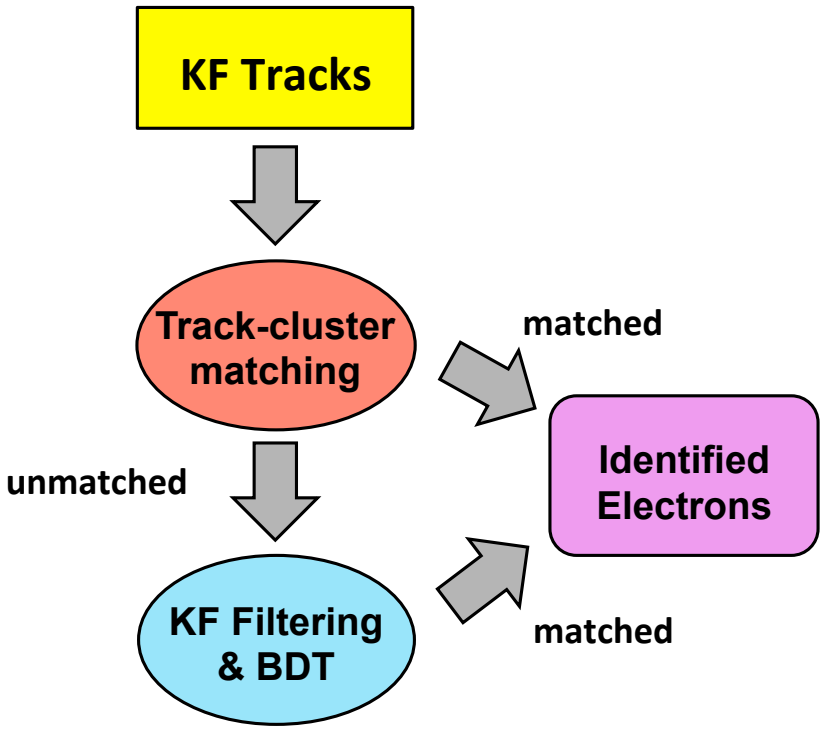

Figure 4.2: Workflow of the electron tracker-driven seeding strategy.

[5]The GSF method as a weighted sum of Gaussian distributions that is able to follow the electron tracks after bremsstrahlung.

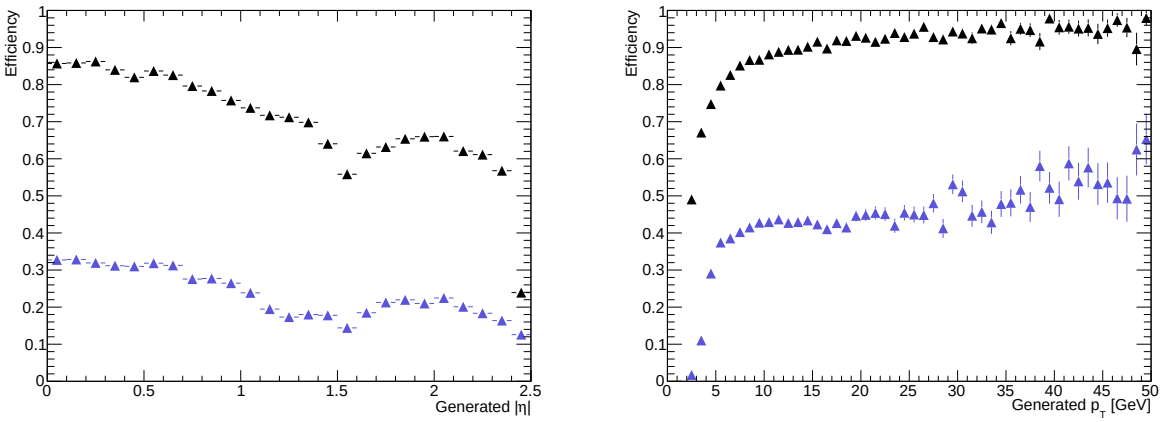

(a) (b)

Figure 4.3: Electron seeding efficiency as a function of the generated η (a) and p_{T} (b) in a b-jet sample. Black triangles indicate seeds found by the tracker-driven and ECAL-driven seeds, and blue triangles indicate seeds found by the ECAL-driven method only. The efficiency is increased by almost a factor of three with an addition of the tracker-driven method.

4.4 Muon Reconstruction

In the CMS experiment, the muon reconstruction is performed in two stages: muon tracks in the tracker detector for the "tracker muons" and muon signals in the muon system for the "stand-alone muons", and combined these of them is called a "global muon" that is the best estimate for the muon reconstruction (see Figure 4.4) [62].

The tracker muon algorithm is used to identify of low energy muons that is not able to leave enough hits in the muon station. If extrapolated track to the muon station is compatible with at least one segment, this track is considered the tracker muon [6].

For the stand-alone muon reconstruction uses to collect data from only muon system that starts from the track segments in the muon chambers [63]. The muon track position, direction, and momentum that associate with the track segments are used to build the muon trajectories using the KF algorithm. In the endcap muon system, the individual reconstructed component of the segments are used since the magnetic field is nonuniform [63].

These muon track information is combined and re-fitted to build a global muon track. The best global muon track is selected by a suitable χ^2 requirement for each stand-alone muon [62].

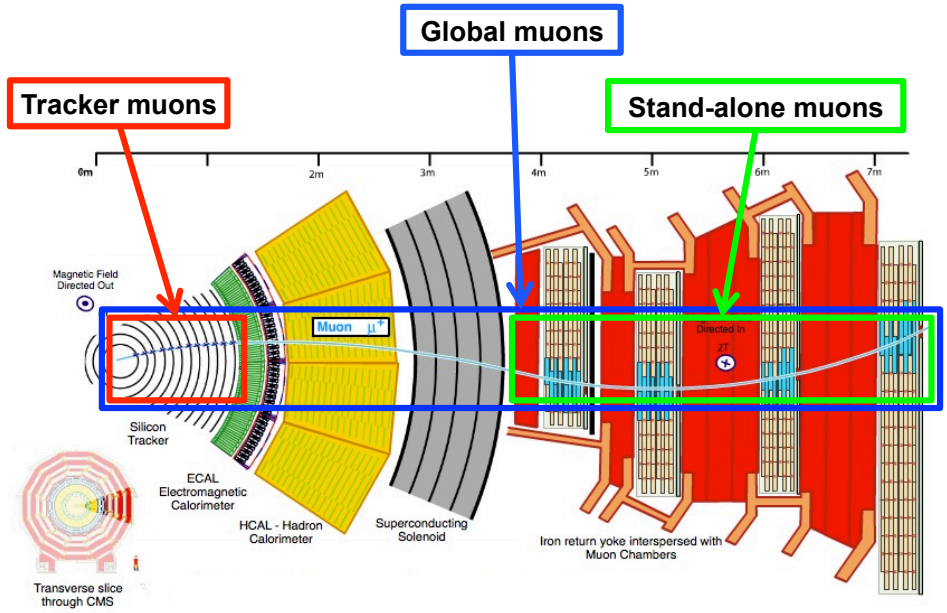

Figure 4.4: Definition of muon candidates identified by various CMS sub-detectors. Tracker muons are identified by tracker system only, stand-alone muons are identified by muons sub-detector, and global muons are obtained by matching tracker and stand-alone muon candidates using the muon reconstruction [12].

Chapter 5

Measurement of Z$\gamma\gamma$ Production Cross Section

5.1 Data and Simulated Samples

5.1.1 Data Samples for Z$\gamma\gamma$ Analysis

The cross section measurement in the electron or muon channel is done on the data collected with the CMS detector during the full 2012 run (runs 190456 - 208686) [14]. The data samples are listed in Table 5.1 and 5.2, and we restrict the analysis to the lumi-sections [64] validated in the JSON file, [1] Cert_190456-208686_8TeV_22Jan2013ReReco_Collisions12_JSON.txt [65]. The data were collected using double-muon or double-electron triggers which are listed in Table 5.3.

5.1.2 Monte Calro Simulation Samples

The Z$\gamma\gamma$ signal samples at both leading order (LO) and next-leding order (NLO) are produced privately using `MadGraph5_V_1.5.14` [66] event generator, where the Z boson can

[1] A JSON file is able to used to select events in data samples.

Run range	Dataset	$\int \mathcal{L}$, fb^{-1}
190456 - 193621	/DoubleMu/Run2012A-22Jan2013-v1/AOD	0.876
193834 - 196531	/DoubleMuParked/Run2012B-22Jan2013-v1/AOD	4.412
198022 - 203742	/DoubleMuParked/Run2012C-22Jan2013-v1/AOD	7.017
203777 - 208686	/DoubleMuParked/Run2012D-22Jan2013-v1/AOD	7.369
Total		19.674

Table 5.1: Summary of the data sample and integrated luminosity in the muon channel [14].

Run range	Dataset	$\int \mathcal{L}$, fb^{-1}
190456 - 193621	/DoubleElectron/Run2012A-22Jan2013-v1/AOD	0.876
193834 - 196531	/DoubleElectron/Run2012B-22Jan2013-v1/AOD	4.412
198022 - 203742	/DoubleElectron/Run2012C-22Jan2013-v1/AOD	7.055
203777 - 208686	/DoubleElectron/Run2012D-22Jan2013-v1/AOD	7.369
Total		19.710

Table 5.2: Summary of the data sample and integrated luminosity in the electron channel [14].

decay to a pair of any charged leptons of the same flavor. These samples have the following generator-level requirements:

- The distance between two leptons $\Delta\mathrm{R}(\ell, \ell)$ is larger than 0.4.
- The distance either leptons from photons $\Delta\mathrm{R}(\gamma, \ell)$ is larger than 0.4.
- The invariant mass of two leptons $\mathrm{M}(\ell, \ell)$ is larger than 40 GeV.
- The transverse momentum of a photon p_{T}^{γ} is larger than 10 GeV.

The LO prediction for Z$\gamma\gamma$ cross section offer the generator-level requirement is 0.125 pb. The NLO cross section for Z$\gamma\gamma$ events is 0.752 pb. The Z$\gamma\gamma$ sample was generated using the `NNPDF3.0` [67] PDF set. Resultant Les Houches Event (LHE) files were interfaced to PYHTIA6 [68] version for showering and GEANT4 [69] for simulation with "S10" pile-up scenario for 8 TeV. More detailed information on the signal generation can be found in Appendix A.1. In this Z$\gamma\gamma$ study, the NLO is used to the principal signal sample.

Dataset	Trigger Name
DoubleEle	HLT_Ele17_*_Ele8_*
DoubleMuParked	HLT_Mu17_Mu8_v* or HLT_Mu17_TkMu8_v*

Table 5.3: Summary of triggers in the muon or electron channel.

The background samples used for this analysis are officially produced and listed in Table 5.4 together with corresponding NLO cross sections.

Dataset	σ, pb
/ZGToLLG_8TeV-madgraph	159.120
/DYJetsToLL_M-50_TuneZ2Star_8TeV-madgraph-tarball	3503.71
/ZZTo4e_8TeV-powheg-pythia6	0.0769
/ZZTo4tau_8TeV-powheg-pythia6	0.0769
/ZZTo2e2mu_8TeV-powheg-pythia6	0.1767
/ZZTo2mu2tau_8TeV-powheg-pythia6	0.1767
/ZZZNoGstarJets_8TeV-madgraph	0.00459
/WWGJets_8TeV-madgraph_v2	1.440
/WWWJets_8TeV-madgraph	0.0806
/WWZNoGstarJets_8TeV-madgraph	0.0633
/WWJetsTo2L2Nu_TuneZ2star_8TeV-madgraph-tauola	5.995
/WZJetsTo2L2Q_TuneZ2star_8TeV-madgraph-tauola	5.995
/WZJetsTo3LNu_TuneZ2_8TeV-madgraph-tauola	1.057
/WZZNoGstarJets_8TeV-madgraph	0.0192
/GluGluToZZTo2L2L_TuneZ2star_8TeV-gg2zz-pythia6	0.1203
/GluGluToZZTo4L_8TeV-gg2zz-pythia6	0.0048
/TTJets_SemiLeptMGDecays_8TeV-madgraph	99.440
/TTJets_FullLeptMGDecays_8TeV-madgraph	23.830
/TTWJets_8TeV-madgraph	0.1249
/TTZJets_8TeV-madgraph_v2	0.1720
/TTGJets_8TeV-madgraph	1.4440

Table 5.4: Summary of Monte Carlo background samples and cross section used in the analysis [15].

5.1.3 Overlappig Photon Removal

Since PYTHIA6 can add extra photons to simulate V + jets events during showering, these samples partially overlap with V + γ simulated samples that have real photon emission during generation. This issue of overlapping events in V + γ and V + jets samples is resolved by vetoing these extra overlapped photon by using MC-truth information. We define a "signal" MC photon as the one produced by ISR or FSR process and that have $p_{\mathrm{T}} > 10\,\mathrm{GeV}$ and $\Delta\mathrm{R}(\ell,\gamma) > 0.4$ from the nearest lepton. If V + jets sample used for background estimation has such a signal MC photon matched to a reconstructed photon candidate within $\Delta\mathrm{R} < 0.2$ (see Figure 5.1), it is removed from consideration to avoid double counting with V + γ. In the diphoton case, the V + γ + jet sample also partially overlap with the V + γ + γ sample. If the V + γ + jet sample is produced at least two signal MC photons matched to reconstructed photon candidates within $\Delta\mathrm{R} < 0.2$, they are removed from consideration to avoid double counting with V + γ + γ.

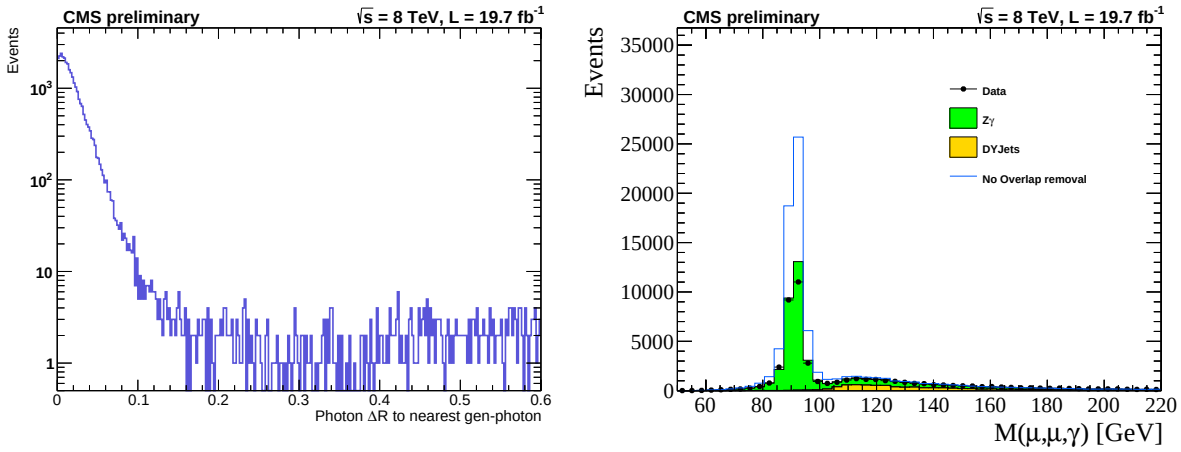

(a) (b)

Figure 5.1: The spatial separation of generator-level photon with the nearest reconstructed photon candidate in the V + jets sample. If a reconstructed candidate has $\Delta\mathrm{R} < 0.2$, we define such a candidate to be matched to the generator level photon.

5.2 Object Selection

The electron, muon, and photon candidates for the Z$\gamma\gamma$ event candidates are selected using lepton identification and photon identification that are optimized by Egamma-POGs and Muon-POGs. We also apply additional offline requirements for the event candidates.

5.2.1 Electron Selection

The electron candidates are required to pass the Egamma-POGs loose identification [70], summarized in Table 5.5. Electron candidates are required to have $p_{\mathrm{T}} > 20\,\mathrm{GeV}$ and $10\,\mathrm{GeV}$ for leading and trailing electrons, respectively. The following objects are used to identify the electron candidates [71]:

- $|\Delta\eta(sc, track)|$: The distance of supercluster to extrapolated track in η.
- $|\Delta\phi(sc, track)|$: The distance of supercluster to extrapolated track in ϕ.
- $\sigma_{i\eta i\eta}$: The shape of the energy deposit in the calorimeter that is calculated by the 5x5 ECAL crystals around the seed crystal.
- E_{had}/E_{em} : The ratio of energy measurement in HCAL over energy in ECAL.
- $|d_{xy}(vertex)|$: The transverse distance in XY plane to the primary vertex from ECAL surface.
- $|d_z(vertex)|$: The longitudinal distance in Z direction to the primary vertex from closest electron track.
- $|\frac{1}{E} - \frac{1}{p}|$: The absolute distance of the inverted supercluster energy to the inverted electron track momentum [51].
- I_{PF}/p_{T} : The isolation (I_{PF}) based on the sum of transverse momentum of PF [72] objects within $\Delta\mathrm{R} < 0.3$ around the electron [73, 74] divide by transverse momentum.

- Conversion rejection: vertex fit probability : The electron probability being matched to a conversion vertex [51].

- Conversion rejection: missing hits : The number of missing expected tracker hits on the trajectory [51].

Variable	$\lvert\eta_{SC}\rvert < 1.479$	$1.479 < \lvert\eta_{SC}\rvert < 2.5$
$\lvert\Delta\eta(sc, track)\rvert$	< 0.007	< 0.009
$\lvert\Delta\phi(sc, track)\rvert$	< 0.15	< 0.10
$\sigma_{i\eta i\eta}$	< 0.01	< 0.03
E_{had}/E_{em}	< 0.12	< 0.10
$\lvert d_{xy}(vertex)\rvert$	$< 0.02\,\text{cm}$	$< 0.02\,\text{cm}$
$\lvert d_z(vertex)\rvert$	$< 0.2\,\text{cm}$	$< 0.2\,\text{cm}$
$\lvert\frac{1}{E} - \frac{1}{p}\rvert$	$< 0.05\,\text{GeV}^{-1}$	$< 0.05\,\text{GeV}^{-1}$
I_{PF}/p_{T}	< 0.15	< 0.15 (0.10)
Conversion rejection: vertex fit probability	$< 10^{-6}$	$< 10^{-6}$
Conversion rejection: missing hits	≤ 1	≤ 1

Table 5.5: Summary of electron loose identification selection optimized by Egamma-POGs. A value in brackets is for $p_{\text{T}} < 20\,\text{GeV}$ where $\lvert\eta_{SC}\rvert$ to be between 1.479 and 2.5.

5.2.2 Muon Selection

The Muon-POGs tight identification [75] is applied in the muon selection. The all muon candidates are reconstructed as a global and tagged by particle flow. All the muon identification and isolation requirements is summarized in Table 5.6. Events are required to have at least two muon candidates passing identification and isolation with the $p_{\text{T}} > 20\,\text{GeV}$ and 10 GeV, respectively. The following objects are used to identify the muon candidates [75]:

- $\chi^2/ndof$ of global fit : The normalized χ^2 of the global muon track.

- muon system hits in global fit : The number of valid muon hits on the track.

- matched muon stations : The number of muon stations with matched segment.

- $|d_{xy}|$: The transverse impact parameter of the tracker track from the primary vertex.
- $|d_z|$: The longitudinal impact parameter of the tracker track from the primary vertex.
- pixel hits : The number of hits in the pixel detector.
- tracker layers with measurement : The number of tracker layers with a valid measurement.
- I_{PF}/p_{T} : The PF-based isolation (I_{PF}) based on the charged hadron from pile-up to infer the total amount of pile-up energy from neutrals with a cone size of $\Delta\mathrm{R} < 0.4$ [76].

Variable	$\lvert\eta\rvert < 2.4$
$\chi^2/ndof$ of global fit	< 10
muon system hits in global fit	> 0
matched muon stations	> 1
$\lvert d_{xy}\rvert$	$< 0.2\,\mathrm{cm}$
$\lvert d_z\rvert$	$< 0.5\,\mathrm{cm}$
pixel hits	> 0
tracker layers with measurement	> 5
I_{PF}/p_{T}	< 0.12

Table 5.6: Summary of muon tight identification and isolation selection optimized by Muon-POGs.

5.2.3 Photon Pre-selection

Photon candidates are selected in the barrel (EB), $|\eta_{SC}| < 1.479$, and endcap (EE), $1.479 < |\eta_{SC}| < 2.5$, sections of the CMS electromagnetic calorimeter (ECAL) excluding the EB/EE gap-region $1.44 < |\eta_{SC}| < 1.57$ passing the Egamma-POGs medium photon identification [77], except for the PF charged hadron isolation, summarized in Table 5.8. Photon candidates are required to have $p_{\mathrm{T}}^{\gamma} > 15\,\mathrm{GeV}$. The following objects are used to identi-

fied pre-selected photon candidates [78], and distributions of these objects are shown in Figure 5.2.

- Single-tower H/E : The ratio of the sum of the hadronic energies within a cone of size $\Delta\mathrm{R} < 0.15$ over the supercluster energy.

- Conversion safe electron veto : Remove the photon candidate if its supercluster is matched to an electron candidate to avoid misidentify electron as photon [79].

- $\sigma_{i\eta i\eta}$: The shower shape objects is defined as Equation [80]:

$$\sigma^2_{i\eta i\eta} = \frac{\sum_i^{5x5} \omega_i (i\eta_i - i\eta_{seed})^2}{\sum_i^{5x5} \omega_i} \quad ; \quad \omega_i = \max\left(0.,\ 4.7 + \ln\left(\frac{E_i}{E_{5x5}}\right)\right) \tag{5.1}$$

  Lowercase where $i\eta_{\text{seed}}$ is the energy of the seed crystal, E_{5x5} is the energy of the 5x5 crystals around the seed crystal, and E_i and $i\eta$ are the energy and η of the i-th crystal within the 5x5 ECAL cluster, respectively.

- Rho corrected PF isolation : The isolation, based on the PF objects, is corrected for pile-up using Rho: $I_{\text{corr}} = max(I - Rho \times A_{\text{eff}}, 0)$ where A_{eff} is the effective area determined to stabilize the efficiency with respect to changing pile-up conditions. The effective areas used for PF isolations for charged hadrons, neutral hadrons, and photons in this analysis are summarized in Table 5.7. The isolation of photons is built with a cone size of $\Delta\mathrm{R} < 0.3$.

$\|\eta\|$ range	Charged Hadrons	Neutral Hadrons	Photons
$0.0 < \|\eta\| < 1.0$	0.012	0.030	0.148
$1.0 < \|\eta\| < 1.479$	0.010	0.057	0.130
$1.479 < \|\eta\| < 2.0$	0.014	0.039	0.112
$2.0 < \|\eta\| < 2.2$	0.012	0.015	0.216
$2.2 < \|\eta\| < 2.3$	0.016	0.024	0.262
$2.3 < \|\eta\| < 2.4$	0.020	0.039	0.260
$\|\eta\| > 2.4$	0.012	0.072	0.266

Table 5.7: The effective areas used for PF isolations [16].

Variable	$\|\eta_{SC}\| < 1.479$	$1.479 < \|\eta_{SC}\| < 2.5$
Single-tower H/E	< 0.05	< 0.05
Conversion safe electron veto	$\surd$	$\surd$
$\sigma_{i\eta i\eta}$	< 0.011	< 0.033
Rho corrected PF neutral hadron isolation	$< 1.0 + 0.04\,p_{\mathrm{T}}$	$< 1.5 + 0.04\,p_{\mathrm{T}}$
Rho corrected PF photon isolation	$< 0.7 + 0.005\,p_{\mathrm{T}}$	$< 1.0 + 0.005\,p_{\mathrm{T}}$

Table 5.8: Summary of photon pre-selected identification selection optimized by Egamma-POGs.

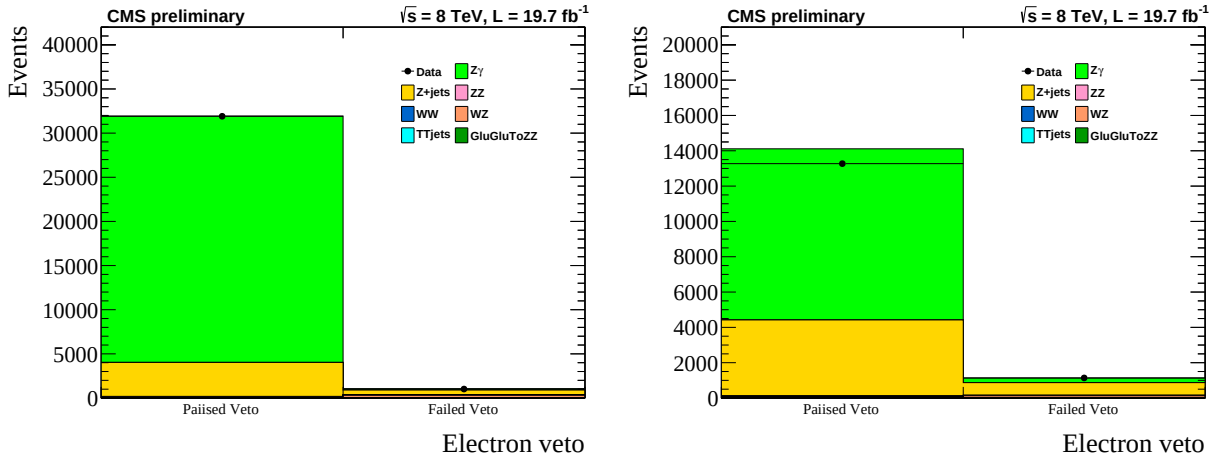

(a) (b)

Figure 5.2: Distribution of photon requirement variables. Electron veto (a, b), Single-tower H/E (c, d), $\sigma_{i\eta i\eta}$ (e, f), PF Neutral Hadron Isolation (g, h),and PF Photon Isolation (i, j) in EB (left) and EE (right) region in $\mathrm{Z}\gamma \to \mu\mu\gamma$ events.

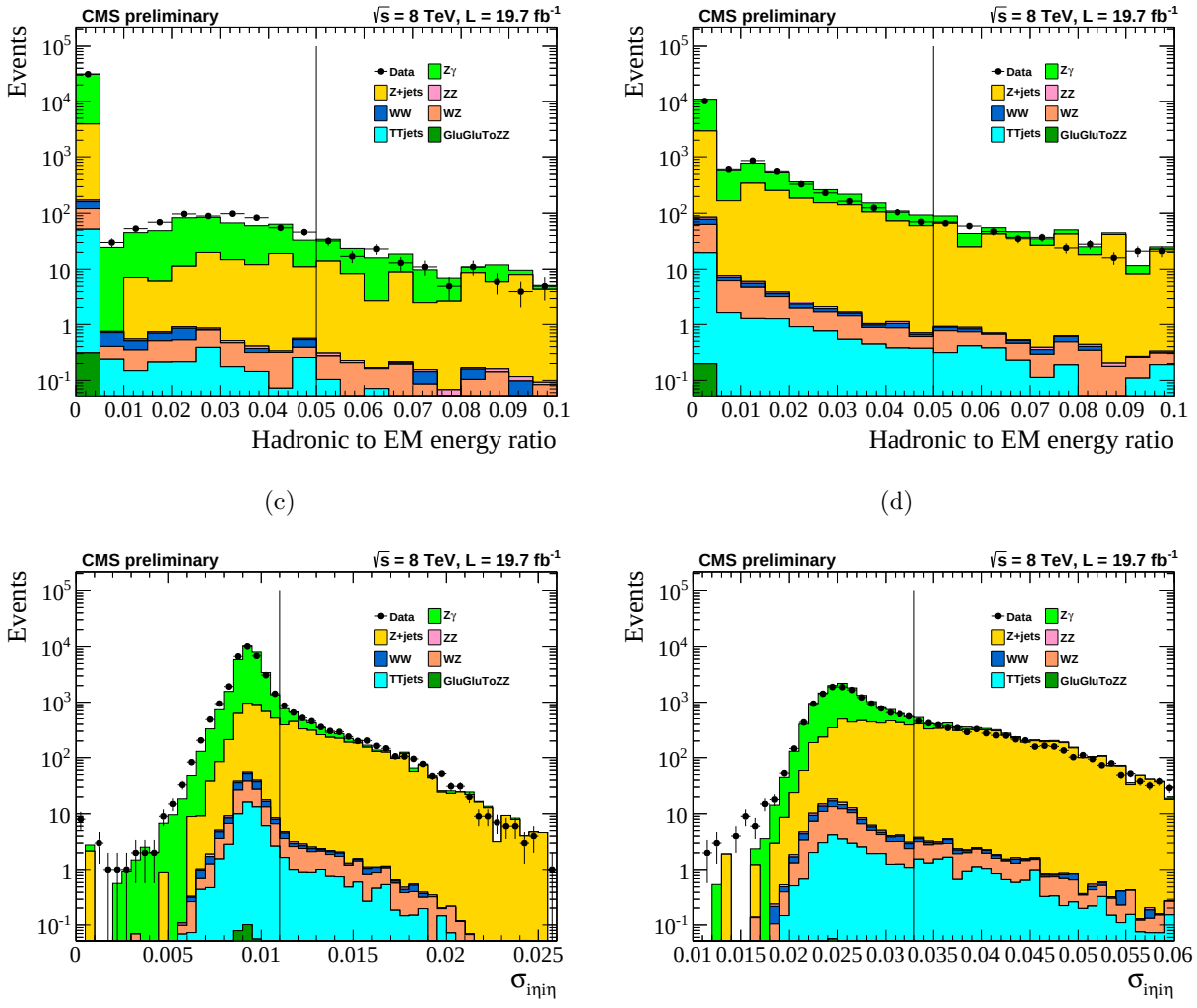

Figure 5.2: Distribution of photon requirement variables. Electron veto (a, b), Single-tower H/E (c, d), $\sigma_{i\eta i\eta}$ (e, f), PF Neutral Hadron Isolation (g, h),and PF Photon Isolation (i, j) in EB (left) and EE (right) region in $Z\gamma \to \mu\mu\gamma$ events.

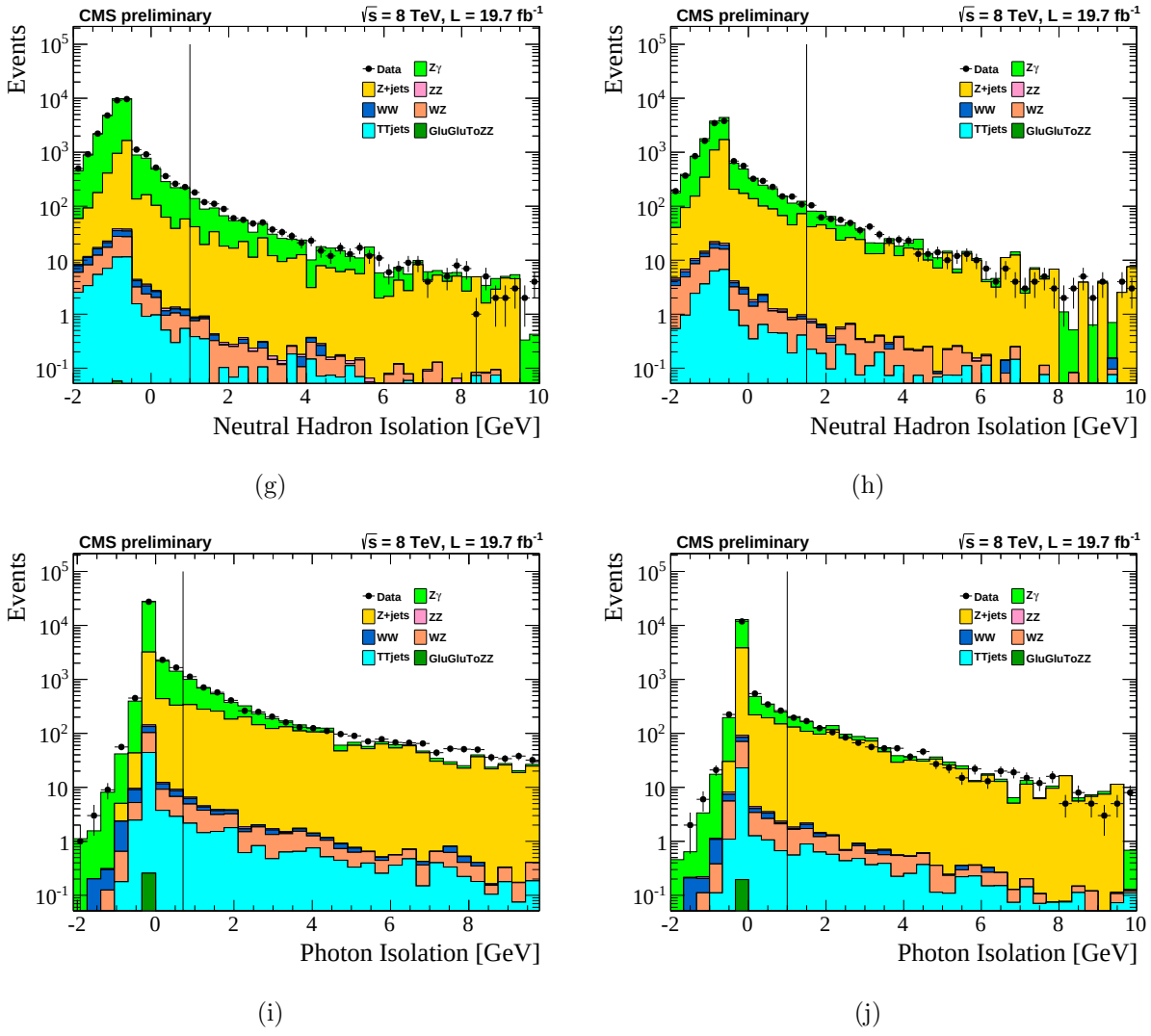

Figure 5.2: Distribution of photon requirement variables. Electron veto (a, b), Single-tower H/E (c, d), $\sigma_{i\eta i\eta}$ (e, f), PF Neutral Hadron Isolation (g, h),and PF Photon Isolation (i, j) in EB (left) and EE (right) region in $Z\gamma \to \mu\mu\gamma$ events.

5.2.4 Photon Selection

Signal photon candidates require to pass charged hadron isolation requirements in EB (EE) region [77, 78]:

- Rho corrected PF charged hadron isolation < 1.5 (1.2) GeV

The isolation of photons is defined with $\Delta R < 0.3$ similarly to the PF neutral hadron isolation and PF photon isolation. Figure 5.3 shows the distribution of PF charged hadron isolation.

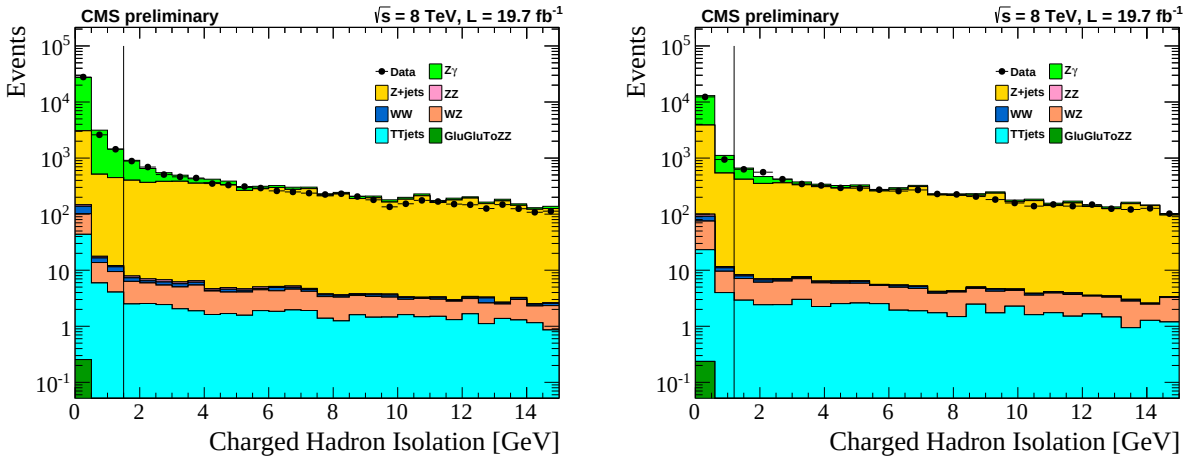

(a) (b)

Figure 5.3: PF charged hadron isolation in EB (a) and EE (b) region for $Z\gamma \to \mu\mu\gamma$ events.

5.2.5 Event Selection

The events for the analysis require to have double-electron or double-muon triggers (see Table 5.3 in Section 5.1.1). These triggers require the minimum transverse momentum of electron or muon candidates to be 17 GeV and 8 GeV. In addition, we require to have two electron or two muon candidates passing identification and isolation, and at least two photons passing pre-selection that are separated from either leptons, $\Delta R(\gamma, \ell) > 0.4$, and two photons are separated from each other, $\Delta R(\gamma, \gamma) > 0.4$. Additional offline requirements

are applied when electron/muon and photon candidates pass the selections described above. In both electron and muon channel, invariant mass of two leptons candidates is required to be greater than 40 GeV.

5.3 Monte Carlo Correction Factors

All MC simulation samples are weighted such that their pile-up distributions match those measured in the data. Additional scale factors (SFs) are applied to the simulation performance to match to the data that are measured by the ratio between data and MC simulations. The SFs are calculated as function of η and p_{T} of objects (leptons or photon).

5.3.1 Pile-Up Multiplicity Correction

The application of pile-up reweighting essentially improve the agreement between the data and the MC simulations. Figure 5.4 shows the number of primary vertices before and after MC samples are applied pile-up reweighting. All MC samples are done with the application of the pile-up reweighting in this analysis.

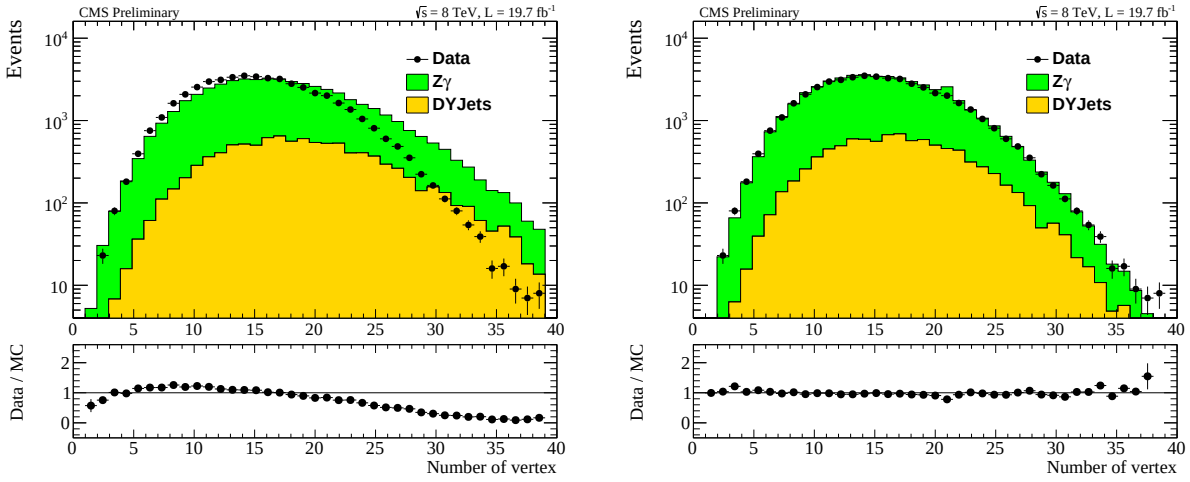

(a) (b)

Figure 5.4: The number of primary vertices in data and MC simulation before (a) and after (b) applied pile-up reweighting to selection of $\mathrm{Z}\gamma \to \mu\mu\gamma$ events.

5.3.2 Electron Efficiency Scale Factors

The electron trigger and reconstruction SFs are measured by the Egamma-POGs. The electron efficiencies are determined by a tag and probe method using Z decays [81]. Table 5.9 and 5.10 show the scale factor representing the trigger and identification, respectively. The efficiencies are scaled up and down by their uncertainties that are used to measure the systematic uncertainty.

	$0.0 < \lvert\eta^{e1}_{SC}\rvert < 1.47$	$1.47 < \lvert\eta^{e1}_{SC}\rvert < 2.4$
$0.0 < \lvert\eta^{e2}_{SC}\rvert < 1.47$	$0.996^{+0.011}_{-0.011}$	$1.008^{+0.016}_{-0.016}$
$1.47 < \lvert\eta^{e2}_{SC}\rvert < 2.4$	$0.994^{+0.017}_{-0.017}$	$0.966^{+0.025}_{-0.025}$

Table 5.9: Electron trigger SFs as a function of $|\eta_{SC}|$ for leading electron and trailing electron that are provided by Egamma-POGs. The uncertainty include statistical and systematical uncertainties.

p_{T} GeV	$0.0 < \lvert\eta_{SC}\rvert < 0.8$	$0.8 < \lvert\eta_{SC}\rvert < 1.442$	$1.442 < \lvert\eta_{SC}\rvert < 1.556$	$1.556 < \lvert\eta_{SC}\rvert < 2.0$	$2.0 < \lvert\eta_{SC}\rvert < 2.5$
10 - 15	$0.865^{+0.023}_{-0.019}$	$0.967^{+0.020}_{-0.020}$	$1.064^{+0.103}_{-0.092}$	$0.939^{+0.039}_{-0.038}$	$1.050^{+0.019}_{-0.019}$
15 - 20	$0.958^{+0.009}_{-0.009}$	$0.971^{+0.010}_{-0.010}$	$0.902^{+0.036}_{-0.032}$	$0.897^{+0.016}_{-0.016}$	$0.941^{+0.017}_{-0.017}$
20 - 30	$0.988^{+0.002}_{-0.002}$	$0.965^{+0.003}_{-0.003}$	$0.990^{+0.011}_{-0.011}$	$0.953^{+0.005}_{-0.005}$	$1.017^{+0.005}_{-0.005}$
30 - 40	$1.002^{+0.001}_{-0.001}$	$0.985^{+0.001}_{-0.001}$	$0.966^{+0.005}_{-0.005}$	$0.980^{+0.003}_{-0.003}$	$1.019^{+0.003}_{-0.003}$
40 - 50	$1.005^{+0.001}_{-0.001}$	$0.989^{+0.001}_{-0.001}$	$0.971^{+0.004}_{-0.004}$	$0.999^{+0.002}_{-0.002}$	$1.019^{+0.002}_{-0.002}$
50 <	$1.005^{+0.001}_{-0.001}$	$0.989^{+0.002}_{-0.002}$	$0.980^{+0.008}_{-0.008}$	$1.004^{+0.003}_{-0.002}$	$1.023^{+0.004}_{-0.004}$

Table 5.10: Electron identification SFs as a function of $|\eta_{SC}|$ and p_{T} that are provided by Egamma-POGs. The uncertainty include statistical and systematical uncertainties.

5.3.3 Muon Efficiency Scale Factors

The muon trigger and reconstruction SFs are measured by the Muon-POGs. The muon efficiencies are determined by a tag and probe method using Z decays [82]. Table 5.11 shows the scale factor for muon trigger, Table 5.12 shows the scale factor for muon identification, and the muon isolation scale factor is shown in Table 5.13. The efficiencies are scaled up and down by their uncertainties that are used to measure the systematic uncertainty.

	$0.0 < \|\eta^{\mu 1}\| < 0.9$	$0.9 < \|\eta^{\mu 1}\| < 1.2$	$1.2 < \|\eta^{\mu 1}\| < 2.1$	$2.1 < \|\eta^{\mu 1}\| < 2.4$
$0.0 < \|\eta^{\mu 2}\| < 0.9$	$0.964^{+0.001}_{-0.001}$	$0.968^{+0.011}_{-0.011}$	$0.960^{+0.010}_{-0.010}$	$0.976^{+0.023}_{-0.023}$
$0.9 < \|\eta^{\mu 2}\| < 1.2$	$0.971^{+0.011}_{-0.011}$	$0.971^{+0.012}_{-0.012}$	$0.964^{+0.012}_{-0.012}$	$0.962^{+0.024}_{-0.024}$
$1.2 < \|\eta^{\mu 2}\| < 2.1$	$0.970^{+0.010}_{-0.010}$	$0.962^{+0.012}_{-0.012}$	$0.953^{+0.011}_{-0.011}$	$0.966^{+0.020}_{-0.020}$
$2.1 < \|\eta^{\mu 2}\| < 2.4$	$0.967^{+0.021}_{-0.021}$	$0.951^{+0.026}_{-0.026}$	$0.936^{+0.017}_{-0.017}$	$1.037^{+0.065}_{-0.065}$

Table 5.11: Muon trigger SFs as a function of $|\eta|$ for leading muon and trailing muon that are provided by Muon-POGs. The uncertainty include statistical and systematical uncertainties.

p_{T} GeV	$0.0 < \|\eta\| < 0.9$	$0.9 < \|\eta\| < 1.2$	$1.2 < \|\eta\| < 2.1$	$2.1 < \|\eta\| < 2.4$
10 - 20	$0.970^{+0.005}_{-0.005}$	$1.002^{+0.007}_{-0.007}$	$1.018^{+0.004}_{-0.004}$	$1.005^{+0.007}_{-0.007}$
20 - 25	$0.989^{+0.002}_{-0.002}$	$0.994^{+0.003}_{-0.002}$	$1.000^{+0.001}_{-0.001}$	$0.998^{+0.003}_{-0.003}$
25 - 30	$0.992^{+0.001}_{-0.001}$	$0.995^{+0.001}_{-0.001}$	$0.998^{+0.001}_{-0.001}$	$0.996^{+0.002}_{-0.002}$
30 - 35	$0.993^{+0.001}_{-0.001}$	$0.993^{+0.001}_{-0.001}$	$0.997^{+0.001}_{-0.001}$	$1.001^{+0.002}_{-0.002}$
35 - 40	$0.994^{+0.000}_{-0.000}$	$0.992^{+0.001}_{-0.001}$	$0.996^{+0.001}_{-0.001}$	$0.993^{+0.001}_{-0.001}$
40 - 50	$0.992^{+0.000}_{-0.000}$	$0.992^{+0.000}_{-0.000}$	$0.996^{+0.000}_{-0.000}$	$0.995^{+0.001}_{-0.001}$
50 - 60	$0.991^{+0.001}_{-0.001}$	$0.995^{+0.001}_{-0.001}$	$0.995^{+0.001}_{-0.001}$	$0.994^{+0.003}_{-0.003}$
60 - 90	$0.989^{+0.001}_{-0.001}$	$0.990^{+0.002}_{-0.002}$	$0.992^{+0.002}_{-0.002}$	$0.989^{+0.005}_{-0.005}$
90 - 140	$1.004^{+0.003}_{-0.003}$	$1.009^{+0.006}_{-0.006}$	$1.023^{+0.005}_{-0.005}$	$1.060^{+0.010}_{-0.016}$
140 <	$1.019^{+0.017}_{-0.017}$	$1.011^{+0.035}_{-0.032}$	$0.975^{+0.029}_{-0.030}$	$0.891^{+0.124}_{-0.160}$

Table 5.12: Muon identification SFs as a function of $|\eta|$ and p_{T} given by Muon-POGs. The uncertainty include statistical and systematical uncertainties.

p_{T} GeV	$0.0 < \|\eta\| < 0.9$	$0.9 < \|\eta\| < 1.2$	$1.2 < \|\eta\| < 2.1$	$2.1 < \|\eta\| < 2.4$
10 - 20	$0.959^{+0.003}_{-0.003}$	$0.966^{+0.003}_{-0.003}$	$0.982^{+0.002}_{-0.002}$	$1.076^{+0.004}_{-0.004}$
20 - 25	$0.988^{+0.001}_{-0.001}$	$0.990^{+0.002}_{-0.002}$	$0.995^{+0.001}_{-0.001}$	$1.060^{+0.003}_{-0.003}$
25 - 30	$0.999^{+0.001}_{-0.001}$	$1.002^{+0.001}_{-0.001}$	$1.002^{+0.001}_{-0.001}$	$1.047^{+0.002}_{-0.002}$
30 - 35	$0.999^{+0.000}_{-0.000}$	$1.002^{+0.001}_{-0.001}$	$1.003^{+0.000}_{-0.000}$	$1.032^{+0.001}_{-0.001}$
35 - 40	$0.999^{+0.000}_{-0.000}$	$1.001^{+0.001}_{-0.001}$	$1.002^{+0.000}_{-0.000}$	$1.023^{+0.001}_{-0.001}$
40 - 50	$0.998^{+0.000}_{-0.000}$	$1.000^{+0.000}_{-0.000}$	$1.000^{+0.000}_{-0.000}$	$1.011^{+0.000}_{-0.000}$
50 - 60	$0.999^{+0.000}_{-0.000}$	$1.000^{+0.000}_{-0.000}$	$1.000^{+0.000}_{-0.000}$	$1.000^{+0.001}_{-0.001}$
60 - 90	$1.000^{+0.000}_{-0.000}$	$1.000^{+0.000}_{-0.000}$	$1.000^{+0.000}_{-0.000}$	$1.007^{+0.001}_{-0.001}$
90 - 140	$1.001^{+0.001}_{-0.001}$	$1.001^{+0.001}_{-0.001}$	$1.000^{+0.001}_{-0.001}$	$0.999^{+0.003}_{-0.003}$
140 <	$1.001^{+0.002}_{-0.002}$	$1.004^{+0.005}_{-0.003}$	$0.997^{+0.002}_{-0.001}$	$1.005^{+0.010}_{-0.015}$

Table 5.13: Muon isolation SFs as a function of $|\eta|$ and p_{T} given by Muon-POGs. The uncertainty include statistical and systematical uncertainties.

5.3.4 Photon Efficiency Scale Factors

The SFs for photon identification are provided by the Egamma-POGs. The photon efficiencies are determined in a similar way to electrons, a tag and probe method using Z decays [83]. Table 5.14 shows the photon scale factor. The efficiencies are scaled up and down by their uncertainties that are used to measure the systematic uncertainty.

p_{T} GeV	$0.0 < \lvert\eta_{SC}\rvert < 0.8$	$0.8 < \lvert\eta_{SC}\rvert < 1.44$	$1.57 < \lvert\eta_{SC}\rvert < 2.0$	$2.0 < \lvert\eta_{SC}\rvert < 2.5$
15 - 20	$0.946^{+0.021}_{-0.021}$	$0.992^{+0.021}_{-0.021}$	$1.001^{+0.021}_{-0.021}$	$1.017^{+0.021}_{-0.021}$
20 - 30	$0.964^{+0.010}_{-0.010}$	$0.973^{+0.010}_{-0.010}$	$0.984^{+0.010}_{-0.010}$	$1.005^{+0.010}_{-0.010}$
30 - 40	$0.976^{+0.010}_{-0.010}$	$0.978^{+0.010}_{-0.010}$	$0.992^{+0.010}_{-0.010}$	$1.004^{+0.010}_{-0.010}$
40 - 50	$0.980^{+0.010}_{-0.010}$	$0.984^{+0.010}_{-0.010}$	$0.996^{+0.010}_{-0.010}$	$1.007^{+0.010}_{-0.010}$
50 <	$0.979^{+0.010}_{-0.010}$	$0.982^{+0.010}_{-0.010}$	$0.997^{+0.010}_{-0.010}$	$1.008^{+0.010}_{-0.010}$

Table 5.14: Photon identification SFs as a function of $|\eta_{SC}|$ and p_{T} given by Egamma-POGs. The uncertainty include statistical and systematical uncertainties.

5.4 Background Estimation using Matrix Method

The dominant background to the Z$\gamma\gamma$ process is from Zγ + jets and Z + jets production, where one or two of the jets are misidentified as photon candidates. Signal events can be classified in four cases: true signal events, where both photon candidates are true signal photons ($\gamma\,\gamma$), events with a leading or trailing photon candidate being a misidentified jet that we refer to as ($\gamma\,$j) and (j$\,\gamma$) respectively, and finally events with both photon candidates being misidentified jets (j j) (see Figure 5.5).

The contribution from backgrounds is established using control data samples. This backgrounds can be estimated in data by measuring the number of the events that pass or fail requirements on sensitive observable. In this study, we chose PF charged hadron isolation, but the method should work with any observable that can separate signal from background well. The method to estimate backgrounds for PF charged hadron isolation is described in Section 5.4.1 through 5.4.3.

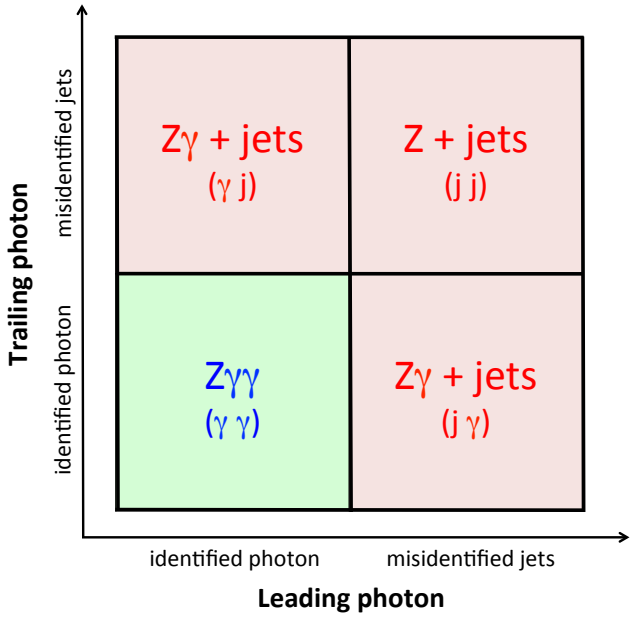

Figure 5.5: A signal process when both photon candidates are identified true photons (green), and three background processes (red) where either of the two is misidentified jets or both of them are misidentified jets.

5.4.1 PF Charged Hadron Isolation

The PF charged hadron isolation of photons, described in Section 5.2.3, can separate signal and background well. Figure 5.6 shows the PF charged hadron isolation distribution based on simulated events. The distribution of both blue and red are "identified" photons. Blue is true, and red is false. True photons peak sharply in PF charged hadron isolation, while misidentified jets have much wider distribution with long tails. Thus, PF charged hadron isolation is required to be less than 1.5 in EB and 1.2 in EE region in order to remove PF charged hadron isolation long tail that is dominated by the misidentified jets.

In the following, we define four non-overlapping regions based on PF charged hadron isolation as follows: both photons pass the observable requirement (PP), the leading photon passes but the trailing photon fails (PF), the trailing photon passes but the leading photon fails (FP), and both of them fail (FF). The observable for the true photons and for the

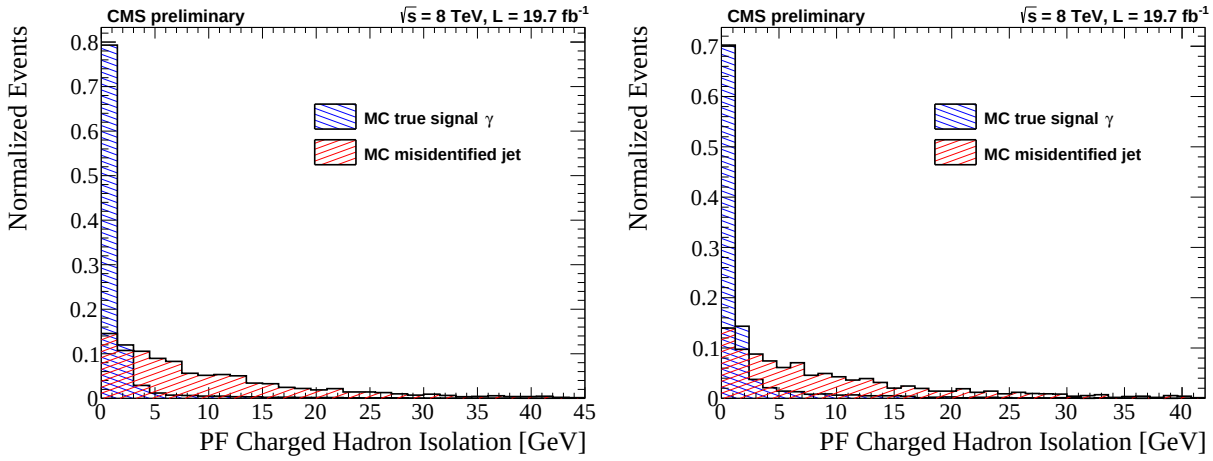

(a) (b)

Figure 5.6: The comparison of PF charged hadron isolation distribution between true signal photon (blue) and misidentified jet (red) for MC simulation in EB (a) and EE (b) region.

misidentified jets are taken to calculate probabilities of those four regions.

To measure the probabilities for genuine photons to pass or fail the observable requirements, we use simulated $Z\gamma \rightarrow \mu\mu\gamma$ events where reconstructed photons are required to matched to a true photon within $\Delta R < 0.2$. The probabilities are measured separately for photons in EB and EE region within each leading photon bin ($15 < p_T < 25$, $25 < p_T < 40$, $p_T > 40\,GeV$). The distribution of true matched photons is compared with data for FSR Z $\rightarrow \ell\ell\gamma$ process, where $\ell\ell$ will be a pair of muons (see Figure 5.7). We select these events following the standard criteria, except for the requirement on PF charged hadron isolation. Moreover, we require the three-body invariant mass of $\mu\mu\gamma$ to be within 5 GeV of the Z mass, 91.2 GeV [80, 84]. This selection yields nearly 100% pure $Z \rightarrow \mu\mu\gamma$ production. Probabilities of simulated $Z\gamma$ and true signal photon candidates for data events as summarized in Table 5.15. Systematic uncertainty on the measured probabilities for genuine photons is determined by comparing the distribution of charged hadron isolation between simulation and data.

The observable of jets misidentified as photons is determined from Z + jets data. For obtaining misidentified jets, events have to have two reconstructed muon candidates and one

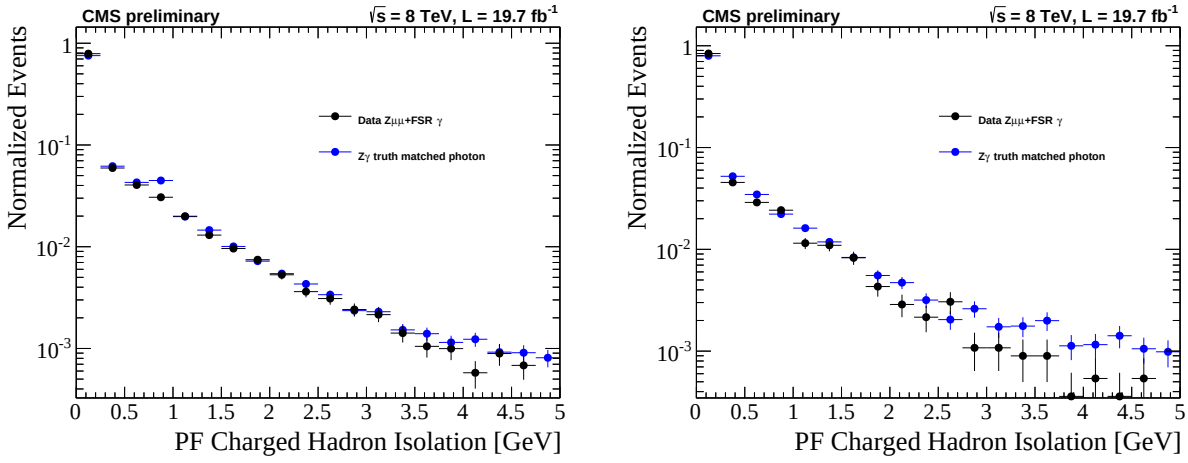

(a) (b)

Figure 5.7: The comparison of the shape of PF charged hadron isolation distribution between true matched photon in simulated Zγ (blue) events and FSR photon candidate in Z $\rightarrow \mu\mu$ events in data (black) in EB (a) and EE (b) region.

	MC simulated Zγ		Data for FSR Z $\rightarrow \mu\mu\gamma$	
$\lvert\eta\rvert$	ϵ_γ^P	ϵ_γ^F	ϵ_γ^P	ϵ_γ^F
EB	0.950±0.002	0.050±0.002	0.952±0.002	0.048±0.002
EE	0.941±0.003	0.059±0.003	0.946±0.004	0.054±0.004

Table 5.15: Probabilities of identified true photon candidates for charged hadron isolation in EB and EE region.

photon candidate passing pre-selections described in Section 5.2.3. The invariant mass of two muon candidates has to be within 5 GeV of the Z mass, 91.2 GeV, and misidentified jet candidates have to be separated from any charged lepton candidates with $\Delta R\ (\gamma, \ell) > 1.0$ to reduce the contribution from FSR photon candidates. Figure 5.8 shows the comparison of PF charged hadron isolation distribution between data and simulation for Z + jets events. The study of Zγ production in 8 TeV data had given an excellent agreement [80], we use MC simulation to subtract remaining true photon contribution from the FSR Z processes. Similarly to the probabilities for genuine photons, the probabilities of misidentified jets are determined separately for photons in EB and EE region and in each leading photon p_T bin ($15 < p_T < 25$, $25 < p_T < 40$, $p_T > 40$ GeV). Probabilities of misidentified jets as summarized in Table 5.16.

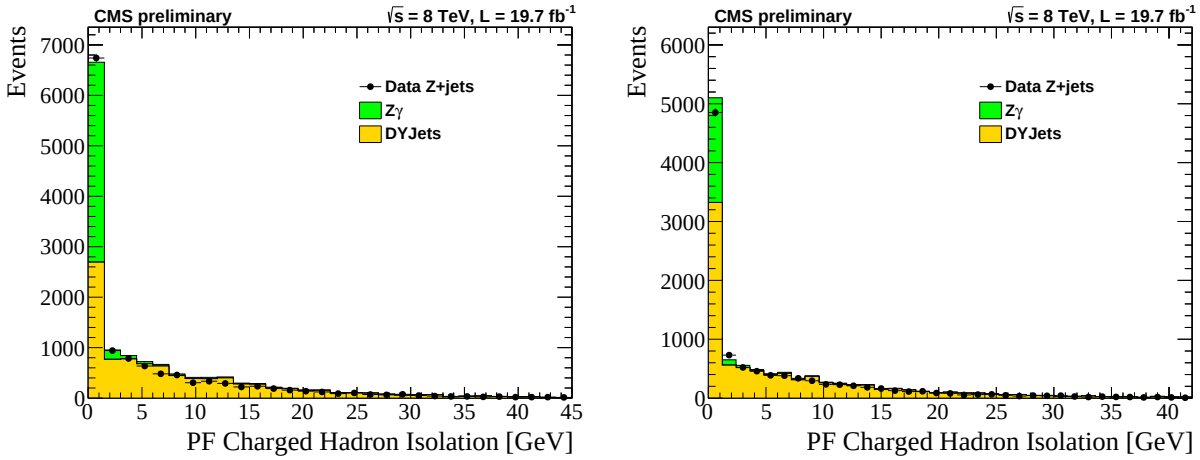

(a) (b)

Figure 5.8: The comparison of PF charged hadron isolation distribution between data and simulation for Z + jets using the $\mu\mu$ final state in EB (a) and EE (b) region.

5.4.2 Matrix Method to Background Estimate

In this Z$\gamma\gamma$ analysis, we employs "Matrix Method" to subtract backgrounds. The idea of this method is to use the observed classified data events to estimate the background

	Z + jets data	
$\|\eta\|$	ϵ_j^P	ϵ_j^F
EB	0.409±0.007	0.591±0.007
EE	0.485±0.007	0.515±0.007

Table 5.16: Probabilities of misidentified jets for charged hadron isolation in EB and EE region.

contributions through an probability matrix. The number of events in the four above-mentioned categories ($\alpha_{\gamma\gamma}$, $\alpha_{\gamma j}$, $\alpha_{j\gamma}$, α_{jj}) in the signal sample that passes pre-selection identification can be connected with the number of the observed events after applying full selection criteria (N_{PP}, N_{PF}, N_{FP}, N_{FF}) as Equation 5.2. The background study process is done separately for the case when two photon candidates in EB region (EB-EB), and one of the photon candidate in EB and an another candidate is in EE region (EB-EE and EE-EB).

$$\begin{pmatrix} N_{PP} \\ N_{PF} \\ N_{FP} \\ N_{FF} \end{pmatrix} = \begin{pmatrix} \epsilon_\gamma^P \epsilon_\gamma^P & \epsilon_\gamma^P \epsilon_j^P & \epsilon_j^P \epsilon_\gamma^P & \epsilon_{jj}^{PP} \\ \epsilon_\gamma^P \epsilon_\gamma^F & \epsilon_\gamma^P \epsilon_j^F & \epsilon_j^P \epsilon_\gamma^F & \epsilon_{jj}^{PF} \\ \epsilon_\gamma^F \epsilon_\gamma^P & \epsilon_\gamma^F \epsilon_j^P & \epsilon_j^F \epsilon_\gamma^P & \epsilon_{jj}^{FP} \\ \epsilon_\gamma^F \epsilon_\gamma^F & \epsilon_\gamma^F \epsilon_j^F & \epsilon_j^F \epsilon_\gamma^F & \epsilon_{jj}^{FF} \end{pmatrix} \begin{pmatrix} \alpha_{\gamma\gamma} \\ \alpha_{\gamma j} \\ \alpha_{j\gamma} \\ \alpha_{jj} \end{pmatrix} \tag{5.2}$$

The observed events where the both photon candidates pass PF charged hadron isolation requirement are denotes N_{PP} that consists of two photon candidates events corresponding to true signal events ($\gamma\,\gamma$) and background events ($\gamma\,\mathrm{j}$, $\mathrm{j}\,\gamma$, and $\mathrm{j}\,\mathrm{j}$) processes. From tested on the MC simulation, we assume that probabilities for a true photon and misidentified jets to be uncorrelated. However, for the case when both photon candidates are being misidentified jets ($\mathrm{j}\,\mathrm{j}$), small correlations between one and the other photon objects are exist in data. To include those correlation effects to the measurements, we use data events that have two misidentified jets. To enhance the misidentified jets, both pre-selected photon candidates

are fallen in "sideband" region. Table 5.17 summarizes sideband definition in EB and EE regions. The probabilities of two misidentified jets are determined by two-dimensional PF charged hadron isolation distribution in each leading photon p_{T} bin in each η region (EB-EB, EB-EE, EE-EB). Systematic uncertainty is measured based on selections of sideband that is described in Section 5.6. Figure 5.9 shows two-dimensional PF charged hadron isolation distribution of misidentified jets. Probabilities of events with both photon candidates being misidentified jets (j j) in four non-overlapping regions (PP, PF, FP, FF) for data events as summarized in Table 5.18.

Selection	Sideband definition
Nominal	$0.011\,(0.033) < \sigma_{i\eta i\eta} < 0.029\,(0.087)$, $0.7\,(1.0) <$ PF Pho. Iso. $< 9.0\,(9.0)$
Tight	$0.011\,(0.033) < \sigma_{i\eta i\eta} < 0.029\,(0.087)$, $0.7\,(1.0) <$ PF Pho. Iso. $< 7.0\,(7.0)$
Loose	$0.011\,(0.033) < \sigma_{i\eta i\eta} < 0.029\,(0.087)$, $0.7\,(1.0) <$ PF Pho. Iso. $< 11.0\,(11.0)$
Looser	$0.011\,(0.033) < \sigma_{i\eta i\eta} < 0.029\,(0.087)$, $0.7\,(1.0) <$ PF Pho. Iso. $< 16.0\,(16.0)$

Table 5.17: The sideband definition to define misidentified jets. The numbers are in brackets in EE region.

η	ϵ_{jj}^{PP}	ϵ_{jj}^{PF}	ϵ_{jj}^{FP}	ϵ_{jj}^{FF}
EB-EB	0.084±0.013	0.047±0.010	0.156±0.016	0.713±0.020
EB-EE	0.088±0.017	0.071±0.015	0.170±0.022	0.671±0.028
EE-EB	0.123±0.021	0.059±0.015	0.182±0.025	0.636±0.031

Table 5.18: Probabilities when both photon candidates are misidentified jets (j j) for PF charged hadron isolation when both photon candidates in EB region, and the one when one of the photon candidate in EB and EE region.

The probability matrix is evaluated with the probability terms (ϵ_{γ}^{P}, ϵ_{γ}^{F}, ϵ_{j}^{P}, ϵ_{j}^{F}, ϵ_{jj}^{PP}, ϵ_{jj}^{PF}, ϵ_{jj}^{FP}, ϵ_{jj}^{FF}). Thus, by solving the matrix equation, the number of events are evaluated for each of two photons samples so that the contamination of the background in the PP ($\epsilon_{\gamma}^{P}\,\epsilon_{j}^{P}\alpha_{\gamma\,j}$ + $\epsilon_{j}^{P}\,\epsilon_{\gamma}^{P}\alpha_{j\,\gamma}$ + $\epsilon_{jj}^{PP}\alpha_{j\,j}$) can be estimated.

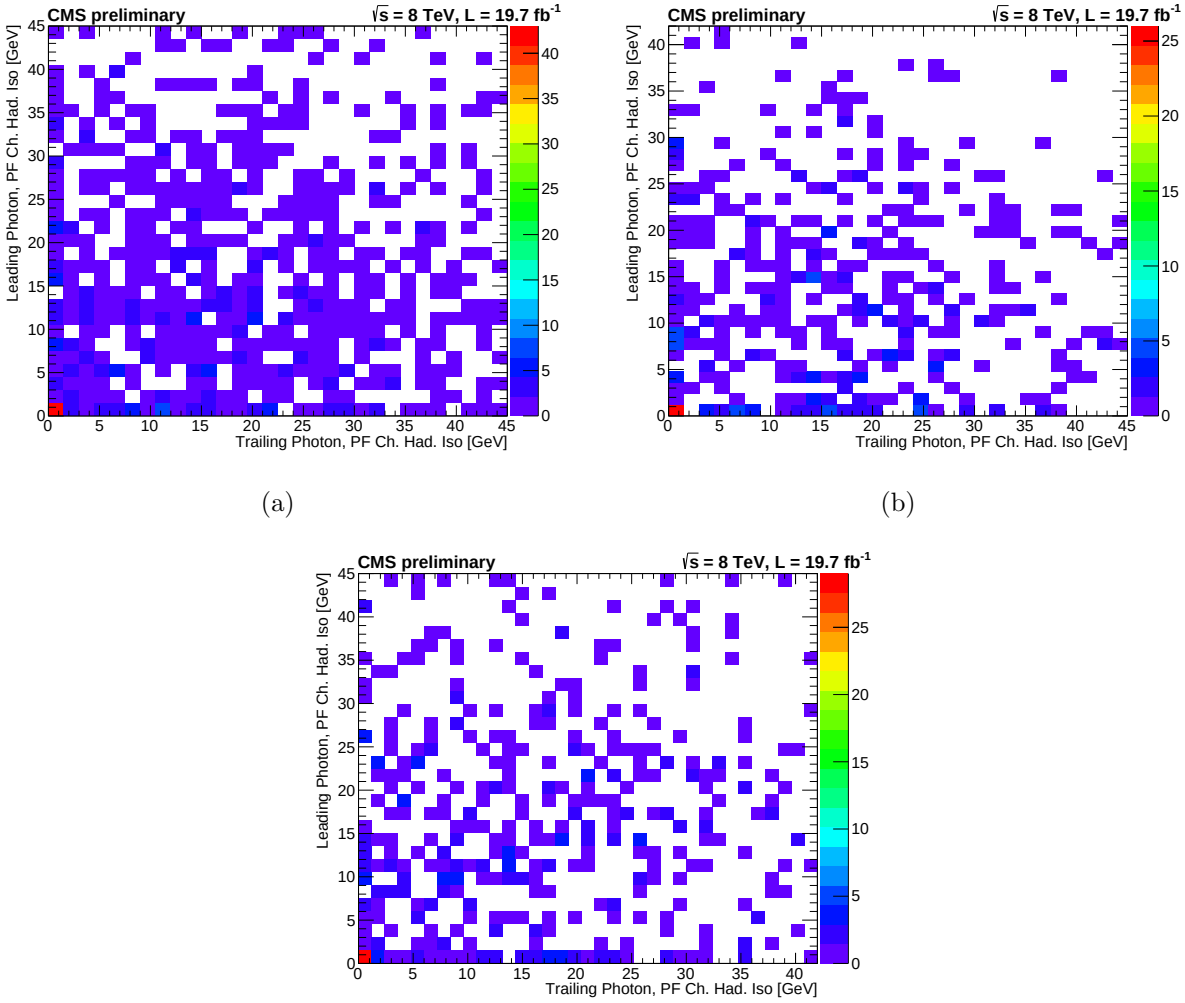

Figure 5.9: The distribution of PF charged hadron isolation when both photon candidates are misidentified jets (jj) in EB-EB (a), EB-EE (b), and EE-EB (c) regions.

5.4.3 Loosened Photon Requirements

The observed events after applying full selection criteria in where one or both photon candidates fail the observable requirement can be small that leads to large statistical uncertainties. We improve statistics with loosened photon $\sigma_{i\eta i\eta}$ requirements on each photon candidates that fall in (PF, FP, FF) region to trade off statistical uncertainty with systematic uncertainty [85]. The applying loosened photon $\sigma_{i\eta i\eta}$ requirements with good agreement with nominal requirements, but good decrease in statistics uncertainty. The observed data events are scaled by the probability of the loosened requirements relative to the nominal requirements. This probability is determined in the Z + jets background region to evaluate the probability of misidentified jet. Therefore, using this method, the value of N_{PF} is determined by loosening requirement on the trailing photon candidate and scaling the observed number of events by the probability of nominal requirements relative to the loosened requirements. Similarly, the value of N_{FP} is determined by loosening requirement on the leading photon candidate and scaling the observed number of events by the probability of the nominal requirements relative to the loosened requirements. In the background region where both photon candidates fail PF charged hadron isolation requirement, the value of N_{FF} is the average of the scaled data from loosening requirements on the leading and trailing photon candidates separately. The value of the loosened photon $\sigma_{i\eta i\eta}$ is required to be less than 0.029 in EB and 0.087 in EE region. The values of the loosened requirements depend on PF charged hadron isolation distributions.

5.4.4 Validation with single photon events

The performance of "matrix method" is validated by comparing simulations with data to Zγ production. Events are required the three body invariant mass M(ℓ, ℓ, γ) has to be greater than 105 GeV to enrich the contribution from jets misidentified as photon candidates. In addition, the invariant mass of two lepton candidates is required to satisfy M$(\ell, \ell) > 60$ GeV. With single photon events, the matrix form is defined as:

$$\begin{pmatrix} N_P \\ N_F \end{pmatrix} = \begin{pmatrix} \epsilon_\gamma^P & \epsilon_j^P \\ \epsilon_\gamma^F & \epsilon_j^F \end{pmatrix} \begin{pmatrix} \alpha_\gamma \\ \alpha_j \end{pmatrix} \tag{5.3}$$

The validation process is performed in the Zγ control region where we select two muon candidates that are consistent with the Z boson and one photon candidate. This Zγ control region largely overlaps with the region where misidentified jets are determined, so we consider this region to be a closure test. Figure 5.10 shows the comparison between data and estimated background predictions and true photons predictions from simulation in EB and EE region. In this Zγ validation procedure, we find that the excellent agreement between data and the true photon predictions from simulation plus the predictions of misidentified jets from matrix method.

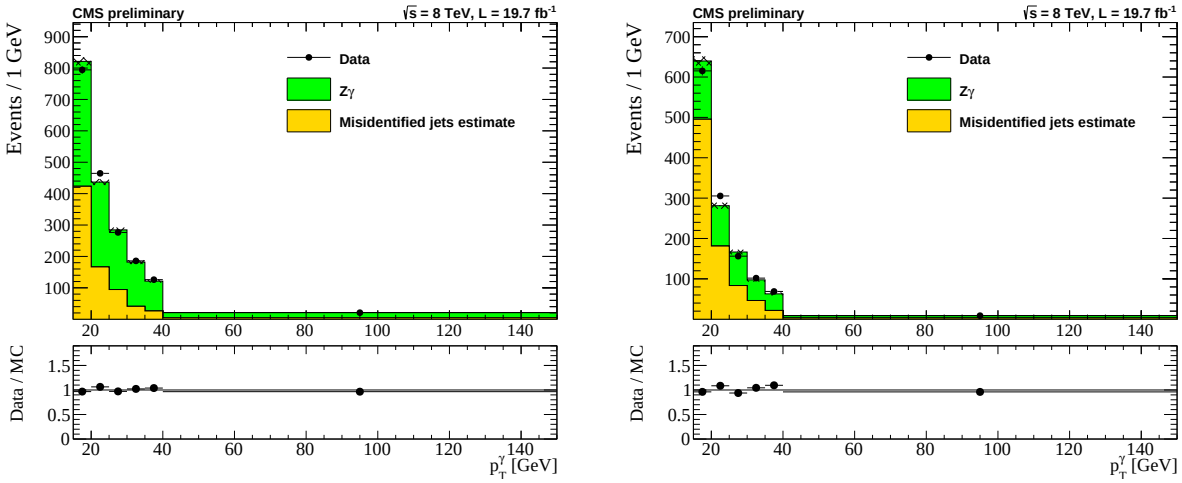

Figure 5.10: The comparison between the true photon predictions from simulation plus the misidentified jets predictions from the matrix method and data in dimuon plus photon events in muon (top) and electron (bottom) channel in EB (left) and EE (right).

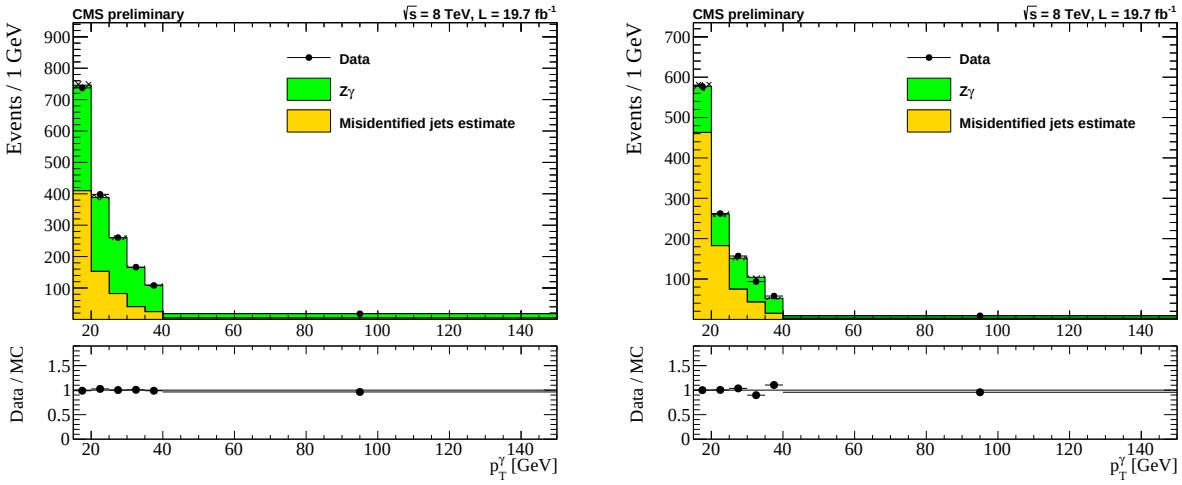

(c) (d)

Figure 5.10: The comparison between the true photon predictions from simulation plus the misidentified jets predictions from the matrix method and data in dimuon plus photon events in muon (top) and electron (bottom) channel in EB (left) and EE (right).

5.4.5 Results from Matrix Method Fitting

The matrix method is performed using the nominal and loosened photon $\sigma_{i\eta i\eta}$ requirement in each η region (EB-EB, EB-EE, EE-EB) for the electron and muon channel. Background predictions are evaluated in PP region. The results obtained from using loosened photon requirements that have smaller statistical uncertainty and agree well with nominal photon requirements. The evaluated predictions applying loosened $\sigma_{i\eta i\eta}$ requirements are shown in Appendix A.3. Figure 5.11 shows the background predictions in PP region from the matrix method with Z$\gamma\gamma$ signal predictions from simulation are compared to the data where both photon candidates pass all selections. We have an excellent agreement within statistical uncertainty.

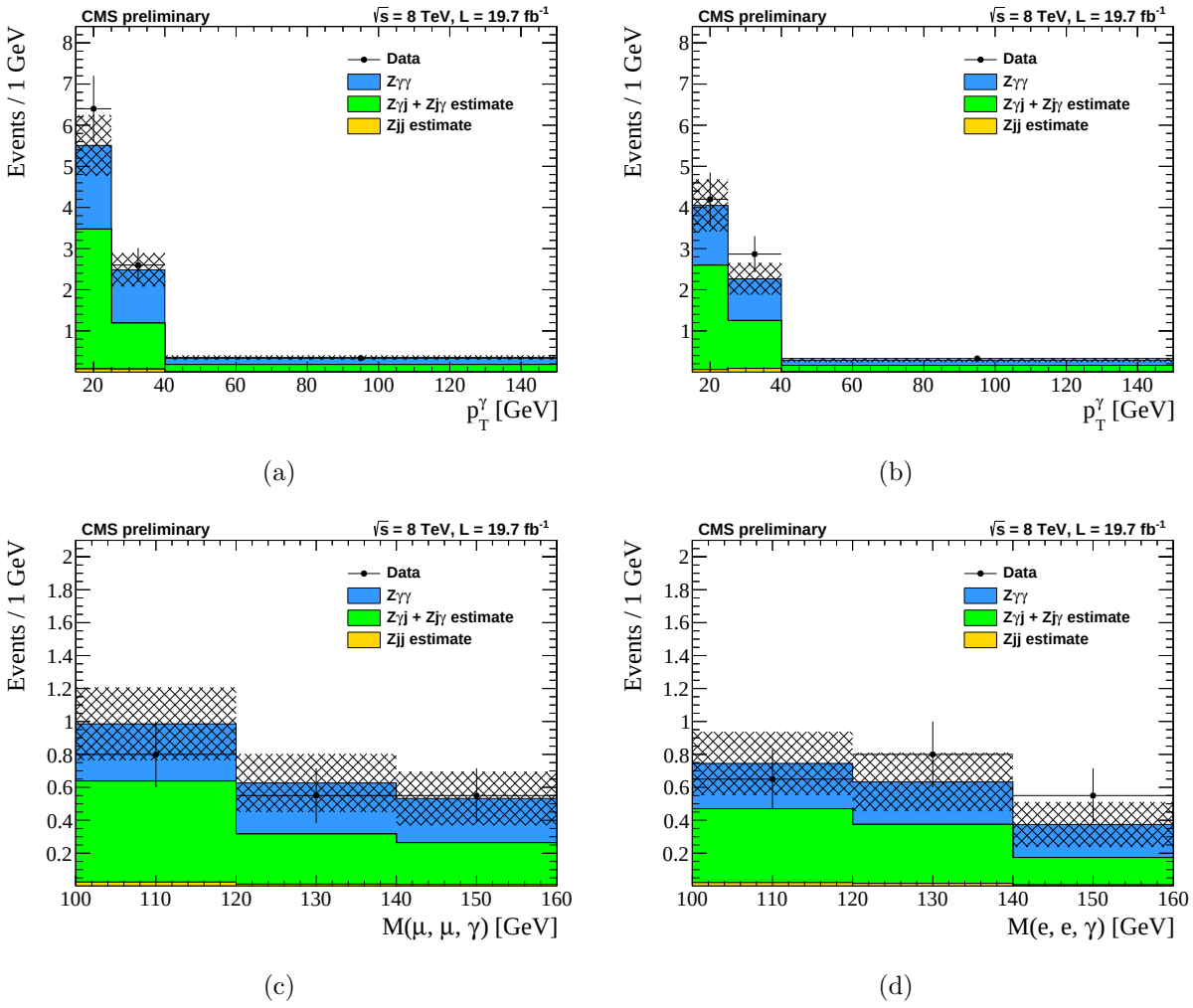

Figure 5.11: The comparison of p_{T}^{γ} of leading photon (a, b), three-body mass, $\mathrm{M}(\ell,\ell,\gamma)$, (c, d) and four-body mass, $\mathrm{M}(\ell,\ell,\gamma,\gamma)$, (e, f) distributions between the background predictions in PP region from the matrix method with $\mathrm{Z}\gamma\gamma$ signal predictions from simulation and data for muon channel (left) and electron channel (right). The hashed areas show the total statistical uncertainty on the background estimate.

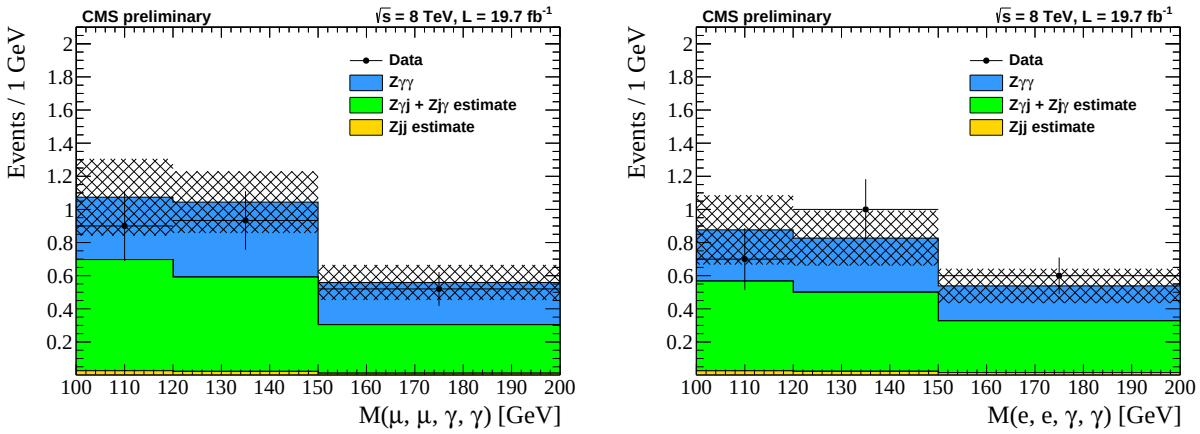

(e) (f)

Figure 5.11: The comparison of p_{T}^{γ} of leading photon (a, b), three-body mass, M(ℓ, ℓ, γ), (c, d) and four-body mass, M$(\ell, \ell, \gamma, \gamma)$, (e, f) distributions between the background predictions in PP region from the matrix method with Z$\gamma\gamma$ signal predictions from simulation and data for muon channel (left) and electron channel (right). The hashed areas show the total statistical uncertainty on the background estimate.

5.4.6 Cross Check the Method with $\sigma_{i\eta i\eta}$

The performance of method to estimate backgrounds is repeated using $\sigma_{i\eta i\eta}$ distribution as a cross check purpose. In the estimation of backgrounds, the sideband definition and loosened photon requirements are determined by isolation of photon candidates. Table 5.19 shows the sideband definition to $\sigma_{i\eta i\eta}$ distribution.

Selection	Sideband definition
Nominal	1.5 (1.2) < PF Ch. Had. Iso. < 12.0 (12.0), 0.7 (1.0) < PF Pho. Iso. < 9.0 (9.0)
Tight	1.5 (1.2) < PF Ch. Had. Iso. < 10.0 (10.0), 0.7 (1.0) < PF Pho. Iso. < 7.0 (7.0)
Loose	1.5 (1.2) < PF Ch. Had. Iso. < 15.0 (15.0), 0.7 (1.0) < PF Pho. Iso. < 11.0 (11.0)
Looser	1.5 (1.2) < PF Ch. Had. Iso. < 20.0 (20.0), 0.7 (1.0) < PF Pho. Iso. < 16.0 (16.0)

Table 5.19: The sideband definition to define misidentified jets to $\sigma_{i\eta i\eta}$. The numbers are in brackets in EE region.

The values of the loosened requirements depend on $\sigma_{i\eta i\eta}$ distributions. The requirements are progressively loosened on three isolation variables for photon candidates, which

are for "PF charged hadron isolation", "PF neutral hadron isolation", and "PF photon isolation". The value of those loosened isolation requirements are, in order of loosening, [5,3,3], [8,5,5], [10,7,7], [12,9,9], [15,11,11], and [20,16,16]. The results of matrix method using $\sigma_{i\eta i\eta}$ distribution also obtained from the loosened photon isolation that have smaller statistical uncertainty and agree well with nominal isolation requirements as well as using PF charged hadron isolation. Figure 5.12 shows the comparison between the data and background prediction with signal predictions from simulation in PP region when we use $\sigma_{i\eta i\eta}$ as the observable. We have good agreement within statistical uncertainty as well as use PF charged hadron isolation to the observable.

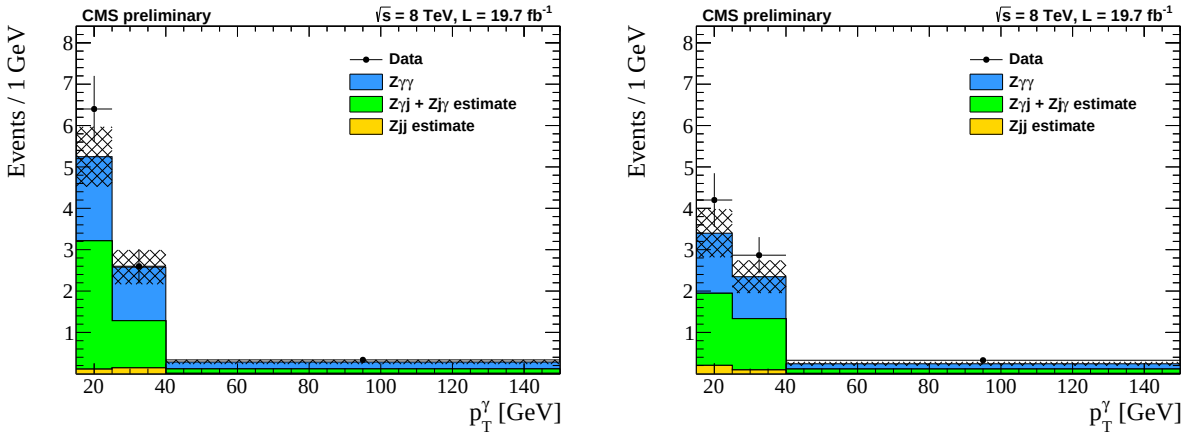

(a) (b)

Figure 5.12: The comparison of p_{T}^{γ} of leading photon (a, b), three-body mass, M(ℓ,ℓ,γ), (c, d) and four-body mass, M$(\ell,\ell,\gamma,\gamma)$, (e, f) distributions between the background predictions in PP region from the matrix method with Z$\gamma\gamma$ signal predictions from simulation and data for muon channel (left) and electron channel (right). The hashed areas show the total statistical uncertainty on the background estimate.

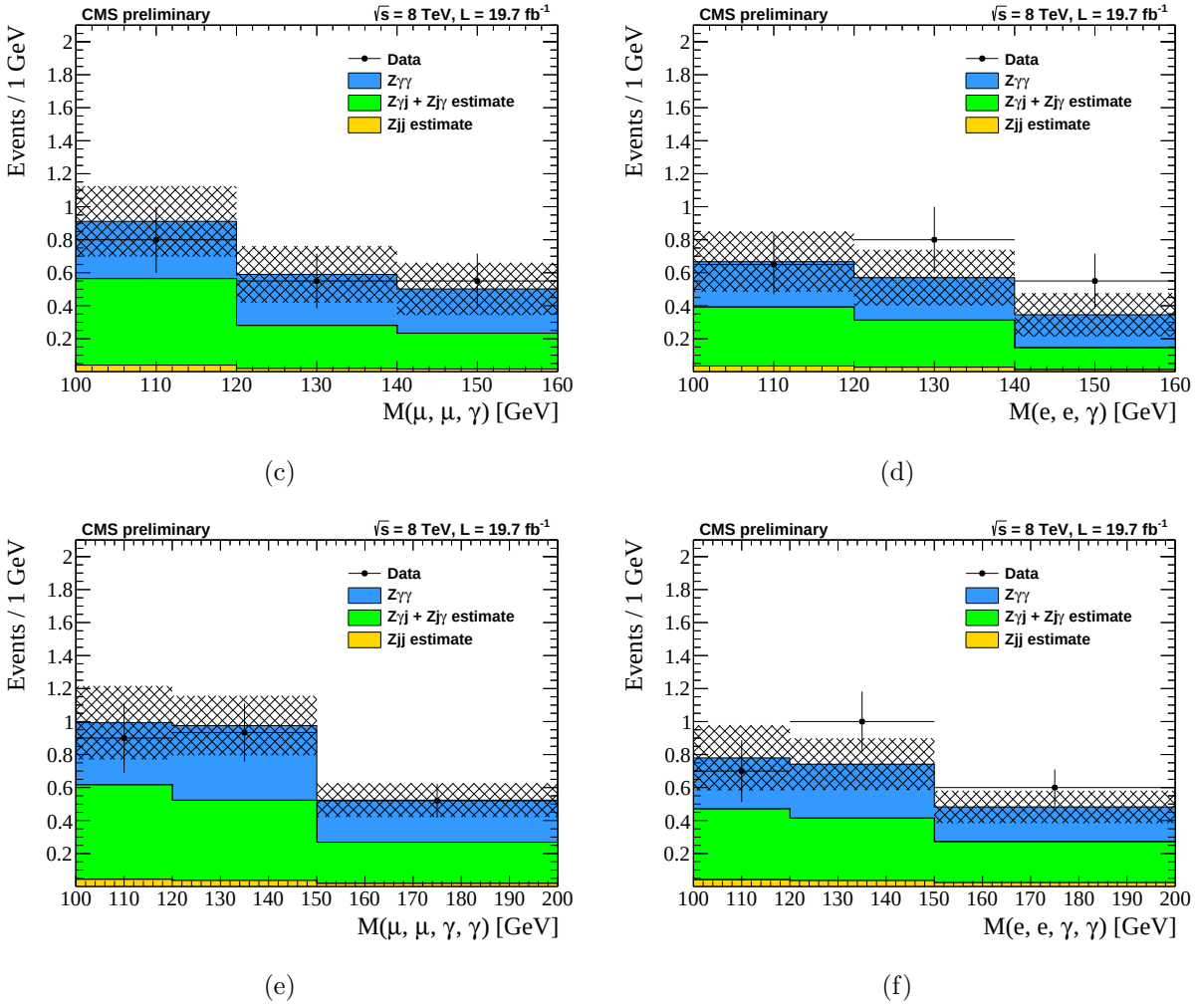

Figure 5.12: The comparison of p_{T}^{γ} of leading photon (a, b), three-body mass, $\mathrm{M}(\ell,\ell,\gamma)$, (c, d) and four-body mass, $\mathrm{M}(\ell,\ell,\gamma,\gamma)$, (e, f) distributions between the background predictions in PP region from the matrix method with $\mathrm{Z}\gamma\gamma$ signal predictions from simulation and data for muon channel (left) and electron channel (right). The hashed areas show the total statistical uncertainty on the background estimate.

5.5 Zγγ Acceptance

The cross section of Zγγ production is measured within a fiducial region defined by two leptons with two photons with leading photon $p_{\mathrm{T}} > 15\,\mathrm{GeV}$. In order to minimize extrapolations from the selected events, the fiducial region is mirrored to the offline event selection as closely as possible. Table 5.20 shows the fiducial region used in the Zγγ cross section measurement.

Definition of Zγγ Fiducial Region
Candidate Photon: $p_{\mathrm{T}} > 15\,\mathrm{GeV}$, $\lvert\eta\rvert < 2.5$, and no jet parentage Candidate Lepton: $p_{\mathrm{T}} > 10\,\mathrm{GeV}$, $\lvert\eta\rvert < 2.4$, Z or τ parent, and no jet parentage
Exactly 2 (same type) candidate leptons and 2 candidate photons Leading lepton $p_{\mathrm{T}} > 20\,\mathrm{GeV}$ $\mathrm{M}(\ell,\,\ell) > 40\,\mathrm{GeV}$ $\Delta\mathrm{R}(\gamma,\,\gamma) > 0.4$, $\Delta\mathrm{R}(\gamma,\,\ell) > 0.4$, and $\Delta\mathrm{R}(\ell,\,\ell) > 0.4$

Table 5.20: Definition of the fiducial region used for Zγγ cross section measurement.

Fiducial Requirements	$\mathrm{Z}\gamma\gamma \to \mu\mu\gamma\gamma$	$\mathrm{Z}\gamma\gamma \to ee\gamma\gamma$
Exactly 2, same tyle leptons	3586.3±13.6	3592.6±13.6
Exactly 2 photons	745.2±5.8	750.0±5.8
Leading lepton $p_{\mathrm{T}} > 20\,\mathrm{GeV}$	677.9±5.5	684.1±5.5
$\mathrm{M}(\ell,\,\ell) > 40\,\mathrm{GeV}$	589.9±5.1	596.1±5.2
$\Delta\mathrm{R}(\ell,\,\ell) > 0.4$	589.8±5.1	595.8±5.2
$\Delta\mathrm{R}(\gamma,\,\gamma) > 0.4$	562.2±5.0	567.2±5.0
$\Delta\mathrm{R}(\gamma,\,\ell) > 0.4$	249.5±3.4	251.4±3.4

Table 5.21: CutFlow for the Zγγ generated events in fiducial region.

The Zγγ production cross section in defined fiducial region is calculated as:

$$\sigma(pp \to \ell\ell\gamma\gamma)_{Fiducial} = (1 - f_{\tau}) \cdot \frac{N_{obs} - N_{bkg}}{C_{Z\gamma\gamma} \cdot \mathcal{L}} \tag{5.4}$$

where N_{obs} is the observed number of events in PP region, N_{bkg} is the predicted number of background events in PP region evaluated by matrix method (described in Section 5.4),

f_τ is the fraction of events from τ decay to electron or muon, $C_{Z\gamma\gamma}$ is the acceptance and correction factor for selected events, and $\mathcal{L}$ is the integrated luminosity. The acceptance, $C_{Z\gamma\gamma}$, and the fraction of events from τ decay, f_τ, are calculated as:

$$C_{Z\gamma\gamma} = \frac{N_{reco}[Z\gamma\gamma \to \ell\ell\gamma\gamma] + N_{reco}[Z\gamma\gamma \to \tau\tau\gamma\gamma \to \ell\nu\nu\ell\nu\nu\gamma\gamma]}{N_{gen}[Z\gamma\gamma \to \ell\ell\gamma\gamma(fiducial)] + N_{gen}[Z\gamma\gamma \to \tau\tau\gamma\gamma \to \ell\nu\nu\ell\nu\nu\gamma\gamma(fiducial)]} \tag{5.5}$$

$$f_\tau = \frac{N_{gen}[Z\gamma\gamma \to \tau\tau\gamma\gamma \to \ell\nu\nu\ell\nu\nu\gamma\gamma(fiducial)]}{N_{gen}[Z\gamma\gamma \to \ell\ell\gamma\gamma(fiducial)] + N_{gen}[Z\gamma\gamma \to \tau\tau\gamma\gamma \to \ell\nu\nu\ell\nu\nu\gamma\gamma(fiducial)]} \tag{5.6}$$

The τ backgrounds are subtracted by f_τ estimated at 0.30% in electron channel and 0.31% in muon channel. The $C_{Z\gamma\gamma}$ and f_τ are evaluated from MC simulations. These terms are canceled when we take their ratio as $\frac{C_{Z\gamma\gamma}}{(1-f_\tau)}$. Table 5.22 shows $\frac{C_{Z\gamma\gamma}}{(1-f_\tau)}$ in each leading photon p_{T} bin.

Leading photon p_{T}	$Z\gamma\gamma \to \mu\mu\gamma\gamma$	$Z\gamma\gamma \to ee\gamma\gamma$
15-25	$27.53\pm1.33^{+1.13}_{-1.12}$	$19.32\pm1.09^{+1.18}_{-1.16}$
25-40	$28.23\pm1.44^{+0.99}_{-0.99}$	$22.88\pm1.27^{+1.24}_{-1.23}$
40+	$32.10\pm1.66^{+1.15}_{-1.15}$	$26.17\pm1.50^{+1.17}_{-1.17}$
Total (p_{T} >15 GeV)	$29.11\pm0.84^{+1.53}_{-1.14}$	$22.49\pm0.73^{+1.40}_{-1.17}$

Table 5.22: The $Z\gamma\gamma$ acceptance, $\frac{C_{Z\gamma\gamma}}{(1-f_\tau)}$, in fiducial region in each leading photon p_{T} bin.

5.6 Systematic Uncertanty on the Cross Section

The sources of systematic uncertainties considered in the cross section measurements in this analysis are given by the uncertainty in the luminosity evaluation, the uncertainty in the detector performance, the uncertainty related to the simulation sample, and the uncertainty from background estimation. The source of systematic uncertainties are explained in the following list and summarized in Table 5.23, 5.24, and 5.25. These systematic uncertainties

are summed up quadratically and Table 5.26 shows contributions of group uncertainties. The systematic uncertainties need to be considered for the muon and electron channel, respectively.

- **uncertainty in the luminosity evaluation** : The systematic uncertainty in the measured integrated luminosity is taken to be 2.6% [86].

- **uncertainty in the dilepton trigger, lepton and photon identification and isolation efficiency evaluations** : The efficiencies are scaled up and down with respect to the nominal performance provided by the Muon POGs [87] and Egamma POGs [81].

- **uncertainty in the pile-up reweighting** : The pile-up reweighting are adjusted up and down with 5% minimum-bias cross section.

- **uncertainty due to the PDF** : The PDF uncertainty is calculated from the change in our acceptance depending on the used PDF sets. Our Z$\gamma\gamma$ signal samples used NLO `NNPDF3.0` that we compared to the `CT10` [88] and `MSTW2008` [89] sets.

- **uncertainty in factorization and renormalization scale** : The factorization and renormalization scale uncertainty will be source of systematic uncertainty. Simulation samples are dedicated with doubled and halved factorization and renormalization scales for the Z$\gamma\gamma$ signal.

- **uncertainty from background estimation** : Systematic uncertainties from backgrounds estimation are evaluated to account for PF charged hadron isolation shape and for correlations induced on each photon candidate when photon candidates are required looser isolation.

  - uncertainty in data in sideband region : The statistical uncertainty in observed data in sideband regions of the background estimates contribute.

– uncertainty in ϵ_γ and ϵ_j : The uncertainty in photon candidates and misidentified jets to pass or fail the observable requirement propagate into the uncertainty on the γ j, j γ, and j j background normalization.

– uncertainty in the shape of observable : The uncertainty in the shape of the observable distribution of genuine photons is determined by comparing between matched true photons in simulated events and data for FSR Z$\rightarrow \mu\mu\gamma$ process. The uncertainty in the shape of the observable distribution of misidentified jets is determined by comparing the PF charged hadron isolation distribution required nominal $\sigma_{i\eta i\eta}$ to distribution required looser $\sigma_{i\eta i\eta}$. Figure 5.13 and 5.14 show the comparison of PF charged hadron distribution to determine shape uncertainty in observable.

– uncertainty in Zγ contribution : The probability of misidentified jets receive an uncertainty from subtraction of true photon candidates using Zγ simulation. Uncertainties in Zγ contribution are correlated between η bins.

– uncertainty in j j shape : The distribution of j j account for the correlations between one and the other photon objects in data events. To produce signal free sample, we require inverted requirements of photon candidates. The requirements that define the sideband regions are varied to estimate uncertainty (see Table 5.17). The maximum difference in the results compare to nominal requirement is taken to the uncertainty.

– uncertainty in cross correlation between two photons : An additional uncertainty is evaluated from cross correlation between two photon candidates. It is defined by the observable distribution shape of misidentified jets when both photons are required nominal $\sigma_{i\eta i\eta}$ compare to the distribution shape when one of photon is required loosened $\sigma_{i\eta i\eta}$. Figure 5.15 shows the distribution used to determine for uncertainty in cross correlation. For the distribution required loosened $\sigma_{i\eta i\eta}$, we apply 10% uncertainty consistently. Uncertainties in cross correlation between

two photons are correlated between η bins.

Systematic source	$Z\gamma\gamma \to \mu\mu\gamma\gamma$, (%)	$Z\gamma\gamma \to ee\gamma\gamma$, (%)
Uncertainty in luminosity	±2.6	±2.6
Detector Performance Modeling		
Uncertainty in dilepton trigger	±1.20	±1.33
Uncertainty in photon identification	±2.82	±2.78
Uncertainty in photon conversion save electron veto	±0.76	±0.76
Uncertainty in muon identification	±0.41	
Uncertainty in muon isolation	±0.21	
Uncertainty in electron identification		±3.71
Uncertainty in photon and electron energy scale	+3.57/-0.96	+3.47/-0.80
Uncertainty in muon energy scale	+1.72/-1.48	
Uncertainty in pile-up reweighting	±0.39	±1.49
Monte Carlo Simulation Modeling		
Statistical uncertainty in MC sample	±2.89	±3.25
Uncertainty in PDF sets	±0.24	±0.27
Uncertainty in PDF Eigenvectors	±1.17	±0.87
Uncertainty in factorization scale	±0.48	±0.24
Uncertainty in renormalization scale	±0.48	±0.49
Total uncertainty	+6.00/-4.85	+7.03/-6.15

Table 5.23: Summary of uncertainties in luminosity evaluation, the detector performance, and related simulation sample with leading photon $p_{\mathrm{T}} > 15\,\mathrm{GeV}$.

$Z\gamma\gamma \to \mu\mu\gamma\gamma$, (fb)				
Systematic source	EB-EB	EB-EE	EE-EB	Sum
Uncertainty in ϵ_γ and ϵ_j to Pass	0.33	0.17	0.40	0.55
Uncertainty in ϵ_γ and ϵ_j to Fail	0.29	0.16	0.20	0.39
Uncertainty in shape of observable	1.14	1.62	2.01	2.82
Uncertainty in $Z\gamma$ contribution	5.06	1.48	1.53	8.07
Uncertainty in j j shape	0.19	0.66	0.45	0.82
Uncertainty in cross correlation between two photons	0.10	0.10	0.10	0.30
Uncertainty in data in sideband region	0.64	0.36	0.42	0.85
Total uncertainty	5.25	2.33	2.64	8.66

Table 5.24: Summary of uncertainties from background estimation with leading photon $p_{\mathrm{T}} > 15\,\mathrm{GeV}$ in muon channel.

$Z\gamma\gamma \to ee\gamma\gamma$, (fb)				
Systematic source	EB-EB	EB-EE	EE-EB	Sum
Uncertainty in ϵ_γ and ϵ_j to Pass	0.25	0.17	0.18	0.35
Uncertainty in ϵ_γ and ϵ_j to Fail	0.22	0.16	0.16	0.31
Uncertainty in shape of observable	0.86	0.40	1.71	1.96
Uncertainty in $Z\gamma$ contribution	3.80	1.64	1.42	6.86
Uncertainty in j j shape	0.18	0.79	0.40	0.90
Uncertainty in cross correlation between two photons	0.10	0.10	0.10	0.30
Uncertainty in data in sideband region	0.50	0.40	0.36	0.73
Total uncertainty	3.95	1.92	2.30	7.25

Table 5.25: Summary of uncertainties from background estimation with leading photon $p_{\mathrm{T}} > 15\,\mathrm{GeV}$ in electron channel.

Systematic source	$Z\gamma\gamma \to \mu\mu\gamma\gamma$, (fb)	$Z\gamma\gamma \to ee\gamma\gamma$, (fb)	Combined, (fb)
Data Statistics	2.09	2.48	1.61
Luminosity	0.32	0.34	0.33
Detector Performance	0.62	0.77	0.56
MC Simulation	0.39	0.48	0.34
Background Estimation	1.51	1.64	1.57
Total uncertainty	2.70	3.13	2.37

Table 5.26: Summary of the $Z\gamma\gamma$ cross section uncertainties for each channel and combination of the two channels.

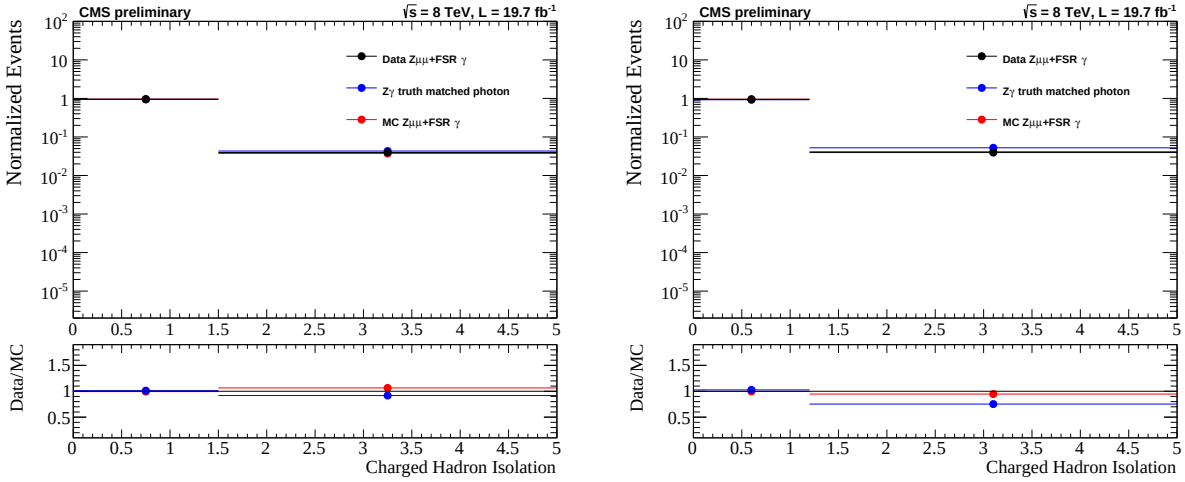

(a) (b)

Figure 5.13: The comparison of PF charged hadron isolation distribution between true photon in simulation (blue) and data for FSR Z $\rightarrow \mu\mu\gamma$ (black) in EB (a) and EE (b) region with $p_{\mathrm{T}} > 15\,\mathrm{GeV}$.

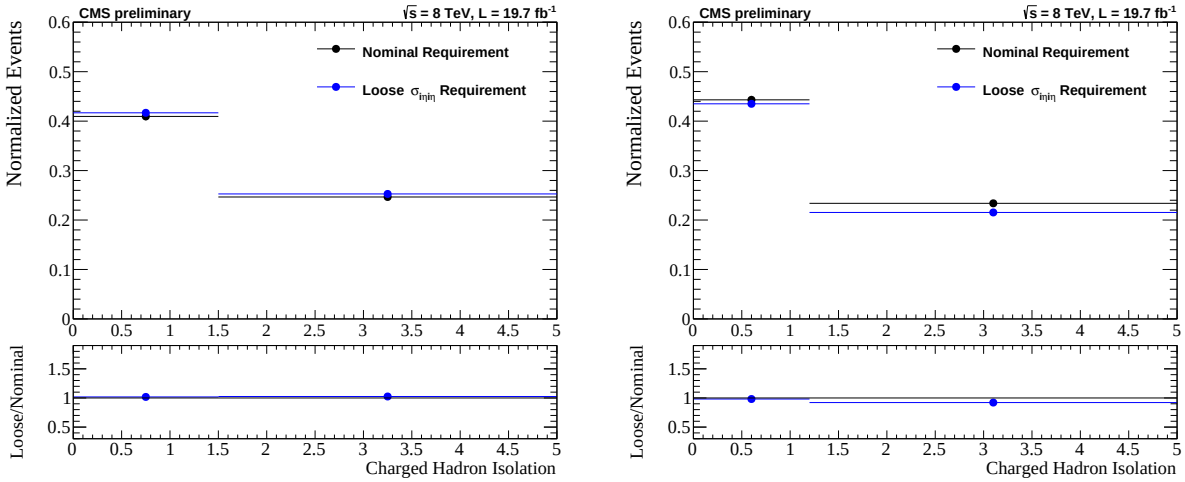

(a) (b)

Figure 5.14: The comparison between PF charged hadron isolation distribution applied nominal isolation and applied looser isolation in Z + jets data in EB (a) and EE (b) region with $p_{\mathrm{T}} > 15\,\mathrm{GeV}$.

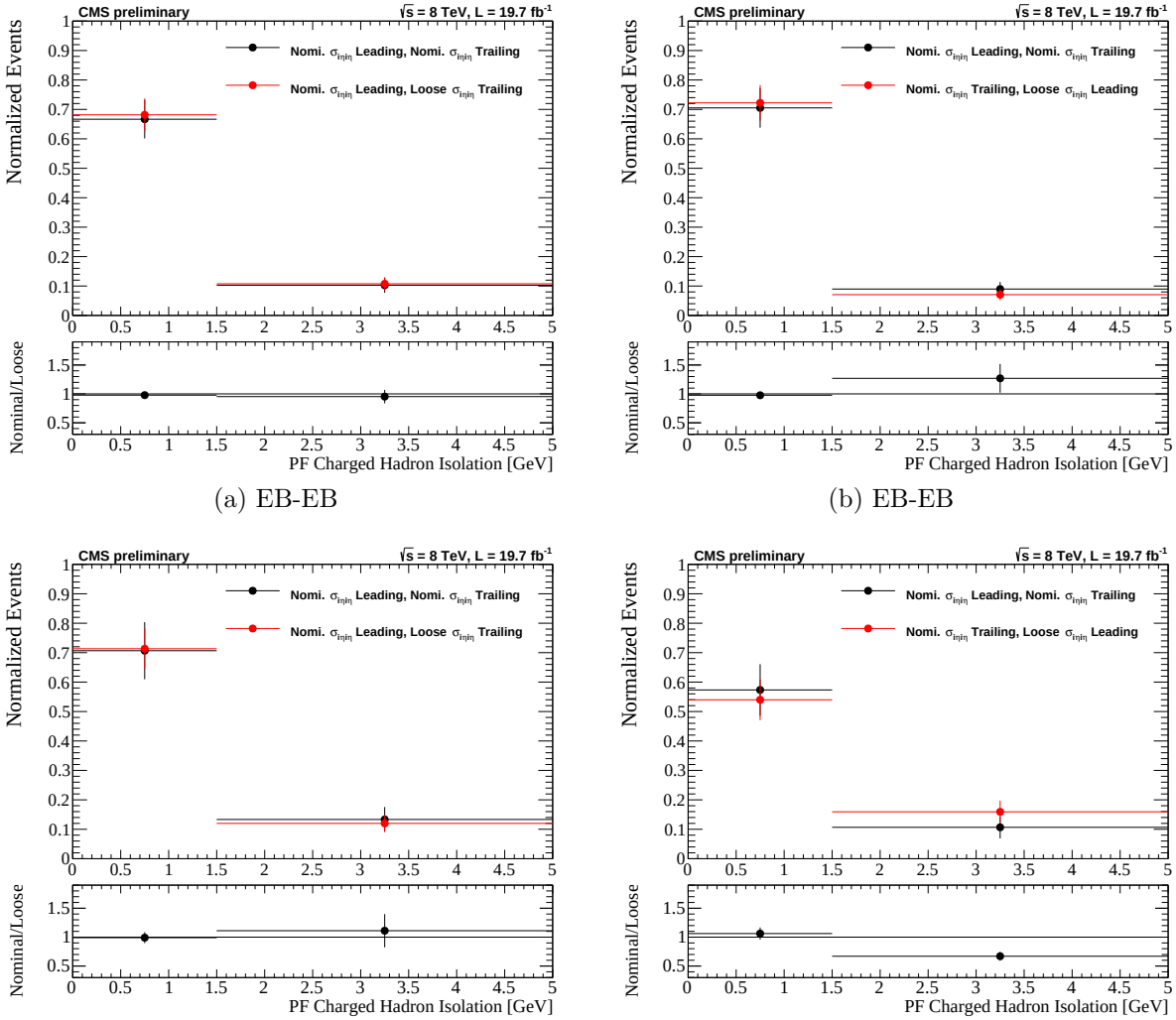

(a) EB-EB (b) EB-EB

(c) EB-EE (d) EB-EE

Figure 5.15: The comparison of PF charged hadron isolation distribution propagate to the leasing photon when the trailing photon is required loosened $\sigma_{i\eta i\eta}$ requirement (left) and to the trailing photon when the leading photon is required loosened $\sigma_{i\eta i\eta}$ requirement (right). Distributions are shown when the both photon candidates are in EB region (a, b) and when the leading photon is in EB region and trailing photon is in EE region (c, d), and the leading photon is in EE region and the trailing photon is in EB region (e, f).

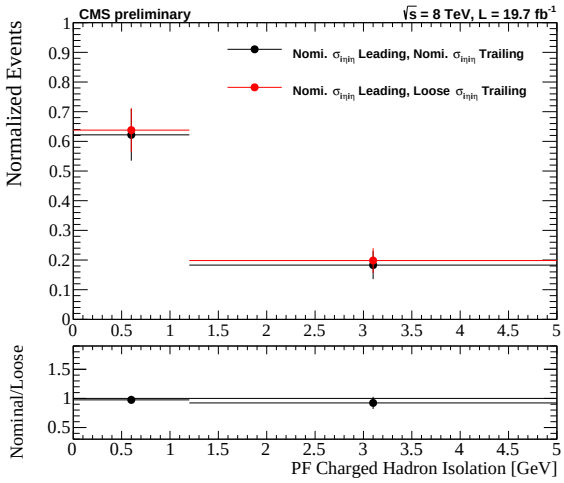

(e) EE-EB

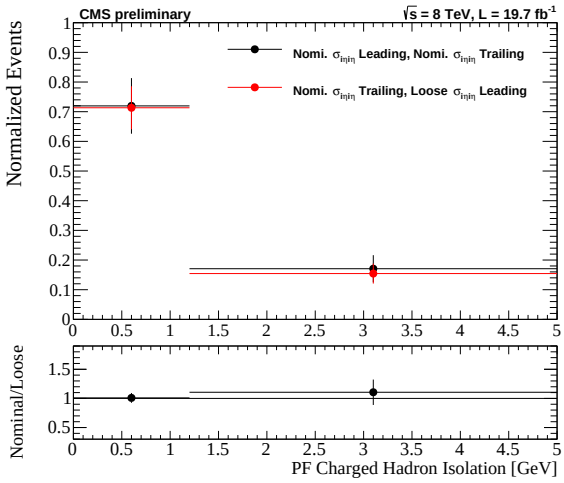

(f) EE-EB

Figure 5.15: The comparison of PF charged hadron isolation distribution propagate to the leasing photon when the trailing photon is required loosened $\sigma_{i\eta i\eta}$ requirement (left) and to the trailing photon when the leading photon is required loosened $\sigma_{i\eta i\eta}$ requirement (right). Distributions are shown when the both photon candidates are in EB region (a, b) and when the leading photon is in EB region and trailing photon is in EE region (c, d), and the leading photon is in EE region and the trailing photon is in EB region (e, f).

5.7 Results of Cross Section Measurement

The Z$\gamma\gamma$ fiducial cross section is finally measured with the equation 5.4 by combining the results described in the previous sections (N_{obs}, N_{bkg}, $C_{Z\gamma\gamma}$, f_{τ}, and $\mathcal{L}$). The cross section is calculated from contributions from Z$\gamma\gamma \to \mu\mu\gamma\gamma$ process and Z$\gamma\gamma \to ee\gamma\gamma$ process separately. Table 5.27 shows the individual fiducial cross sections separately for electron and muon channel.

Channel	$\sigma\,(pp \to \ell\ell\gamma\gamma)$ fb (stat., syst., lumi.)
Z$\gamma\gamma \to \mu\mu\gamma\gamma$	12.2 ± 2.1 (stat.) ± 1.7 (syst.) ± 0.3 (lumi.) fb
Z$\gamma\gamma \to ee\gamma\gamma$	13.0 ± 2.5 (stat.) ± 1.9 (syst.) ± 0.3 (lumi.) fb

Table 5.27: Measured cross section in Z$\gamma\gamma$ fiducial region in individual channels.

We use Best Linear Unbiased Estimator (BLUE) [90] technique to combine the individual cross sections to get the final cross section. Based on the BLUE method, the cross section

of two channel combination to be:

$$\sigma(pp \to \ell\ell\gamma\gamma)_{Fiducial} = 12.6 \pm 1.6\ (\text{stat.}) \pm 1.7\ (\text{syst.}) \pm 0.3\ (\text{lumi.})\,\text{fb}.$$

Three uncertainties are determined that originate from data statistics uncertainty, systematic uncertainties, and uncertainty of the integrated luminosity, respectively. The uncertainties on the measured cross section is calculated using the Equation A.2 in Appendix A.2.

Chapter 6

Conclusion

The measurement of the $Z\gamma\gamma$ production cross section at the CMS experiment is presented, and this is the first measurement at proton-proton collisions with 8 TeV data. The $Z\gamma\gamma$ final state that has two electrons or muons with two photons is measured in a fiducial region where leptons $p_T > 20/10$ GeV for leading and trailing respectively, leading photon $p_T > 15$ GeV, and invariant dilepton mass $M(\ell, \ell) > 40$ GeV. The fiducial cross section has been measured to be

$$12.6 \pm 1.6 \text{ (stat.)} \pm 1.7 \text{ (syst.)} \pm 0.3 \text{ (lumi.) fb.}$$

where stat., syst., and lumi. denote the statistical uncertainty, systematic uncertainty, and the uncertainty of integrated luminosity from CMS detector, respectively. The theoretical cross section calculated using $Z\gamma\gamma$ NLO signal sample is 13.0 ± 1.5 fb. The experimental results have an excellent agreement with theoretical result within their precision.

Bibliography

[1] A. Purcell, *CERN Buletin, GO ON A PARTICLE QUEST AT THE FIRST CERN WEBFEST*, http://cds.cern.ch/journal/CERNBulletin/2012/35/News%20Articles/1473657, The Standard Model infographic developed at the webfest.

[2] R. Coker, *Gauge Invariance*, https://web2.ph.utexas.edu/~coker2/index.files/gaugef.htm.

[3] C. Lefevre, *The CERN accelerator complex. Complexe des accelerateurs du CERN*, https://cds.cern.ch/record/1260465/export/hx?ln=en (Dec. 2008), CERN-DI-0812015.

[4] The CMS Collaboration, *CMS Luminosity-Public Results, Public CMS Luminosity Information*, http://cms-service-lumi.web.cern.ch/cms-service-lumi/publicplots/int_lumi_cumulative_pp_2.png, Comments: Delivered Luminosity versus time for 2010, 2011, 2012 (p-p data only).

[5] A. Ball and A. Rao, *The CMS detector description*, http://orbiterchspacenews.blogspot.com/2013/04/cern-cms-prepares-for-future.html.

[6] I. Chakaberia, *STUDY OF THE HELICITY DISTRIBUTIONS OF $Z\gamma$ PRODUCTION AT THE CMS EXPERIMENT*, Ph.D. Thesis, KANSAS STATE UNIVERSITY (2014).

[7] The CMS Collaboration, *The CMS experiment at the CERN LHC*, JINST 3, S08004, doi:10.1088/1748-0221/3/08/S08004 (2008).

[8] D. Sanders, *CMS Pixel Detector*, http://www.phy.olemiss.edu/HEP/cms/pixel/ (Nov. 2005), Figure 1: CMS Pixel Detector: 2x2 Configuration.

[9] T. Lenzi, *Development and Study of Different Muon Tracker Reconstruction Algorithms for the Level-1 Trigger for the CMS Muon Upgrade with GEM Detector*, MS. Thesis, arXiv:1306.0858 [physics.ins-det] (June 2013).

[10] B. Isildak, *Measurement of the differential dijet production cross section in proton-proton collisions at* $\sqrt{s} = 7$ *TeV*, Ph.D. Thesis, arXiv:1308.6064 [hep-ex] (2013).

[11] The CMS Collaboration, *ECAL Clustering*, https://twiki.cern.ch/twiki/pub/CMSPublic/SWGuideEcalRecoClustering/BasicCluster.png.

[12] S. Shrestha, *A MEASUREMENT OF* $Z(\nu\overline{\nu})\gamma$ *CROSS SECTION AND LIMITS ON ANOMALOUS TRIPLE GAUGE COUPLING AT* $\sqrt{s} = 7$ *TeV USING CMS*, Ph.D. Thesis, KANSAS STATE UNIVERSITY (2013).

[13] The L3 Collaboration, *Measurement of the* $e^+e^- \to Z\gamma\gamma$ *Cross Section and Determination of Quartic Gauge Boson Couplings at LEP*, Phys.Lett.B478:39-49, arXiv:hep-ex/0002037v1, doi:10.1016/S0370-2693(00)00279-3 (Feb. 2000).

[14] A. Gozzelino, *Search for heavy lepton partners of neutrinos in the context of type III seesw mechanism in 2012 LHC CMS data*, Phys. Lett. B 718 (2012) 348, arXiv:1210.1797v2 [hep-ex], doi:10.1016/j.physletb.2012.10.070 (2013), CMS-EXO-11-073; CERN-PH-EP-2012-278.

[15] E. Avdeeva, *ggNtuple MC Samples, 8 TeV*, https://twiki.cern.ch/twiki/bin/viewauth/CMS/GgNtupleMCSamples.

[16] CMS collaboration, *Effective area for rho correction*, https://twiki.cern.ch/twiki/bin/view/CMS/CutBasedPhotonID2012#Effective_Areas_for_rho_correcti.

[17] University of Tsukuba, http://www.tsukuba.ac.jp/english/community/oubo.html.

[18] Y. Okumura, *The top-quark pair-production cross-section measurement in the dilepton final states at proton-proton collisions with* $\sqrt{s} = 7$ *TeV*, Ph.D. Thesis, NAGOYA UNIVERSITY (2012).

[19] A. Pich, *The Standard Model of Electroweak Interactions*, CERN-2012-001, pp.1-50, arXiv:1201.0537v1 [hep-ph] (2012).

[20] T. Cahalan, *Dark Energy and Human Consciousness: Humanity's Path to Freedom* (BalboaPress, 2014).

[21] Berkeley Lab, *The Particle Adventure: Color charge*, http://www.particleadventure.org/color.html.

[22] A. V. Ferapontov, *MEASUREMENTS AND SEARCHES FOR NEW PHYSICS IN DI-BOSON PROCESSES WITH THE DØ DETECTOR*, Ph.D. Thesis, KANSAS STATE UNIVERSITY (2009).

[23] Berkeley Lab, *The Particle Adventure: Hadrons, Baryons, and Mesons*, http://www.particleadventure.org/hadrons.html.

[24] D. Griffiths, *Introduction to Elementary Particles* (WILEY-VCH Verlag GmbH & Co. KGaA, Weinheim, 2004).

[25] K. Jakobs and C. Seez, *The higgs Boson discovery*, http://www.scholarpedia.org/article/The_Higgs_Boson_discovery, doi:10.4249/scholarpedia.32413 (2015).

[26] P. Langacker, *Introduction to the Standard Model and Electroweak Physics*, arXiv:0901.0241 [hep-ph] (2009).

[27] G. Arnison et al., *Experimental observation of lepton pairs of invariant mass around 95* GeV/c^2 *at the CERN SPS collider*, Physics Letters B, Volume 126, Issue 5, Page 398-410, doi:10.1016/0370-2693(83)90188-0 (Jul. 1983).

[28] UA1 Collaboration (G. Arnison et al.), *Experimental observation of isolated large transverse energy electrons with associated missing energy at* $\sqrt{s} = 540$ *GeV*, Physics Letters B, Volume 122, Issue 1, Page 103-116, doi:10.1016/0370-2693(83)91177-2 (Feb. 1983).

[29] L. Xu, *Study of Electroweak and Higgs Physics with ZZ Productions at LHC*, Ph.D. Thesis, University of Science and Technology of China (2015).

[30] T. W. B. Kibble, *Symmetry Breaking in Non-Abelian Gauge Theories*, Phys. Rev. 155, 1554, doi:http://dx.doi.org/10.1103/PhysRev.155.1554 (1967).

[31] O. Bruning et al., *LHC Luminosity and Energy Upgrade: A Feasibility Study*, LHC Project Report 626 (Dec. 2002).

[32] K. Schindl, *THE INJECTOR CHAIN FOR THE LHC*, CERN/PS 99-018 (DI) (Jan. 1999), Workshop on LEP-SPS Performance, Chamonix IX.

[33] L. Evans and P. Bryant (editors), *LHC Machine*, JINST 3, S08001, doi:10.1088/1748-0221/3/08/S08001 (2008).

[34] The ATLAS Collaboration, *The ATLAS Experiment at the CERN Large Hadron Collider*, JINST 3, S08003, doi:10.1088/1748-0221/3/08/S08003 (2008).

[35] L. Taylor, *Observation of a New Particle with a Mass of 125 GeV*, http://cms.web.cern.ch/news/observation-new-particle-mass-125-gev (Jul. 2012), CMS Experiment, CERN.

[36] H. Murayama, *Introduction to Supersymmetry*, http://hitoshi.berkeley.edu/public_html/susy/susy.html (2000), Comments: This home page is based on the introduction in Supersymmetry Phenomenology by Hitoshi Murayama.

[37] The LHCb Collaboration, *The LHCb Detector at the LHC*, JINST 3, S08005, doi:10.1088/1748-0221/3/08/S08005 (2008).

[38] M. P. Altarelli and F. Teubert, *B Physics at LHCb*, arXiv:0802.1901 [hep-ph], doi:10.1142/S0217751X08042791 (Feb. 2008), Comments: 26 pages, Contribution to "Perspectives on LHC Physics", ed. G.Kane and A.Pierce.

[39] The ALICE Collaboration, *The ALICE Experiment at the CERN LHC*, JINST 3, S08002, doi:10.1088/1748-0221/3/08/S08002 (2008).

[40] CERN timelines, *The Large Hadron Collider*, http://timeline.web.cern.ch/timelines/The-Large-Hadron-Collider?page=3.

[41] P. L. Rocca and F. Riggi, *The upgrade program of the major experiments at the Large Hadron Collider*, Journal of Physics: Conference Series 515 (2014) 012012, doi:10.1088/1742-6596/515/1/012012.

[42] V. Relovic, *CMS.FourVector*, https://twiki.cern.ch/twiki/bin/view/CMSPublic/SWGuideFourVector.

[43] A. K. Nayak, *Reconstruction of physics objects in the CMS detector*, arXiv:1310.7408v1 [hep-ex] (Oct. 2013).

[44] D. Acosta et al. (Editor), *CMS Physics Technical Design Report Volume I: Detector Performance and Software*, CERN/LHCC 2006-001, CMS TDR 8.1 (Feb. 2006).

[45] S. Norberg, *Inner Tracker*, https://twiki.cern.ch/twiki/bin/view/CMSPublic/WorkBookCMSExperiment#InnerTracker.

[46] J. L. Leonard, *Z BOSON CROSS SECTION MEASUREMENT USING AT THE LHC*, Ph.D. Thesis, UNIVERSITY OF WISCONSIN - MADISON (2011).

[47] L. Taylor, *Silicon Pixels*, http://cms.web.cern.ch/news/silicon-pixels.

[48] T. Lenzi, *Development and Study of Different Muon Track Reconstruction Algorithms for the Level-1 Trigger for the CMS Muon Upgrade with GEM Detectors*, MS. Thesis, arXiv:1306.0858 [physics.ins-det] (2013).

[49] The CMS Collaboration, *Energy calibration and resolution of the CMS electromagnetic calorimeter in pp collisions at* $\sqrt{s}$*=7 TeV*, JINST 8 (2013) P09009, arXiv:1306.2016v2 [hep-ex], doi:10.1088/1748-0221/8/09/P09009 (2013).

[50] L. Taylor, *ECAL Preshower*, http://cms.web.cern.ch/news/ecal-preshower.

[51] M. Radziej, *RESONANT SLEPTON PRODUCTIONIN THE TWO MUON + JETS FINAL STATE AT* $\sqrt{s}$ *= 8 TEV*, Ph.D. Thesis, RWTH AACHEN UNIVERSITY (2014).

[52] The CMS Collaboration, *Performance of the CMS Hadronic Calorimeter with Cosmic Ray Muons and LHC Beam Data*, JINST 5:T03012, arXiv:0911.4991v3 [physics.ins-det], doi:10.1088/1748-0221/5/03/T03012 (2010), CMS-CFT-09-009.

[53] Integrated Infrastructure Initiative for Neutron Scattering and Muon Spectroscopy, *The characteristics of muons*, http://nmi3.eu/muon-research/characteristics-of-muons.html.

[54] L. Taylor, *Muon Detectors*, http://cms.web.cern.ch/news/muon-detectors.

[55] L. Taylor, *Muon Drift Tubes*, http://cms.web.cern.ch/news/muon-drift-tubes.

[56] D. Acosta, *Muon Detectors in CMS*, http://www.phys.ufl.edu/~acosta/cms/cmshi.pdf.

[57] L. Taylor, *Triggering and Data Acquisition*, http://cms.web.cern.ch/news/triggering-and-data-acquisition (2011).

[58] M. Makouski, *A MEASUREMENT OF TOP QUARK PAIR AND PHOTON PRODUCTION CROSS SECTION WITH CMS DETECTOR*, Ph.D. Thesis, KANSAS STATE UNIVERSITY (2015).

[59] The CMS Collaboration, *Particle-Flow Event Reconstruction in CMS and Performance for Jets, Taus, and* E_{T}^{miss}, CMS PAS PFT-09-001 (2009).

[60] The CMS Collaboration, *Hybrid superclusters*, https://twiki.cern.ch/twiki/bin/view/CMSPublic/SWGuideEcalRecoClustering#HybriD.

[61] S. Toda, *Identifying Elementary Particles From High Energy Collections Produced by The Large Hadron Collider at CERN*, http://neutrino.phys.ksu.edu/ksuheptrac/attachment/wiki/PostersandTalks/KRFPosterFinalVersion3-24SPM.pdf (2014).

[62] The CMS Collaboration, *CMS Physics Technical Design Report Volume I: Detector Performance and Software*, CERN-LHCC-2006-001 ; CMS-TDR-8-1 (2006).

[63] The CMS Collaboration, *Performance of CMS muon reconstruction in pp collision events at* $\sqrt{s} = 7$ *TeV*, JINST 7 (2012) P10002, arXiv:1206.4071 [physics.ins-det], doi: 10.1088/1748-0221/7/10/P10002 (2012), CMS-MUO-10-004; CERN-PH-EP-2012-173.

[64] The CMS Collaboration, *Public CMS Luminosity Information*, https://twiki.cern.ch/twiki/bin/view/CMSPublic/LumiPublicResults.

[65] CMS collaboration, *ECALELF*, https://twiki.cern.ch/twiki/bin/view/CMSPublic/ECTWiki.

[66] J. Alwall et al., *MadGraph 5: Going Beyond*, arXiv:1106.0522 [hep-ph], doi:10.1007/JHEP06(2011)128 (2011).

[67] R. D. Ball, V. Bertone, S. Carrazza, C. S. Deans, L. D. Debbio, S. Forte, A. Guffanti, N. P. Hartland, J. I. Latorre, J. Rojo, and M. Ubiali, *Parton distributions for the LHC Run II*, arXiv:1410.8849 [hep-ph], doi:10.1007/JHEP04(2015)040 (2015).

[68] T. Sjostrand, S. Mrenna, and P.Z. Skands, *PYTHIA 6.4 Physics and Manual*, arXiv:0603175 [hep-ph], doi:10.1088/1126-6708/2006/05/026 (2006).

[69] GEANT4 Collaboration, *GEANT4: A Simulation toolkit*, Nucl.Instrum.Meth. A506 (2003) 250-303, doi:10.1016/S0168-9002(03)01368-8, SLAC-PUB-9350, FERMILAB-PUB-03-339 (2003).

[70] CMS collaboration, *Cut based electron ID 2012*, https://twiki.cern.ch/twiki/bin/view/CMS/EgammaCutBasedIdentification.

[71] CMS collaboration, *Electron ID Algorithms*, https://twiki.cern.ch/twiki/bin/view/CMSPublic/SWGuideElectronID#Electron_ID_Algorithms (2010).

[72] The CMS collaboration, *Commissioning of the Particle-flow Event Reconstruction with the first LHC collisions recorded in the CMS detector*, CMS PAS PFT-10/001 (2010).

[73] CMS collaboration, *Electron PF Isolation*, https://twiki.cern.ch/twiki/bin/view/CMS/EgammaEARhoCorrection#Effective_Areas_calculated_on_da.

[74] CMS collaboration, *Effective area for electron isolation*, https://github.com/sachikot/cmssw/blob/CMSSW_7_1_X/EgammaAnalysis/ElectronTools/interface/ElectronEffectiveArea.h#L114-122.

[75] CMS collaboration, *Standard muon ID 2012*, https://twiki.cern.ch/twiki/bin/view/CMSPublic/SWGuideMuonId#Tight_Muon.

[76] CMS collaboration, *Muon PF Isolation*, https://twiki.cern.ch/twiki/bin/view/CMSPublic/SWGuideMuonId#Muon_Isolation.

[77] CMS collaboration, *Cut based photon ID 2012*, https://twiki.cern.ch/twiki/bin/viewauth/CMS/CutBasedPhotonID2012.

[78] CMS Collaboration, *About Photon Identification*, https://twiki.cern.ch/twiki/bin/view/CMS/PhotonIDAnalysis#About_Photon_Identification.

[79] G. Sandro, *Study of γ + jets data with the CMS detector in pp collisions at $\sqrt{s}$ = 8 TeV*, Ph.D. Thesis, UNIVERSITA DEGLI STUDI FIRENZE (2011).

[80] O. Hindrichs et al., *Measurement of the production cross section of Z plus γ and limits on anomalous triple gauge couplings in proton-proton collisions at $\sqrt{s}$ = 8 TeV*, CMS AN-2013/280 (2014).

[81] The CMS Collaboration, *2012 8TeV Jan22 Re-recoed data vs 53X MC*, https://twiki.cern.ch/twiki/bin/view/Main/EGammaScaleFactors2012#2012_8_TeV_Jan22_Re_recoed_data.

[82] CMS collaboration, *Reference muon id and isolation efficiencies*, https://twiki.cern.ch/twiki/bin/view/CMS/MuonReferenceEffs.

[83] CMS collaboration, *Cut based photon ID scale factors for 8TeV*, https://twiki.cern.ch/twiki/bin/viewauth/CMS/CutBasedPhotonID2012.

[84] The CMS Collaboration, *Measurement of the $W\gamma$ and $Z\gamma$ cross section and limits on anomalous triple gauge couplings in pp collisions at $\sqrt{s}$ = 7 TeV*, CMS EWK-11-009 (2013).

[85] J. Kunkle et al., *Measurement of the $pp \to \ell\nu\gamma\gamma$ Final State and Limit on Dimension 8 Effective Anomalous Couplings at $\sqrt{s}$ = 8sTeV*, CMS AN-2013/282 (2015).

[86] The CMS Collaboration, *CMS Luminosity Based on Pixel Cluster Counting - Summer 2013 Updata*, CMS PAS LUMI-13/001 (2013).

[87] CMS collaboration, *Muon trigger efficiencies*, https://twiki.cern.ch/twiki/bin/viewauth/CMS/MuonReferenceEffs.

[88] H. L. Lai, M. Guzzi, J. Huston, Z. Li, P. M. Nadolsky, J. Pumplin and C. P. Yuan, *New parton distributions for collider physics*, Phys.Rev.D82:074024, arXiv:1007.2241, doi:10.1103/PhysRevD.82.074024 (2010).

[89] A. D. Martin, W. J. Stirling, R. S. Thorne and G. Watt, *Parton distributions for the LHC*, Eur.Phys.J.C63:189-285, arXiv:0901.0002 [hep-ph], doi:10.1140/epjc/s10052-009-1072-5 (2009).

[90] L. Lyons, D. Gibaut, and P. Clifford, *How to combine correlated estimates of a single physical quantity*, Nuc. Instr. Meth. A270:No. 110 (1998).

Appendix A

Additions for Chapter 5

A.1 MadGraph5 commands to generate the process

The followings are the `MadGraph5` commands used for generating $Z\gamma\gamma$ signal sample :

```
generate p p > e- e+ a a @1
add process p p > mu- mu+ a a @2
add process p p > ta- ta+ a a @3
```

A.2 Uncertainty estimation in measured cross section

The Z$\gamma\gamma$ cross section in the fiducial region is calculated as:

$$\sigma = (1 - f_\tau) \cdot \frac{N_{obs} - N_{bkg}}{C_{Z\gamma\gamma} \cdot \mathcal{L}} \tag{A.1}$$

where N_{obs} is the number of observed data events in PP region, N_{bkg} is the expected backgrounds in the PP region, $C_{Z\gamma\gamma}$ is acceptance, and $\mathcal{L}$ is the integrated luminosity. The

uncertainty on the measured cross section is calculated as:

$$\left(\frac{\Delta\sigma}{\sigma}\right)^2 = \left(\frac{\sqrt{N_{obs}}}{N_{obs}-N_{bkg}}\right)^2 + \left(\frac{\Delta N_{bkg}}{N_{obs}-N_{bkg}}\right)^2 + \left(\frac{\Delta C_{Z\gamma\gamma}}{C_{Z\gamma\gamma}}\right)^2 + \left(\frac{\Delta\mathcal{L}}{\mathcal{L}}\right)^2 \tag{A.2}$$

A.3 Background predictions from matrix method

The "matrix method" performed using the nominal isolation and loosened isolation in three η regions (EB-EB, EB-EE, and EE-EB) in leading photon p_{T} bins ($15 < p_{\mathrm{T}} < 25$, $25 < p_{\mathrm{T}} < 40$, $40 < p_{\mathrm{T}}$) for the muon and electron channel.

Following tables show evaluated prediction of background events with statistical uncertaintis from the matrix method.

	Input Data			Predicted Counts in PP			
Photon p_{T}	PF	FP	FF	$\gamma\, j$	$j\, \gamma$	$j\, j$	Sum
EB-EB							
15-25	13.0±3.6	10.0±3.2	5.0±2.2	7.3±2.7	4.9±2.4	1.8±1.1	14.0±3.8
25-40	3.0±1.7	14.0±3.7	5.0±2.2	0.3±0.8	5.1±1.7	1.2±0.7	6.6±2.0
40+	7.0±2.6	8.0±2.8	1.0±1.0	3.2±1.6	3.8±1.7	-0.0±0.1	7.0±2.3
Total	23.0±4.8	32.0±5.7	11.0±3.3	10.5±3.2	16.0±3.7	2.5±1.1	29.0±5.0
EB-EE							
15-25	6.0±2.4	4.0±2.0	1.0±1.0	5.3±2.5	2.5±1.5	0.3±0.6	8.1±3.0
25-40	6.0±2.4	5.0±2.2	4.0±2.0	1.9±1.1	1.6±1.0	1.0±0.7	4.5±2.2
40+	6.0±2.4	2.0±1.4	0.0±0.0	1.8±0.9	0.7±0.9	-0.1±0.04	2.4±1.3
Total	18.0±4.2	11.0±3.3	5.0±2.2	11.4±3.3	5.4±2.2	1.3±0.9	18.1±4.1
EE-EB							
15-25	2.0±1.4	3.0±1.7	0.0±0.0	0.7±1.1	1.8±1.8	-0.2±0.3	2.4±2.1
25-40	3.0±1.7	5.0±2.2	3.0±1.7	1.0±0.8	1.7±1.0	1.0±0.7	3.7±1.5
40+	2.0±1.4	8.0±2.8	2.0±1.4	0.5±0.9	2.4±1.1	0.3±0.3	3.2±1.5
Total	7.0±2.6	16.0±4.0	5.0±2.2	2.4±1.8	8.9±3.2	1.8±1.1	13.1±3.8

Table A.1: Number of background predictions from matrix method with use nominal $\sigma_{i\eta i\eta}$ requirement for muon channel.

	Input Data			Predicted Counts in PP			
Photon p_{T}	PF	FP	FF	$\gamma\, j$	$j\, \gamma$	$j\, j$	Sum
EB-EB							
15-25	11.2±0.3	10.2±0.3	2.8±0.1	6.8±0.4	5.3±0.5	2.5±0.5	14.6±0.8
25-40	7.8±0.3	9.0±0.4	1.8±0.1	3.1±0.3	3.6±0.3	1.2±0.4	5.8±0.6
40+	6.2±0.4	3.9±0.2	2.0±0.1	2.9±0.4	1.4±0.4	0.3±0.1	4.6±0.6
Total	24.6±0.5	22.4±0.4	6.41±0.1	13.1±0.6	10.9±0.6	4.0±0.6	28.0±1.0
EB-EE							
15-25	5.2±0.1	3.6±0.1	1.4±0.0	4.3±0.3	2.2±0.2	1.6±0.4	8.1±0.5
25-40	7.2±0.3	3.6±0.2	2.6±0.1	2.3±0.5	1.0±0.4	2.5±1.0	5.8±1.2
40+	7.7±0.4	1.1±0.1	0.6±0.0	2.9±0.3	0.1±0.2	0.0±0.0	3.0±0.4
Total	17.2±0.3	8.0±0.2	4.4±0.1	11.3±0.6	3.5±0.4	3.6±0.6	18.4±0.9
EE-EB							
15-25	4.1±0.1	3.6±0.1	0.7±0.0	2.2±0.2	2.1±0.4	0.5±0.2	4.8±0.5
25-40	1.8±0.1	6.6±0.3	2.0±0.1	0.6±0.1	2.8±0.2	1.5±0.4	4.9±0.5
40+	2.2±0.1	7.7±0.4	1.5±0.1	0.7±0.3	2.7±0.3	0.5±0.3	3.9±0.5
Total	8.0±0.2	15.0±0.3	3.6±0.1	3.4±0.4	9.0±0.6	2.9±0.5	15.3±0.9

Table A.2: Number of background predictions from matrix method with use loosen $\sigma_{i\eta i\eta}$ requirement for muon channel.

	Input Data			Predicted Counts in PP			
Photon p_{T}	PF	FP	FF	$\gamma\, j$	$j\, \gamma$	$j\, j$	Sum
EB-EB							
15-25	9.0±3.0	12.0±3.5	1.0±1.0	5.6±2.2	7.8±2.6	0.0±0.5	13.4±3.4
25-40	8.0±2.8	6.0±2.4	3.0±1.7	2.8±1.3	1.9±1.1	0.7±0.5	5.4±1.8
40+	1.0±1.0	4.0±2.0	4.0±2.0	-1.3±0.8	0.5±1.3	0.3±0.2	-0.5±1.5
Total	18.0±4.2	22.0±4.7	8.0±2.8	7.9±2.8	10.3±3.1	1.8±0.9	20.0±4.3
EB-EE							
15-25	5.0±2.2	4.0±2.0	4.0±2.0	3.7±2.3	2.2±1.5	2.2±1.3	8.1±3.0
25-40	6.0±2.4	4.0±2.0	1.0±1.0	2.1±1.1	1.4±0.9	0.14±0.31	3.6±1.5
40+	6.0±2.4	2.0±1.4	2.0±1.4	2.0±0.9	0.6±0.9	0.12±0.15	2.72±1.28
Total	17.0±4.1	10.0±3.2	7.0±2.6	10.5±3.2	4.6±2.1	2.1±1.1	17.2±4.0
EE-EB							
15-25	1.0±1.0	4.0±2.0	4.0±2.0	-0.9±1.1	0.8±2.6	2.7±1.6	2.6±3.2
25-40	4.0±2.0	3.0±1.7	1.0±1.0	1.5±0.9	1.0±0.8	0.2±0.4	2.7±1.3
40+	2.0±1.4	9.0±3.0	2.0±1.4	0.8±0.8	3.0±1.2	0.2±0.3	4.0±1.5
Total	7.0±2.6	16.0±4.0	7.0±2.6	2.6±1.8	9.1±3.2	2.7±1.3	14.4±3.9

Table A.3: Number of background predictions from matrix method with use nominal $\sigma_{i\eta i\eta}$ requirement for electron channel.

	Input Data			Predicted Counts in PP			
Photon p_{T}	PF	FP	FF	$\gamma\, j$	$j\, \gamma$	$j\, j$	Sum
EB-EB							
15-25	9.7±0.2	8.2±0.2	0.5±0.0	7.0±0.3	5.9±0.3	-0.5±0.1	12.4±0.4
25-40	7.2±0.3	3.6±0.2	2.1±0.1	2.5±0.3	0.5±0.3	1.9±0.6	4.9±0.7
40+	2.2±0.1	2.8±0.2	2.5±0.1	-0.7±0.4	-0.2±0.4	0.5±0.2	-0.4±0.6
Total	18.7±0.4	14.4±0.3	4.8±0.1	9.5±0.5	5.9±0.5	3.2±0.5	18.6±0.9
EB-EE							
15-25	5.2±0.1	2.6±0.1	2.5±0.0	3.8±0.5	1.1±0.1	3.4±0.8	8.3±0.9
25-40	8.3±0.3	4.2±0.2	3.2±0.1	2.5±0.6	1.0±0.4	3.1±1.2	6.6±1.4
40+	5.1±0.3	2.2±0.1	1.9±0.1	1.9±0.2	0.7±0.3	0.4±0.2	3.0±0.4
Total	16.3±0.3	8.6±0.2	6.9±0.1	9.6±0.8	3.2±0.6	6.5±0.9	19.3±1.3
EE-EB							
15-25	1.0±0.0	5.2±0.1	2.3±0.0	-0.1±0.5	2.4±0.9	3.4±1.0	5.7±1.4
25-40	4.8±0.2	3.9±0.2	0.6±0.0	2.3±0.2	1.7±0.1	0.1±0.0	4.1±0.2
40+	2.2±0.1	5.1±0.3	1.5±0.1	1.0±0.2	1.8±0.3	0.5±0.3	3.3±0.5
Total	7.5±0.2	12.7±0.3	4.2±0.1	3.3±0.4	7.5±0.5	3.7±0.7	14.5±0.9

Table A.4: Number of background predictions from matrix method with use loosen $\sigma_{i\eta i\eta}$ requirement for electron channel.